

International Journal of

Rotating Machinery

Special Issue
Wind Generation Systems including Energy Storage

Lead Guest Editor: Lei Chen
Guest Editors: Li Ren, Lin Zhu, Tao Wang, and Yuanzheng Li



Wind Generation Systems including Energy Storage

International Journal of Rotating Machinery

Wind Generation Systems including Energy Storage

Lead Guest Editor: Lei Chen

Guest Editors: Li Ren, Lin Zhu, Tao Wang, and Yuanzheng Li



Copyright © 2017 Hindawi. All rights reserved.

This is a special issue published in “International Journal of Rotating Machinery.” All articles are open access articles distributed under the Creative Commons Attribution License, which permits unrestricted use, distribution, and reproduction in any medium, provided the original work is properly cited.

Editorial Board

Sumanta Acharya, USA
H. Joon Ahn, Republic of Korea
Ryoichi Samuel Amano, USA
Sourabh V. Apte, USA
Farid Bakir, France
Hans Joerg Bauer, Germany
Gerard Bois, France
Christopher Earls Brennen, USA
Alessandro Corsini, Italy

Luis Gato, Portugal
Awatef Hamed, USA
Jechin Han, USA
Hooshang Heshmat, USA
Dimitrios T. Hountalas, Greece
Norihiko Iki, Japan
Tariq Iqbal, Canada
Funazaki Ken-ichi, Japan
Akira Murata, Japan

M. Razi Nalim, USA
Eddie Ng Yin Kwee, Singapore
Yutaka Ohta, Japan
Ion Paraschivoiu, Canada
Paolo Pennacchi, Italy
Sergio Preidikman, USA
Meinhard Taher Schobeiri, USA
Terrence W. Simon, USA
Seung Jin Song, Republic of Korea

Contents

Wind Generation Systems including Energy Storage

Lei Chen, Li Ren, Lin Zhu, Tao Wang, and Yuanzheng Li
Volume 2017, Article ID 7424812, 2 pages

Overvoltage and Insulation Coordination of Overhead Lines in Multiple-Terminal MMC-HVDC Link for Wind Power Delivery

Huiwen He, Lei Wang, Peihong Zhou, and Fei Yan
Volume 2017, Article ID 4849262, 7 pages

Numerical Simulation of Wind Turbine Rotors Autorotation by Using the Modified LS-STAG Immersed Boundary Method

Iliia K. Marchevsky and Valeria V. Puzikova
Volume 2017, Article ID 6418108, 7 pages

Optimal Sizing for Wind/PV/Battery System Using Fuzzy *c*-Means Clustering with Self-Adapted Cluster Number

Xin Liu, Hong-Kun Chen, Bing-Qing Huang, and Yu-Bo Tao
Volume 2017, Article ID 5142825, 9 pages

Variable Ratio Hydrostatic Transmission Simulator for Optimal Wind Power Drivetrains

Jose M. Garcia-Bravo, Ivo N. Ayala-Garcia, and Juan L. Cepeda-Aguilar
Volume 2017, Article ID 5651736, 9 pages

A Comparison of Off-Grid-Pumped Hydro Storage and Grid-Tied Options for an IRSOFC-HAWT Power Generator

Mahdi Majidniya, Kobra Gharali, and Kaamran Raahemifar
Volume 2017, Article ID 4384187, 11 pages

Enhancing LVRT Capability of DFIG-Based Wind Turbine Systems with SMES Series in the Rotor Side

Xiao Zhou, Yuejin Tang, and Jing Shi
Volume 2017, Article ID 4635452, 8 pages

Evaluation of Wind Energy Potential as a Power Generation Source in Chad

Djamal Hissein Didane, Nurhayati Rosly, Mohd Fadhli Zulkafli, and Syariful Syafiq Shamsudin
Volume 2017, Article ID 3121875, 10 pages

Economic Evaluation of Three Available Solutions for Promotion of Wind Power Integration

Hong-Kun Chen, Yan-Juan Yu, Lei Chen, Xin Jiang, and Ren-Yan Yu
Volume 2017, Article ID 1618681, 8 pages

Editorial

Wind Generation Systems including Energy Storage

Lei Chen,¹ Li Ren,² Lin Zhu,³ Tao Wang,⁴ and Yuanzheng Li⁵

¹*School of Electrical Engineering, Wuhan University, Wuhan 430072, China*

²*State Key Laboratory of Advanced Electromagnetic Engineering and Technology, Huazhong University of Science and Technology, Wuhan 430074, China*

³*Department of Electrical Engineering and Computer Science, University of Tennessee, Knoxville, TN 37996, USA*

⁴*Waseda Research Institute for Science and Engineering, Waseda University, Tokyo 169-8555, Japan*

⁵*School of Electrical and Electronic Engineering, Nanyang Technological University, Singapore 639798*

Correspondence should be addressed to Lei Chen; chen_lei@whu.edu.cn

Received 10 September 2017; Accepted 13 September 2017; Published 9 November 2017

Copyright © 2017 Lei Chen et al. This is an open access article distributed under the Creative Commons Attribution License, which permits unrestricted use, distribution, and reproduction in any medium, provided the original work is properly cited.

In recent years, the combined application of wind generation and energy storage has received more and more attention around the world. Technically, wind generation systems including energy storage can offer many benefits, such as power oscillation damping, economic energy dispatch, voltage-frequency stabilization, and fault ride-through (FRT) capability enhancement. This special issue is to provide a platform for presenting the latest research results on wind generation systems including energy storage.

This special issue compiles 8 original researches that describe the technical evaluation, economic performance, low-voltage ride-through (LVRT) capability, optimal capacity, numerical simulation, and experimental verification of wind generation systems including energy storage.

There are three papers on the performance evaluation of wind generation systems. The paper by D. H. Didane et al. conducts the evaluation of wind energy potential as a power generation source in Chad, and a comprehensive wind database and wind map are presented. The paper by H.-K. Chen et al. studies the economic evaluation of three available solutions for promotion of wind power integration, and here the pumped hydrostorage (PHS), heat storage (HS), and electric boiler (EB) are selected to do a detailed comparison. From the given results, the HS requires the least investment and has good performance of coal-saving when accommodating the same amount of curtailed wind power. And the EB has the greatest potential for wind power integration with huge growth of installed capacity of wind

power in the future. In the paper by M. Majidniya et al., enhancing the stability of the horizontal axis wind turbine (HAWT) system is regarded as a research objective, and both of a pumped hydrostorage (PHS) and extra produced electricity are taken into account. The economic analysis of them is performed, and some preliminary discussions on the electricity price and the real interest rate are conducted.

There are two papers on the transient characteristics of wind generation systems. The paper by X. Zhou et al. proposes the use of a superconducting magnetic energy storage (SMES) to improve the LVRT capability of the doubly fed induction generators- (DFIGs-) based wind turbine systems. The demonstrated results show that utilizing the SMES in the rotor side can help to produce a desired output voltage and absorb excess energy under faults, so as to enhance the robustness of wind power generation to a certain extent. In the paper by H. He et al., wind power is transmitted through a voltage source converter- (VSC-) based high voltage direct current (HVDC) system, and the researches on overvoltage calculation and insulation coordination are carried out. It is found that the most serious overvoltage is caused by the fault clearing of the DC breaker, and further the insulation coordination for the overhead lines is addressed in accordance with the calculated overvoltage level.

In addition, the paper by X. Liu et al. investigates the optimal sizing for wind/PV/battery system by use of Fuzzy *c*-means clustering with self-adapted cluster number. Meanwhile, a feasible power balance strategy is introduced

to guide the optimization process with the genetic algorithm, and the optimal configuration is established by considering the minimized cost, reliability, and environmental factors.

Finally, there are two papers on the simulation and experiment of wind generation systems. The paper by J. M. Garcia-Bravo et al. presents the variable ratio hydrostatic transmission simulator for optimal wind power drivetrains. According to the simulation and experimental results, the electrical power output can be regulated further if an energy storage device is used to absorb voltage spikes produced by abrupt changes in wind speed or wind direction. In the paper by I. Marchevsky and V. Puzikova, a software package is developed for numerical simulation of wind turbine rotors autorotation, and the modified LS-STAG level-set/cut-cell immersed boundary method is used. From the simulation analyses, it is verified that the computational results are in good qualitative agreement with the experimental data.

It is hoped that these papers enable enriching our readers and offer useful information about the current contributions and potential challenges related to the wind generation systems including energy storage.

Lei Chen
Li Ren
Lin Zhu
Tao Wang
Yuanzheng Li

Research Article

Overvoltage and Insulation Coordination of Overhead Lines in Multiple-Terminal MMC-HVDC Link for Wind Power Delivery

Huiwen He, Lei Wang, Peihong Zhou, and Fei Yan

State Key Laboratory of Power Grid Environmental Protection, China Electric Power Research Institute, Wuhan 430074, China

Correspondence should be addressed to Huiwen He; husthwh@126.com

Received 2 June 2017; Revised 16 August 2017; Accepted 30 August 2017; Published 25 October 2017

Academic Editor: Tao Wang

Copyright © 2017 Huiwen He et al. This is an open access article distributed under the Creative Commons Attribution License, which permits unrestricted use, distribution, and reproduction in any medium, provided the original work is properly cited.

The voltage-sourced converter-based HVDC link, including the modular multilevel converter (MMC) configuration, is suitable for wind power, photovoltaic energy, and other kinds of new energy delivery and grid-connection. Current studies are focused on the MMC principles and controls and few studies have been done on the overvoltage of transmission line for the MMC-HVDC link. The main reason is that environmental factors have little effect on DC cables and the single-phase/pole fault rate is low. But if the cables were replaced by the overhead lines, although the construction cost of the project would be greatly reduced, the single-pole ground fault rate would be much higher. This paper analyzed the main overvoltage types in multiple-terminal MMC-HVDC network which transmit electric power by overhead lines. Based on ± 500 kV multiple-terminal MMC-HVDC for wind power delivery project, the transient simulation model was built and the overvoltage types mentioned above were studied. The results showed that the most serious overvoltage was on the healthy adjacent line of the faulty line caused by the fault clearing of DC breaker. Then the insulation coordination for overhead lines was conducted according to the overvoltage level. The recommended clearance values were given.

1. Introduction

The voltage-sourced converter- (VSC-) based high-voltage DC (HVDC) transmission system is considered for a wide range of applications for wind power, photovoltaic energy, or other kinds of new energy delivery and grid-connection due to flexibly control of active power and reactive power output capability [1–4]. The Nanhui MMC-HVDC demonstration project and the Nanao multiple-terminal MMC-HVDC link have been put into operation already and achieved the stable and reliable wind power transmission [5, 6].

At present, the study focuses on the MMC principles and controls and less research has been done on the overvoltage of transmission line for the MMC-HVDC project. And there are few studies on the overvoltage characteristics of multi-terminal MMC-HVDC [7, 8]. State Grid Beijing Economic and Technical Research Institute has done research on the Dalian MMC-HVDC project considering the short circuit fault at AC bus, grid side and valve side of connection transformer, smoothing reactor, and DC pole bus. According to the simulation results of overvoltage, the reference voltage and switching impulse withstanding voltage of MOAs in the

converter station were determined [9]. Based on the Trans Bay MMC-HVDC project, Zhejiang University studied the 14 kinds of fault and found the most serious overvoltages were caused by the single-phase grounding fault at valve side of converter transformer, the short circuit of transformer, the ground short circuit fault at valve head, DC bus grounding fault, and DC line grounding fault. The MOA configuration and insulation coordination scheme were proposed. The withstanding voltages of equipment were determined by deterministic method and the margin coefficient between withstand voltage and impulse overvoltage could be selected as 15%, 20%, and 25% for switching impulse, lighting impulse, and steep impulse, respectively [10].

The researches mentioned above were focused on the converter station. Most of the MMC-HVDC projects adopt cables for power transmission all around the world. The cables buried in the ground are not affected by the surrounding environment, so the failure rate is lower [11, 12]. However, cables lines are expensive and the overhead lines can greatly reduce the cost of construction. The overhead lines are susceptible to the surrounding environment, such as lightning and pollution, and the single-pole grounding fault rate is

much higher than using cable lines. Therefore, it is necessary to study the overvoltage generated by overhead line faults to support the design of line insulation.

This paper focuses on the overvoltage level of overhead lines in multiple-terminal MMC-HVDC project. Firstly it pointed out the main overvoltage types of overhead lines in multiple-terminal MMC-HVDC link. Based on an ± 500 kV multiple-terminal MMC-HVDC for wind power delivery project, the transient simulation model was built and various overvoltage types mentioned above were studied. Then the insulation coordination for overhead lines was conducted according to the overvoltage level. In the end the recommended clearance values were given.

This paper is organized as follows. Section 2 is devoted to analyzing the main overvoltage types of overhead lines in multiple-terminal MMC-HVDC link and the differences between it and conventional point-to-point LCC-HVDC project while Section 3 presents the simulation overvoltage results based on a multiple-terminal MMC-HVDC project according to Section 2. Then insulation coordination for overhead lines is conducted and the recommended clearances are given in Section 4. Finally, conclusions are drawn in Section 5.

2. Overvoltage Types of Overhead Line in Multiple-Terminal MMC-HVDC Project

LCC-HVDC systems are usually 2 terminals adopting overhead transmission lines and the occurrence probability of single-pole grounding fault is the highest. Statistical data show that the single-pole lightning flashover rate of ± 500 kV DC transmission lines is 0.28 times per 100 km every year. In a bipolar operation, a grounding fault occurring at one pole will induce the slow front overvoltage at the sound pole through the coupling between two poles and reflection and refraction of traveling wave at both ends of line. The magnitude of the overvoltage can be estimated by the following formula:

$$U_p = U_{dc} \left(1 + \frac{Z_{m0} - Z_{m1}}{Z_{m0} + Z_{m1} + 2R_e} \right), \quad (1)$$

where Z_{m0} and Z_{m1} are zero sequence and positive sequence wave impedance of transmission line, respectively; R_e is the grounding resistance.

The induced overvoltage at sound pole caused by single-pole grounding fault should also be considered for overhead lines in multiple-terminal MMC-HVDC project and the magnitude of the overvoltage can be estimated by formula (1) too. In order to improve the availability of MMC-HVDC project, the DC circuit breaker would be installed for fault clearing at DC side. So the line fault clearing overvoltage and reclosing overvoltage should be considered.

- (1) The line fault clearing overvoltage mainly refers to the overvoltage on the sound pole line and the adjacent sound line generated by the fault tripping. It is equivalent to superimposing a current source with a reverse fault current on the circuit breaker when the circuit breaker interrupts the fault current. The current wave propagation and reflection on the adjacent sound line

form transient overvoltage. The fault current is related to the main circuit parameters of converter station, the operation characteristics of DC circuit breaker, and the fault grounding resistance.

- (2) When the DC line is switched on or reclosing, the overvoltage is generated due to the difference between the initial voltage of the line to the ground and the forced voltage at the end of the transition process. The magnitude of the overvoltage can be estimated by the following formula:

$$U_{pc} = 2U_w - U_0, \quad (2)$$

where U_w is the forced voltage at the end of the transition process and U_0 is the initial voltage of the line to the ground.

Therefore 3 kinds of overvoltage are as follows, which should be studied for overhead lines of multiterminal MMC-HVDC systems:

- (1) Induced overvoltage on healthy pole line caused by single-pole grounding fault
- (2) Fault clearing overvoltage
- (3) Closing and reclosing overvoltage.

3. Analysis of Overvoltage of Overhead Transmission Lines in Multiple-Terminal MMC-HVDC Project

3.1. Simulation Parameters

3.1.1. Main Circuit Parameter. A 4-terminal ± 500 kV MMC-HVDC for wind power delivery project, using half bridge and real bipolar connection, has 245 levels and DC rated voltage is 535 kV. The rated voltage of AC power network is 230 kV at delivery end A, which can send wind power out with 17 kA three-phase short circuit current, and the rated capacity of A is 3000 MW under the normal operation in island. The rated voltage of AC power network is 230 kV at delivery end B, which can send wind power out with 17 kA three-phase short circuit current, and the rated capacity of B is 1500 MW under the normal operation in island. The rated voltage of AC power network is 525 kV at delivery end C, which can send wind power out with 18 kA three-phase short circuit current, and the rated capacity of C is 1500 MW. The rated voltage of AC power network is 525 kV at delivery end D, which can send wind power out with 63 kA three-phase short circuit current, and the rated capacity of D is 3000 MW.

The lengths of DC transmission lines of 4-terminal system are shown in Figure 1. The type of conductors is 4 × JL/G2A-720/50 with 12.8 m pole distance, and the type of ground wire is OPGW-150 with 12 m horizontal distance, together with the model JNRLH60/G1A-400/35 of metallic return line which has the horizontal distance of 9 m. Typical tower model of tangent tower is shown in Figure 2, and the transmission line is simulated by Frequency Dependent (Phase) Model in PSCAD. In the converter station, the

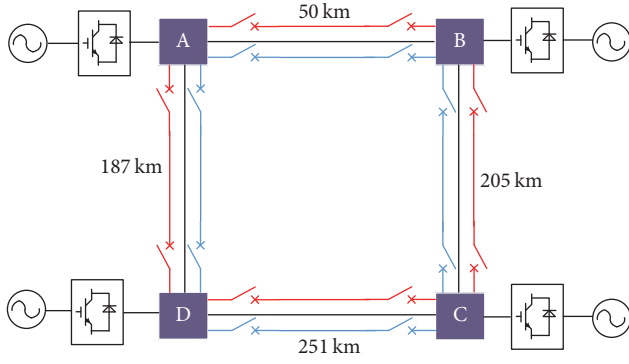


FIGURE 1: Schematic diagram of 4-terminal transmission lines.

current limiting reactors are arranged on the pole lines and the metallic return lines; the values of reactance are 150 mH on the pole line and 300 mH on the neutral line. The reference voltage of pole line arrester is 629 kV and residual voltage is 904 kV under switch operation with 2 kA current.

According to empirical equation (3), the arc resistance R_G in the air can be calculated:

$$R_G \approx 1050 \frac{L_G}{I_G}, \quad (3)$$

where L_G is the length of arc and I_G is the rms. of current with the unit ampere. In the simulation, the sum resistance of arc and grounding tower is 4 Ω .

3.1.2. Control and Protection Model of Converter Station. A double closed-loop controller is established in PSCAD to achieve converter station-level control. Double closed-loop control can be divided into an outer loop controller and an inner loop controller. The outer loop controller can calculate the current reference value of the current-mode inner loop controller according to the active and the reactive power command. The inner loop controller keeps the dq axis current tracking its reference value by adjusting the output voltage of the inverter. The control system used in the simulation is shown in Figure 3 [13–16].

According to Figure 3, the dynamic differential equation of AC side in three-phase stationary coordinate system is shown as

$$\begin{bmatrix} u_{sa} \\ u_{sb} \\ u_{sc} \end{bmatrix} = L \frac{d}{dt} \begin{bmatrix} i_{sa} \\ i_{sb} \\ i_{sc} \end{bmatrix} + R \begin{bmatrix} i_{sa} \\ i_{sb} \\ i_{sc} \end{bmatrix} + \begin{bmatrix} u_{ca} \\ u_{cb} \\ u_{cc} \end{bmatrix}, \quad (4)$$

where u_{sa} , u_{sb} , and u_{sc} are the measured phase A, phase B, and phase C voltages at grid side of converter transformer, respectively. i_{sa} , i_{sb} , and i_{sc} are the measured phase A, phase B, and phase C currents at grid side of converter transformer, respectively. u_{ca} , u_{cb} , and u_{cc} are the measured phase A, phase B, and phase C voltages at valve side of converter transformer, respectively. L is the equivalent reactance. R is the equivalent resistance.

After the park transformation, the active power P injected into the converter station from the AC system is as (5). The

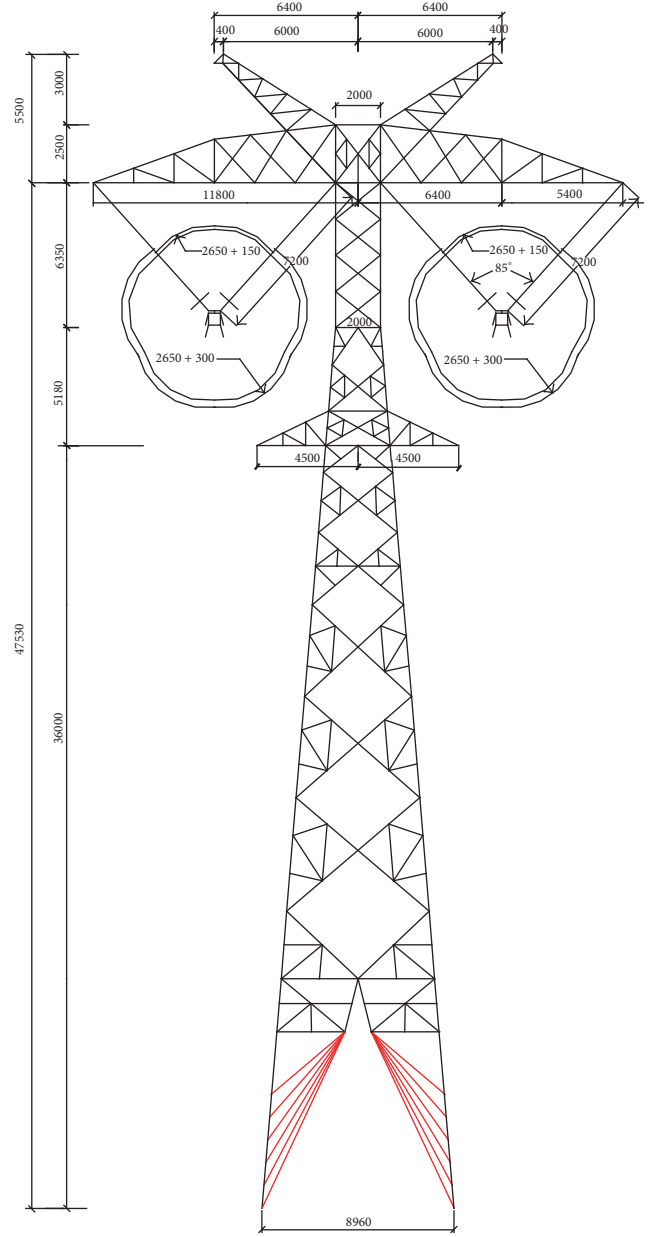


FIGURE 2: Typical tower diagram of single circuit transmission line.

reactive power Q injected into the converter station from the AC system is as (6). So the decoupled control of active power and reactive power can be realized:

$$P = \frac{3}{2} (u_{sd}i_{sd} + u_{sq}i_{sq}) = \frac{3}{2} u_{sd}i_{sd}, \quad (5)$$

$$Q = \frac{3}{2} (u_{sd}i_{sq} - u_{sq}i_{sd}) = \frac{3}{2} u_{sd}i_{sq}, \quad (6)$$

where u_{sd} and u_{sq} are the d axis and q axis voltages derived from park transformation of u_{sa} , u_{sb} , and u_{sc} , respectively. i_{sd} and i_{sq} are the d axis and q axis currents derived from park transformation of i_{sa} , i_{sb} , and i_{sc} , respectively.

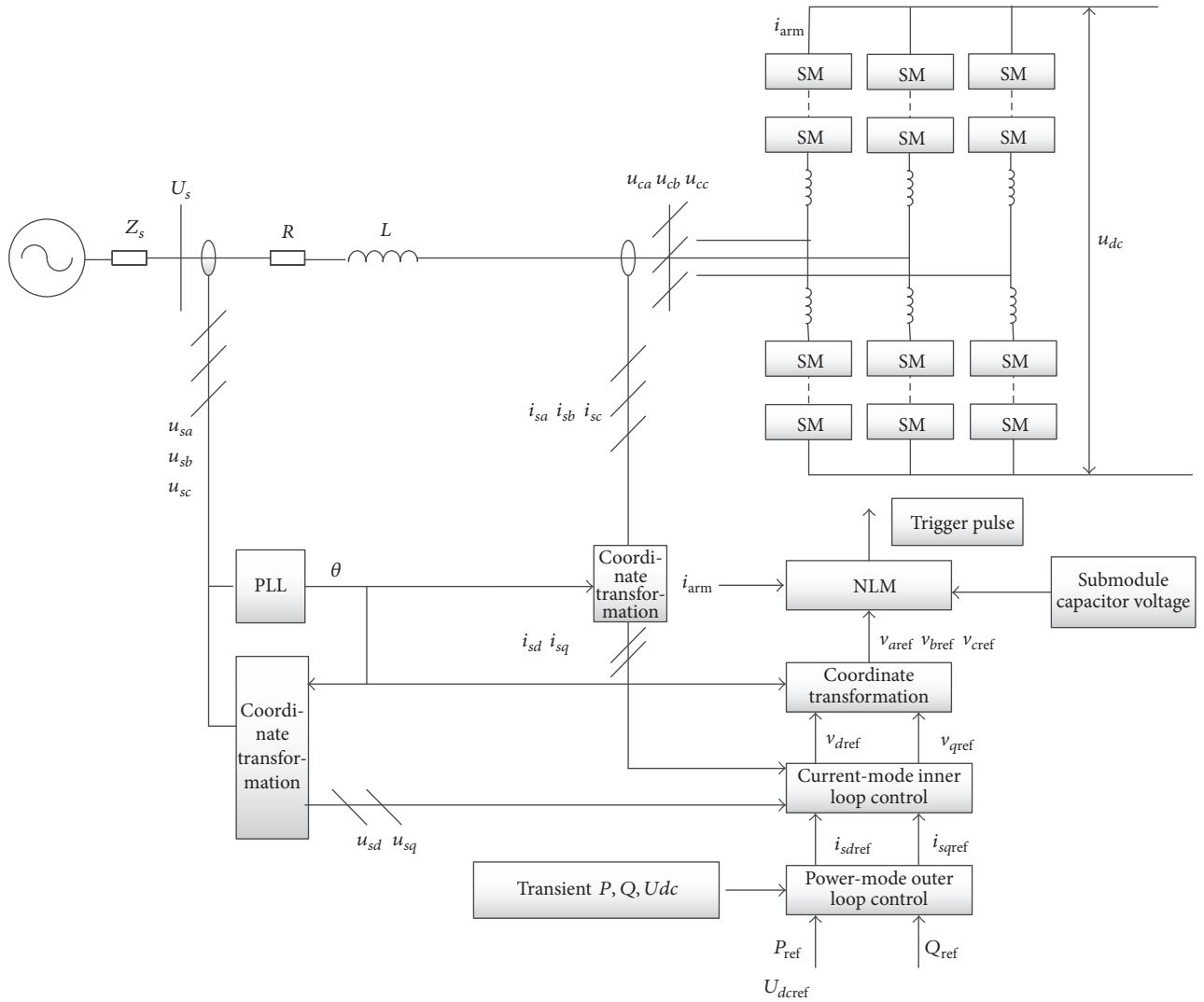


FIGURE 3: The schematic diagram of MMC control system.

3.1.3. Wind Power Model. Two wind farms provide the power sources for 2 substations of the 4-terminal ± 500 kV MMC-HVDC project. In order to calculate the accurate overvoltage level, the influence of the wind farms on overvoltage was considered.

In the simulation, the electromagnetic transient model based on the $dq0$ transform of doubly fed induction generator was established. The dq coordinate system based on rotation speed of rotor was adopted. The voltage and current on the armature side and the exciting side satisfy [17]

$$V_P = -R_P i_P - \frac{d\lambda_P}{dt} + \omega N \lambda_P, \quad (7)$$

$$V_E = -R_E i_E - \frac{d\lambda_E}{dt}, \quad (8)$$

$$N = \begin{bmatrix} 0 & 0 & 0 \\ 0 & 0 & -1 \\ 0 & 1 & 0 \end{bmatrix}, \quad (9)$$

where V_P and V_E are voltages on the armature side and the exciting side, respectively. R_P and R_E are resistance on the armature side and resistance on the exciting side, respectively. i_P and i_E are currents on the armature side and the exciting side, respectively. λ_P and λ_E are flux linkage matrixes on the armature side and the exciting side, respectively. ω is the angular velocity of rotor rotation.

3.2. Overvoltage Analysis. Two modes of operation are considered during the simulation:

(1) Normal mode:

All the stations access the network.

(2) Abnormal mode:

Some of the stations are unconnected to the network, which leads to a longer transmission line than normal mode.

The specific calculation process is as follows. The DC operation voltage is 535 kV before fault. The fault line is

TABLE 1: Overvoltages of transmission lines under normal mode.

Lines	Overvoltages of pole lines	
	kV	p.u.
A-D	950	1.78
C-D	974	1.82
B-C	991	1.85
A-B	888	1.66

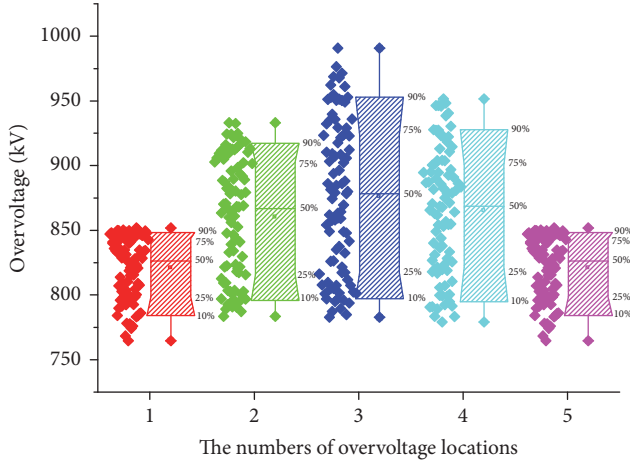


FIGURE 4: The overvoltage distribution and probability distribution of B-C line caused by A-D line fault under normal mode.

divided into 10 sections. Along the line each section is grounded. Then the circuit breakers at the ends of fault line trip remove the temporary ground fault, and after the delay time the DC circuit breakers reclose. Both the overvoltages caused during the grounding and reclose processes are taken into consideration. Besides, the overvoltages caused by faults on other lines should be calculated too.

3.2.1. Normal Mode. The overvoltage levels of all pole lines are shown in Table 1. The maximum overvoltage of 990.77 kV (1.85 p.u., 1 p.u. = 535 kV) appeared in the B-C line, caused by the A-D line fault. The overvoltage distribution and probability distribution of B-C line are shown in Figure 4. The statistics overvoltage along the line is umbrella type distribution. In the middle of line the overvoltage is high and to both ends of the line diminishing. This is due to the installation of the arrester on the pole line bus, which can suppress the overvoltage.

3.2.2. Abnormal Mode. The overvoltage levels of all pole lines were simulated under abnormal mode, which means some of the stations were unconnected to the DC grid during the simulations. The maximum overvoltage, out of hundreds of simulation results of different unconnected stations, occurred in case C station is unconnected. In this section, overvoltages of transmission lines when C station is unconnected are shown in Table 2. The maximum overvoltage has the peak of 1034 kV (1.93 pu), appearing in the CD line, caused by

TABLE 2: Overvoltages of transmission lines under abnormal mode (C station is unconnected).

Lines	Overvoltages of pole lines	
	kV	p.u.
A-D	998	1.87
C-D	1034	1.93
B-C	1010	1.89
A-B	896	1.68

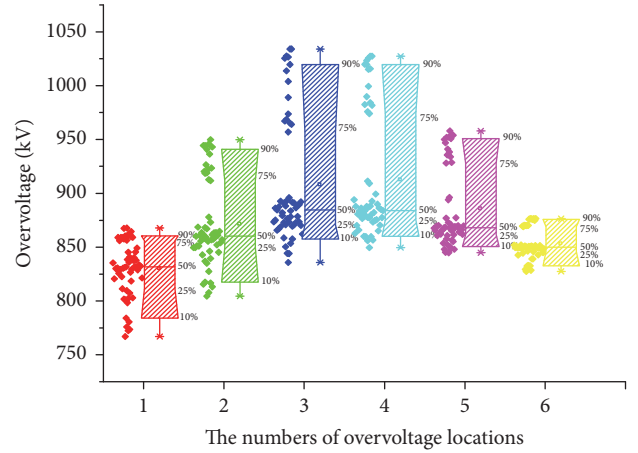


FIGURE 5: The overvoltage distribution and probability distribution of C-D line caused by A-B line fault with unconnected C station.

the A-B positive line ground fault. The overvoltage distribution and probability distribution of C-D line are shown in Figure 5, under situation of the unconnected C station. The maximum overvoltage waveform and the corresponding pole bus waveform are shown in Figure 6. It can be seen that the maximum overvoltage occurs during the DC circuit breaker opening process. Depending on the time difference between peaks, the peaks of the waveform in Figure 6 were caused by the different wave velocities of reflected positive sequence and zero sequence waves.

4. Insulation Coordination of Pole Lines

According to IEC 60071-3, the switching impulse 50% flashover voltage $U_{50\%s}$ of air gap between wire and tower can be calculated in (10), which can be used for insulation coordination of pole lines:

$$U_{50\%s} = \frac{K_a K_3'}{(1 - 2\sigma_s)} U_m, \quad (10)$$

where U_m is maximum voltage of system (535 kV in this paper), K_a is discharge voltage correction coefficient of air density and humidity of the switch impulse voltage, K_3' is the per unit value of overvoltage, and σ_s is the standard deviation.

Altitude correction can be conducted by IEC 60071-2 with safety margin. The calculation formula is showed by

$$K_a = e^{m(H/8150)}, \quad (11)$$

TABLE 3: Required values of air gaps under switch impulse overvoltage for a 4-terminal MMC-HVDC project.

Lines	Switching overvoltage level (p.u.)	Required 50% switching impulse discharge voltage	Altitude (m)		
			0	1000	2000
A-D	1.9 p.u.	1130	2.73	3.13	3.63
C-D	1.93 p.u.	1147	2.79	3.21	3.73
B-C	1.9 p.u.	1130	2.73	3.13	3.63
A-B	1.7 p.u.	1011	2.4	2.75	3.2

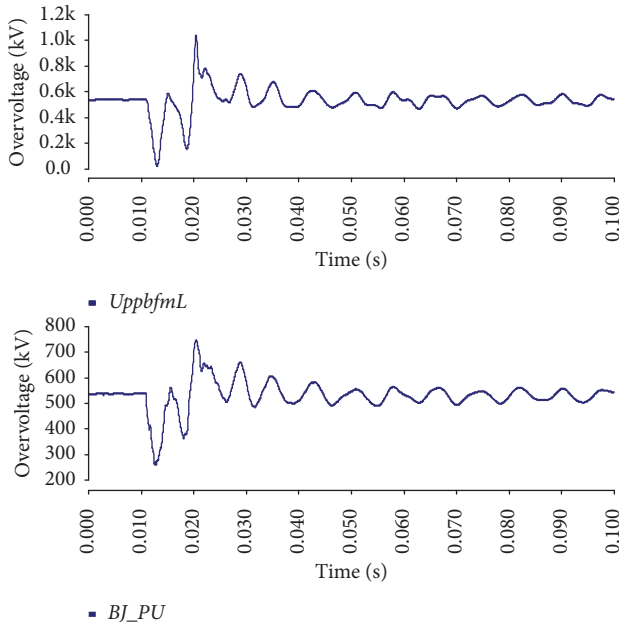


FIGURE 6: The waveforms of maximum overvoltage on C-D line and pole bus of D station under the mode of unconnected C station.

where H is the altitude above sea level measured in meters and the value of m depended on the type of voltage impulse.

The discharge curve of air gap of double circuit tower is provided by CEPRI tested on upper layer of ± 500 kV DC double circuit transmission line, and the discharge curve of air gap of single circuit tower is tested on ± 500 kV real type tower with V-type insulator string. The air gap flashover curve could be obtained by referring to relevant papers [18]. The calculated air gaps of single circuit and double circuit on one tower under switch impulse voltage are shown in Table 3. The required values of air gaps are considered under normal mode and abnormal mode (without C substation).

5. Conclusion

- (1) It is different from circuit breaker adopted MMC-HVDC system and LCC-HVDC when confronted with overvoltage of transmission line. In LCC-HVDC, only the induced overvoltage on sound line caused by single-pole line fault is considered. Besides the induced overvoltage, the fault clearing overvoltage and reclosing overvoltage of transmission line have to

be taken into consideration in the case of multiterminal MMC-HVDC project.

- (2) The statistics overvoltage on the sound line caused by ground fault presents the umbrella type distribution along the line. In the middle of line the overvoltage is high and to both ends of the line diminishing. In this paper, the simulated overvoltage of the project is up to 1.93 p.u., occurring during the DC circuit breaker clearing the DC side failure. The suppression measures of DC circuit breaker causing overvoltage need further study.
- (3) The required minimal clearance of pole lines under switch impulse overvoltage can be selected as 2.79 m at an altitude of 0 m. Differential air gap selection for various transmission lines is also recommended.
- (4) The mechanism for the generation of overvoltages has not been clearly explained. The quantitative influence of the line length, the grounding mode of the valve side of converter, and the network structure on the overvoltage level should be further studied to support the project design.

Conflicts of Interest

The authors declare that there are no conflicts of interest regarding the publication of this paper.

Acknowledgments

The authors are grateful for the support provided by the National Key Research and Development Program of China (Grant 2016YFB0900900) and the SGCC Project of Overvoltage and Insulation Coordination Technology Research of ± 500 kV Flexible DC Grid (GY71-15-076).

References

- [1] H. Zhiyuan, Y. Zhao, and T. Guangfu, "Key Technology Research and Application of the ± 320 kV/1000 MW VSC-HVDC," *Smart Grid*, vol. 4, pp. 124–132, 2016.
- [2] M. Weimin, W. Fangjie, Y. Yiming et al., "Flexible HVDC Transmission Technology's Today and Tomorrow," *High Voltage Engineering*, vol. 40, pp. 2429–2439, 2014.
- [3] T. Guangfu, H. Zhiyuan, and P. Hui, "Discussion on Applying the VSC-HVDC Technology in Global Energy Interconnection," *Smart Grid*, vol. 4, no. 2, pp. 116–123, 2016.
- [4] H. Alyami and Y. Mohamed, "Review and development of MMC employed in VSC-HVDC systems," in *Proceedings of the*

- 2017 IEEE 30th Canadian Conference on Electrical and Computer Engineering (CCECE), pp. 1–6, April 2017.
- [5] L. Xingyuan, Z. Qi, W. Yuhong et al., “Control strategies of voltage source converter based direct current transmission system,” *Gaodiyanya Jishu/High Voltage Engineering*, vol. 42, no. 10, pp. 3025–3037, 2016.
- [6] N. Zhang, C. Kang, D. S. Kirschen et al., “Planning pumped storage capacity for wind power integration,” *IEEE Transactions on Sustainable Energy*, vol. 4, no. 2, pp. 393–401, 2013.
- [7] J. Lyu, X. Cai, and M. Molinas, “Frequency Domain Stability Analysis of MMC-Based HVdc for Wind Farm Integration,” *IEEE Journal of Emerging and Selected Topics in Power Electronics*, vol. 4, no. 1, pp. 141–151, 2016.
- [8] H. Chang, D. Chen, Y. Wu, and Y. Ma, “Analysis and optimization strategy of power disturbance on Xiamen flexible HVDC project,” *Gaodiyanya Jishu/High Voltage Engineering*, vol. 42, no. 10, pp. 3045–3050, 2016.
- [9] M. Weimin, J. Weiyong, and L. Yanan, “System design for dalian VSC-HVDC power transmission project,” *Electric Power Construction*, vol. 34, no. 5, pp. 1–5, 2013.
- [10] Z. Xu, G. Liu, and Z. Zhang, “Research on fault protection principle of DC grids,” *Gaodiyanya Jishu/High Voltage Engineering*, vol. 43, no. 1, pp. 1–8, 2017.
- [11] F. B. Ajaj and R. Iravani, “Cable surge arrester operation due to transient overvoltages under DC-side faults in the MMC-HVDC link,” *IEEE Transactions on Power Delivery*, vol. 31, no. 3, pp. 1213–1222, 2016.
- [12] M. Wang, Y. Hu, W. Zhao, Y. Wang, and G. Chen, “Application of modular multilevel converter in medium voltage high power permanent magnet synchronous generator wind energy conversion systems,” *IET Renewable Power Generation*, vol. 10, no. 6, pp. 824–833, 2016.
- [13] Z. Chengyong, *Modeling and Simulation of Flexible HVDC*, China Electric Power Press, Beijing, China, 2014.
- [14] F. Zhang, J. Xu, and C. Zhao, “New control strategy of decoupling the AC/DC voltage offset for modular multilevel converter,” *IET Generation, Transmission and Distribution*, vol. 10, no. 6, pp. 1382–1392, 2016.
- [15] Y. Dong, W. Ling, J. Tian et al., “Control protection system for Zhoushan multi-terminal VSC-HVDC,” *Electric Power Automation Equipment*, vol. 36, no. 7, pp. 169–175, 2016.
- [16] K. Ou, H. Rao, Z. Cai et al., “MMC-HVDC simulation and testing based on real-time digital simulator and physical control system,” *IEEE Journal of Emerging and Selected Topics in Power Electronics*, vol. 2, no. 4, pp. 1109–1116, 2014.
- [17] Z. Gu, Y. Tang, W. Liu et al., “Electromechanical transient—electromagnetic transient hybrid simulation of double-fed induction generator,” *Power System Technology*, vol. 39, no. 3, pp. 615–620, 2015.
- [18] W. Liao, Y. Ding, Z. Sun, and Z. Su, “Altitude correction of switching impulse flashover voltage of tower gaps with V-shaped insulator strings for HVDC power transmission lines,” *Dianwang Jishu/Power System Technology*, vol. 36, no. 1, pp. 182–188, 2012.

Research Article

Numerical Simulation of Wind Turbine Rotors Autorotation by Using the Modified LS-STAG Immersed Boundary Method

Ilia K. Marchevsky and Valeria V. Puzikova

Applied Mathematics Department, Bauman Moscow State Technical University (BMSTU), 5 2nd Baumanskaya, Moscow 105005, Russia

Correspondence should be addressed to Ilia K. Marchevsky; iliamarchevsky@mail.ru

Received 7 April 2017; Revised 21 July 2017; Accepted 14 August 2017; Published 11 October 2017

Academic Editor: Lin Zhu

Copyright © 2017 Ilia K. Marchevsky and Valeria V. Puzikova. This is an open access article distributed under the Creative Commons Attribution License, which permits unrestricted use, distribution, and reproduction in any medium, provided the original work is properly cited.

A software package is developed for numerical simulation of wind turbine rotors autorotation by using the modified LS-STAG level-set/cut-cell immersed boundary method. The level-set function is used for immersed boundaries description. Algorithm of level-set function construction for complex-shaped airfoils, based on Bézier curves usage, is proposed. Also, algorithm for the level-set function recalculation at any time without reconstructing the Bézier curve for each new rotor position is described. The designed second-order Butterworth low-pass filter for aerodynamic torque filtration for simulations using coarse grids is presented. To verify the modified LS-STAG method, the flow past autorotating Savonius rotor with two blades was simulated at $Re = 1.96 \cdot 10^5$.

1. Introduction

The rotor is the first element in the chain of functional elements of a wind turbine. Its aerodynamic and dynamic properties, therefore, have a decisive influence on the entire system in many respects. The designer faces the problem of finding the relationship between the actual shape of the rotor, for example, the number of rotor blades or the airfoil of its blades, and its aerodynamic properties.

To simulate rotor's dynamics [1–6] and, in particular, its autorotation, there is a need to solve coupled aeroelastic problems. Such problems are complicated for numerical solution, since it is necessary to take into account interference between the flow and moving immersed body. So, the aim of this research is to develop an efficient numerical method for simulation of wind turbine rotors autorotation.

In case of massive body, when its average density is significantly higher than density of the flow, coupled aeroelastic problems can be solved using “step-by-step” weak-coupling numerical algorithm, firstly simulating flow around the body, which moves according to known parameters, and then computing the dynamics of the body under known hydrodynamic loads. Such case is considered in this research.

Immersed boundary methods [7] are suitable for numerical simulation in coupled aeroelastic problems, since they do not require a coincidence of cell edges and boundaries of the computational domain and allow solving problems when domain shape is irregular or it changes significantly in the simulation process due to aeroelastic body motion. The main advantage of these methods is that the mesh should not be reconstructed at every time step.

In the present study, the LS-STAG cut-cell immersed boundary method [8] is used for rotors autorotation simulation. This method permits solving problems on the Cartesian grid. The immersed boundary is represented with the level-set function [9]. Linear systems resulting from the LS-STAG discretization of the Navier-Stokes or Reynolds-averaged Navier-Stokes equations are solved using the BiCGStab method [10] with the ILU and Multigrid [11, 12] preconditioning. An original algorithm for the solver cost-coefficient estimation [13] is used for the optimal parameters of the multigrid preconditioner choice.

2. Governing Equations

The problem is considered in 2D unsteady case when the flow around a rigid airfoil is assumed to be viscous and

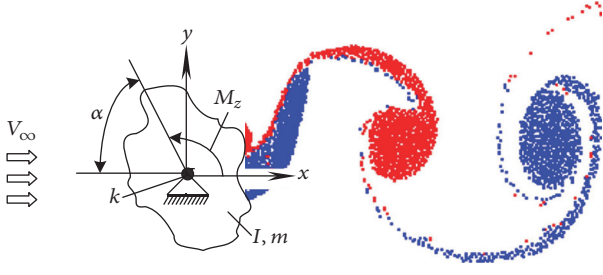


FIGURE 1: The airfoil of irregular shape with one rotational degree of freedom and schematic view of vortex wake behind it.

incompressible. The continuity and momentum equations are as follows:

$$\begin{aligned} \nabla \cdot \mathbf{v} &= 0, \\ \frac{\partial \mathbf{v}}{\partial t} + (\mathbf{v} \cdot \nabla) \mathbf{v} &= \frac{1}{\rho} \nabla p + \nu \Delta \mathbf{v}. \end{aligned} \quad (1)$$

Here \mathbf{v} is the velocity vector, p is the pressure, t is the time, ρ is the flow density, and ν is the flow kinematic viscosity. The boundary conditions on the outer boundaries of the computational domain are as follows:

$$\begin{aligned} \mathbf{v}|_{\text{inlet}} &= \mathbf{v}_{\infty}, \\ \frac{\partial \mathbf{v}}{\partial \mathbf{n}}|_{\text{outlet}} &= 0, \\ \frac{\partial p}{\partial \mathbf{n}}|_{\text{inlet\&outlet}} &= 0. \end{aligned} \quad (2)$$

Here \mathbf{v}_{∞} is the velocity vector on the inlet boundary and \mathbf{n} is the unit outer normal vector. The boundary conditions on the surface line of the airfoil are no-slip conditions:

$$\begin{aligned} \mathbf{v}|_{\text{airfoil}} &= \mathbf{v}^{\text{ib}}, \\ \frac{\partial p}{\partial \mathbf{n}}|_{\text{airfoil}} &= 0. \end{aligned} \quad (3)$$

Here \mathbf{v}^{ib} is the velocity of the immersed boundary.

To simulate the rotation of wind turbine rotors, the following dynamics equation is being solved:

$$I\ddot{\alpha} + k\dot{\alpha} = M_z^{\text{flow}}. \quad (4)$$

Here α is the rotation angle of the rotor, I is the polar inertia moment of the rotor, k is the viscous friction coefficient in the axis, and M_z^{flow} is the aerodynamic torque. Two-dimensional problem is considered, so $M_z^{\text{flow}} = M_z$ (Figure 1).

3. Numerical Method

The Cartesian mesh with cells $\Omega_{i,j} = (x_{i-1}, x_i) \times (y_{j-1}, y_j)$ is introduced in the rectangular computational domain. It is considered that $\Gamma_{i,j}$ is the face of $\Omega_{i,j}$ cell and $\mathbf{x}_{i,j}^c = (x_i^c, y_j^c)$ is its center. Unknown components $u_{i,j}$ and $v_{i,j}$ of velocity

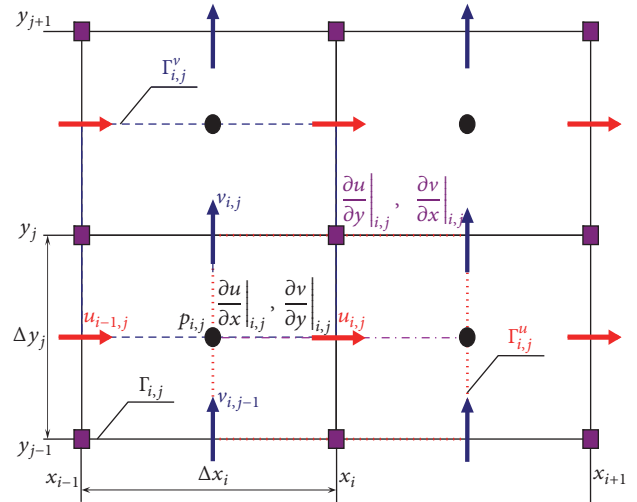


FIGURE 2: Staggered arrangement of the variables on the modified LS-STAG mesh.

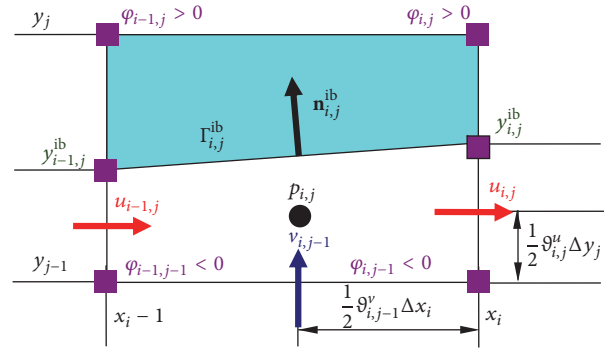


FIGURE 3: Example of a cut-cell.

vector \mathbf{v} are computed in the middle of fluid parts of the cell faces. These points are the centers of control volumes $\Omega_{i,j}^u = (x_i^c, x_{i+1}^c) \times (y_{j-1}, y_j)$ and $\Omega_{i,j}^v = (x_{i-1}, x_i) \times (y_j^c, y_{j+1}^c)$ with faces $\Gamma_{i,j}^u$ and $\Gamma_{i,j}^v$, respectively (Figure 2). The main idea of this numerical method is described in our previous papers, for example, in [14].

Cells which the immersed boundary intersects are the so-called cut-cells (Figures 3 and 4). These cells contain the solid part together with the liquid one. The level-set function φ is used for immersed boundary Γ^{ib} description. The boundary Γ^{ib} is represented by a line segment on the cut-cell $\Omega_{i,j}$. Locations of this segment's endpoints are defined by a linear interpolation of the variable $\varphi_{i,j} = \varphi(x_i, y_j)$.

A few notes should be mentioned about construction of the level-set function. The level-set function cannot be constructed analytically for rotor with complex shape, that is, Darrieus rotor, as for circular airfoil and for simple rotor shapes, for example, for Savonius rotor (Figures 5 and 6). For this reason, it is necessary to approximate the rotor surface line with a curve, which would make it possible to simulate both smooth parts of the boundary and the sharp edges. Moreover, it is desirable that the distance from an arbitrary

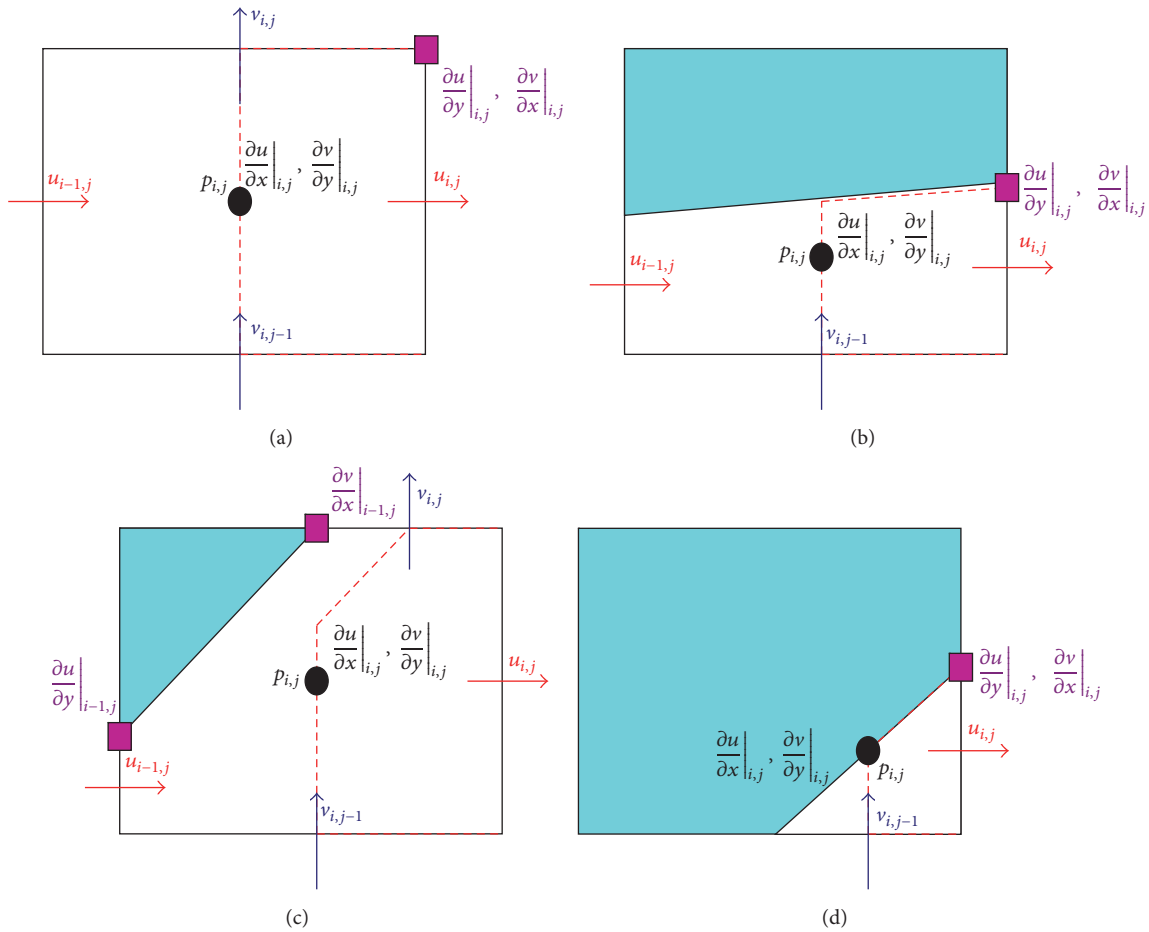


FIGURE 4: Locations of the variables discretization points in case of generic cells on the modified LS-STAG mesh: (a) Cartesian fluid cell; (b) north trapezoidal cell; (c) northwest pentagonal cell; (d) northwest triangle cell.

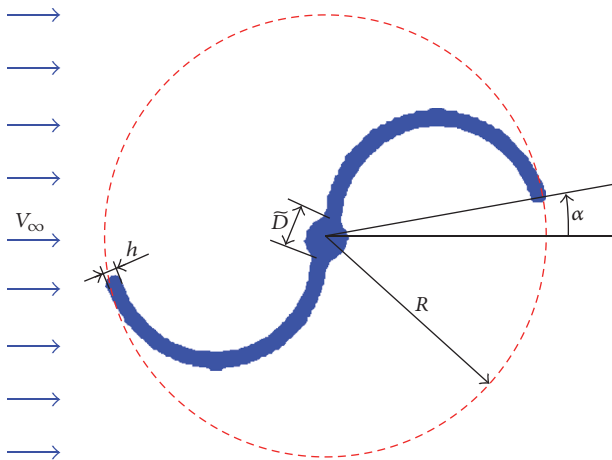


FIGURE 5: Schematic of the two-bucket Savonius rotor.

point to the boundary can be calculated easily. An efficient approach for the level-set function construction for an airfoil of arbitrary shape, which corresponds to the mentioned requirements, is described in [15]. The airfoil's surface line

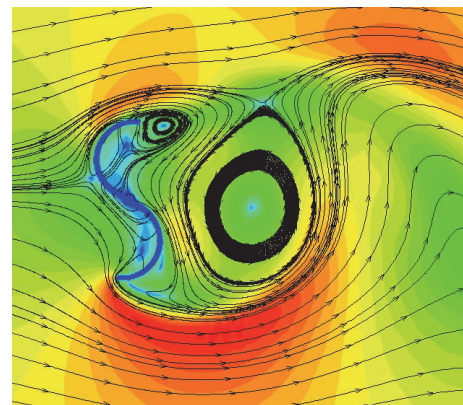


FIGURE 6: Flow past autorotating Savonius rotor with two blades.

approximation by using Bézier curve is taken as a basis of the developed algorithm.

In order to avoid the Bézier curve reconstruction at every time step for the airfoil surface line, the following approach can be used. At the beginning of the computation, the Bézier curve and its derivative should be built for the rotor blade

airfoil at position $\alpha = 0$. Then, the level-set function φ^n in point (x_i, y_j) can be computed as $\varphi^n(x_i, y_j) = \varphi^0(\bar{x}_i, \bar{y}_j)$ for the rotor rotated by angle α^n counterclockwise. Here φ^0 is the level-set function built for the rotor surface line at position $\alpha = 0$ by using the Bézier curve and (\bar{x}_i, \bar{y}_j) is the image of the point (x_i, y_j) after clockwise rotation on the angle α^n . Thus, the level-set function can be recalculated at any time without reconstructing the Bézier curve for each new rotor position.

The cell-face fraction ratios $\vartheta_{i,j}^u$ and $\vartheta_{i,j}^v$ are introduced. They take values in interval $[0, 1]$ and represent the fluid parts of the east and north faces of $\Gamma_{i,j}$, respectively. One-dimensional linear interpolation of $\varphi(x_i, y)$ on the segment $[y_{j-1}, y_j]$ and $\varphi(x, y_j)$ on the segment $[x_{i-1}, x_i]$ is used for the cell-face fraction ratios computing:

$$\begin{aligned}\vartheta_{i,j}^u &= \frac{\min(\varphi_{i,j-1}, \varphi_{i,j})}{\min(\varphi_{i,j-1}, \varphi_{i,j}) - \max(\varphi_{i,j-1}, \varphi_{i,j})}, \\ \vartheta_{i,j}^v &= \frac{\min(\varphi_{i-1,j}, \varphi_{i,j})}{\min(\varphi_{i-1,j}, \varphi_{i,j}) - \max(\varphi_{i-1,j}, \varphi_{i,j})}.\end{aligned}\quad (5)$$

According to the concept of the LS-STAG method, normal Reynolds stress components are sampled on the base mesh (similar to pressure discretization) and shear ones are sampled in the upper right corners of the base mesh cells.

The time integration of the differential algebraic system resulting from continuity and momentum equations sampling in space is performed with a semi-implicit Euler scheme [8]. Predictor step leads to discrete analogues of the Helmholtz equation for velocities prediction at the next time layer. Corrector step leads to discrete analogue of the Poisson equation for pressure correction. After computation of the flow variables, the dynamics equation for the airfoil motion (4) should be solved.

The rotor angular velocity is $\omega = \dot{\alpha}$. So difference analogue of (4) can be written in the following form:

$$I \frac{\omega^{n+1} - \omega^n}{\Delta t} + k\omega^n = M_z^n. \quad (6)$$

The aerodynamic torque at the n -th time step can be computed as follows:

$$\begin{aligned}M_z^n &= \sum_{\text{Cut-cells } \Omega_{i,j}^{\text{ib}}} \left[(x_i^C - X_C) F_{ya}^h|_{i,j}^n - (y_j^C - Y_C) F_{xa}^h|_{i,j}^n \right]. \quad (7)\end{aligned}$$

Here (x_i^C, y_j^C) are coordinates of the center of $\Omega_{i,j}$ cell, (X_C, Y_C) are coordinates of the point around which the airfoil rotates, and $F_{xa}^h|_{i,j}^n$ and $F_{ya}^h|_{i,j}^n$ are the drag and lift forces acting on the solid part of the cut-cell $\Omega_{i,j}$ at the n -th time step:

$$\begin{aligned}F_{xa}^h|_{i,j} &= [n_x \Delta S]_{i,j}^{\text{ib}} \left(p_{i,j} - \nu \frac{\partial u}{\partial x} \Big|_{i,j} \right) \\ &\quad - \nu \text{Quad}_{i,j}^{\text{ib}} \left(\frac{\partial u}{\partial y} \vec{e}_y \cdot \vec{n} \right),\end{aligned}$$

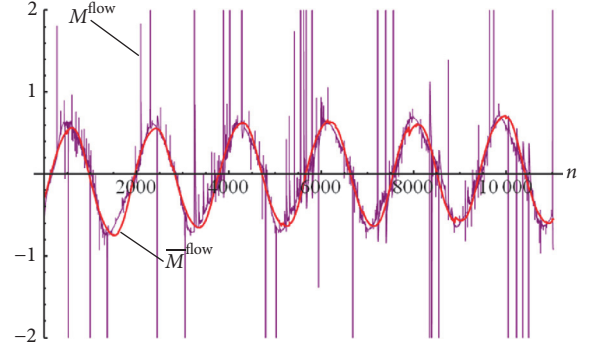


FIGURE 7: The time dependency for the torque $M^{\text{flow}} = M_z(t)$ (on the coarse grid 272×292 with time step $\Delta t = 0.0001$) and filtered time dependency $\bar{M}^{\text{flow}} = \bar{M}_z(t)$ for the torque.

$$\begin{aligned}F_{ya}^h|_{i,j} &= -\nu \text{Quad}_{i,j}^{\text{ib}} \left(\frac{\partial v}{\partial x} \vec{e}_x \cdot \vec{n} \right) \\ &\quad + [n_y \Delta S]_{i,j}^{\text{ib}} \left(p_{i,j} - \nu \frac{\partial v}{\partial y} \Big|_{i,j} \right).\end{aligned}\quad (8)$$

Here $[n_x \Delta S]_{i,j}^{\text{ib}} = (\vartheta_{i-1,j}^u - \vartheta_{i,j}^u) \Delta y_j$, $[n_y \Delta S]_{i,j}^{\text{ib}} = (\vartheta_{i,j-1}^v - \vartheta_{i,j}^v) \Delta x_i$, $\Delta y_j = y_j - y_{j-1}$, $\Delta x_i = x_i - x_{i-1}$, and $\text{Quad}_{i,j}^{\text{ib}}$ are the quadratures of the shear stress which depend on the cut-cells [8].

The value of the rotor angular velocity at the next time step is computed from (6). New rotor position and the immersed boundary velocity can be defined by using this value:

$$\begin{aligned}\alpha^{n+1} &= \alpha^n + \omega^n \Delta t, \\ \mathbf{v}_{i,j}^{\text{ib},n+1} &= \left\{ -\frac{y_j^C - Y_C}{|y_j^C - Y_C|} \cdot \omega^n |x_i^C - X_C|, \frac{x_i^C - X_C}{|x_i^C - X_C|} \right. \\ &\quad \left. \cdot \omega^n |y_j^C - Y_C| \right\}.\end{aligned}\quad (9)$$

Such approach allows reconstructing the level-set function and all matrices and the source terms required for the next time step.

When investigating some complicated physical phenomenon, preliminary qualitative estimations for the considered construction behavior are very important. They allow finding domains for grid refinement, prediction of the structure's dynamic, and estimation of the CFL number. But large fluctuations in the aerodynamic loads can occur on the coarse grid. So the values of the torque acting on the airfoil should be filtered by the low-pass filter (Figure 7). For this purpose, a second-order Butterworth low-pass filter [16] is designed.

It is necessary to explain the reasons for choosing this filter. Filters with infinite impulse response are less expensive from a computational point of view than filters with finite impulse response. The frequency response of the Butterworth filter is maximally flat (i.e., has no ripples) in the passband

and rolls off towards zero in the stopband [16]. Compared with a Chebyshev type I/type II filter or an elliptic filter, the Butterworth filter has a slower roll-off and thus will require a higher order to implement a particular stopband specification, but Butterworth filters have a more linear phase response in the passband than Chebyshev type I/type II and elliptic filters can achieve [16].

The transfer function of the Butterworth second-order filter is as follows:

$$H(s) = \frac{1}{(s - (i-1)/\sqrt{2\varepsilon_p})(s + (i+1)/\sqrt{2\varepsilon_p})} \quad (10)$$

$$= \frac{\varepsilon_p}{1 + \sqrt{2\varepsilon_p}s + \varepsilon_p s^2}.$$

Here $s \in \mathbb{C}$, $i = \sqrt{-1}$, $\varepsilon_p = \sqrt{10^{R_p/10} - 1}$, and R_p is a distortion level in the passband. As practice shows, filters of higher order can lead to the appearance of numerical instability in the filtered signal. For this function, $H(0) = \varepsilon_p$. Therefore the following transfer function corresponds to the normalized Butterworth second-order filter:

$$H^{\text{norm}}(s) = \frac{1}{1 + \sqrt{2\varepsilon_p}s + \varepsilon_p s^2}. \quad (11)$$

In order to control the filter cutoff frequency, it is necessary to use the following transfer function:

$$H_{\text{LP}}(s) = H^{\text{norm}}\left(\frac{s}{\Omega_x}\right). \quad (12)$$

The sampling frequency of the torque is equal to $f_d = 1/\Delta t$ in the numerical simulation (Δt is a time discretization step). It is necessary that the filter cut-off frequency is equal to $f_s = 5$ Hz and the suppression level on the cut-off frequency is equal to $R_s = 3$ dB. So, the following condition imposed on the required filter frequency response function $|H_{\text{LP}}(i \cdot \omega)|$ (Figure 8) must be satisfied for the required filter transfer function $H_{\text{LP}}(s)$:

$$|H_{\text{LP}}(i \cdot \Omega_s)| = \gamma = 10^{-R_s/20}, \quad (13)$$

$$\Omega_s = \tan\left(\frac{\pi f_s}{f_d}\right) = \tan(\pi f_s \Delta t).$$

Solution of (13) leads to the following result:

$$\frac{1}{\sqrt{1 + (\sqrt{\varepsilon_p}/\Omega_x)^4 \Omega_s^4}} = \gamma \iff \quad (14)$$

$$\frac{\sqrt{\varepsilon_p}}{\Omega_x} = \frac{\sqrt[4]{1 - \gamma^2}}{\sqrt{\gamma} \Omega_s} = \xi.$$

Thus, the desired filter transfer function can be written as follows:

$$H_{\text{LP}}(s) = \frac{1}{1 + \sqrt{2}\xi s + (\xi s)^2}. \quad (15)$$

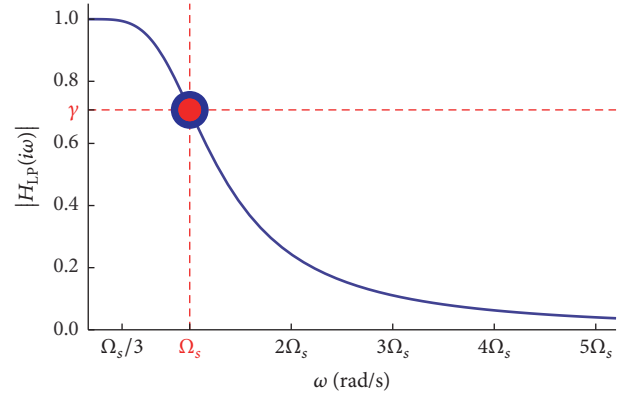


FIGURE 8: The required filter frequency response function.

To obtain the corresponding digital filter coefficients, there is a need to use the bilinear transformation [16]:

$$H_{\text{LP}}\left(\frac{1-z^{-1}}{1+z^{-1}}\right) \quad (16)$$

$$= \frac{1 + 2z^{-1} + z^{-2}}{(1 + \sqrt{2}\xi + \xi^2) + 2(1 - \xi^2)z^{-1} + (1 - \sqrt{2}\xi + \xi^2)z^{-2}}.$$

Here $z \in \mathbb{R}$. It is known that

$$H_{\text{LP}}\left(\frac{1-z^{-1}}{1+z^{-1}}\right) = \frac{b_0 + b_1 z^{-1} + b_2 z^{-2}}{1 + a_1 z^{-1} + a_2 z^{-2}} \quad (17)$$

for the second-order low-pass filter with infinite impulse response. Therefore, it can be obtained from formulae (16) and (17) that the designed digital filter coefficients are the following:

$$b_0 = b_2 = \frac{1}{1 + \sqrt{2}\xi + \xi^2},$$

$$b_1 = \frac{2}{1 + \sqrt{2}\xi + \xi^2},$$

$$a_1 = \frac{2(1 - \xi^2)}{1 + \sqrt{2}\xi + \xi^2}, \quad (18)$$

$$a_2 = \frac{1 - \sqrt{2}\xi + \xi^2}{1 + \sqrt{2}\xi + \xi^2}.$$

So, the filtered value of the torque acting on the airfoil from the flow at the time $t_{n+1} = (n+1)\Delta t$ is

$$\overline{M}_z^{n+1} = b_0 \cdot M_z^{n+1} + b_1 \cdot M_z^n + b_2 \cdot M_z^{n-1} \quad (19)$$

$$- (a_1 \cdot \overline{M}_z^n + a_2 \cdot \overline{M}_z^{n-1}).$$

4. Numerical Experiments

We considered autorotation of Savonius rotor with two blades (Figure 5) at $\text{Re} = 1.96 \cdot 10^5$. The radius of rotation R was

measured from the axis of rotation to the outer edge of the buckets. The turbine-swept area A_s is equal to πR^2 . Reynolds number is based on rotor diameter. The following parameters were used in the simulation:

$$\begin{aligned} V_\infty &= 1.0, \\ R &= \frac{D}{2} = 1.0, \\ \bar{D} &= 0.1D, \\ h &= 0.05R, \\ k &= 0.0, \\ I &= 10.0, \\ \alpha_0 &= \alpha(0) = \frac{\pi}{18}. \end{aligned} \quad (20)$$

It should be noted that the above-proposed algorithm for level-set reconstruction can be easy to apply for rotors of other shapes, that is, Darrieus rotor.

The dimensionless average rotor angular velocity is in the following range:

$$\bar{\omega} = 0.4, \dots, 1.6. \quad (21)$$

Averaging was carried out over 16 dimensionless time units. This time is enough for the rotor to make full turn with the smallest value of average rotor angular velocity $\bar{\omega} = 0.4$. At the chosen values of the parameters, tip speed ratio is equal to

$$X_\infty = \frac{R\bar{\omega}}{V_\infty} = \bar{\omega}; \quad (22)$$

torque coefficient value \bar{C}_Q is obtained by averaging of nonstationary dependency $C_Q(t)$ over time, where

$$C_Q(t) = \frac{2\bar{M}_z(t)}{\rho V_\infty^2 R A_s} = \frac{2\bar{M}_z(t)}{\pi}. \quad (23)$$

Similarly, the power coefficient \bar{C}_P is obtained by averaging of nonstationary dependency $C_P(t)$ over time, where

$$C_P(t) = \frac{2\bar{M}_z(t)\bar{\omega}}{\rho V_\infty^3 A_s} = \frac{2\bar{M}_z(t)\bar{\omega}}{\pi}. \quad (24)$$

A number of computations have been performed on non-uniform grid 544×496 . The uniform mesh block with space discretization step $\Delta h = D/128$ was used in the vicinity of the rotor. Time discretization step was equal to $\Delta t = 10^{-5}$. Computations were performed on a server based on the Intel C610 platform using the Intel Xeon E5-1620 V3 4-core processor (3.5 GHz) with Hyper-Threading support (8 logical cores). The server is equipped with 16 GB of ECC DDR4-2133 RAM and two hard drives (2 TB), united in a RAID1 disk volume. This server is running Windows Server 2012 R2 operating system. To simulate 1 dimensionless time unit, about 24 hours are required.

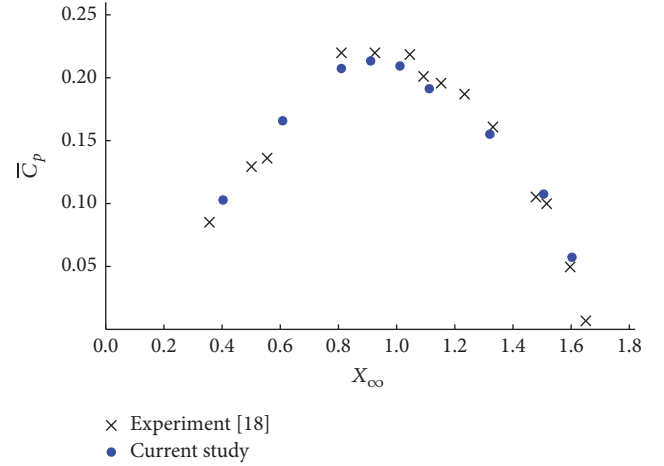


FIGURE 9: Comparison of computed power coefficients \bar{C}_P for a two-bucket Savonius rotor at $Re = 1.96 \cdot 10^5$ with experimental data (Sheldahl et al. [17] at $Re = 3.9 \cdot 10^5$ and Shankar [18] at $Re = 1.96 \cdot 10^5$).

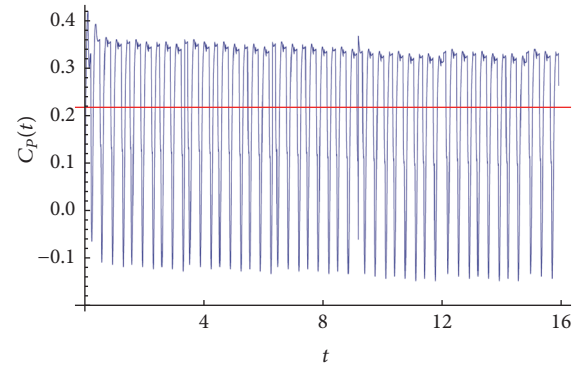


FIGURE 10: Time evolution of the power coefficient $C_P(t)$ at $Re = 1.96 \cdot 10^5$ and $\bar{\omega} = 0.9$. The red line corresponds to the average value \bar{C}_P .

The computed values of the power coefficient \bar{C}_P were compared with the experimental data [17, 18] presented in [18]. As can be seen from Figure 9, the computational results are in good agreement with experiment. An example of simulated nonstationary dependency $C_P(t)$ and computed value of the corresponding power coefficient \bar{C}_P at $Re = 1.96 \cdot 10^5$ and $\bar{\omega} = 0.9$ is shown in Figure 10.

5. Conclusions

We have the following conclusions

- (i) A software package is developed for numerical simulation of wind turbine rotors autorotation by using the modified LS-STAG level-set/cut-cell immersed boundary method. This software package can be used for rotors of other shapes (Savonius rotor, Darrieus rotor, etc.).
- (ii) Algorithms for level-set function construction and recalculation are described.

- (iii) A second-order Butterworth low-pass filter is designed for aerodynamic torque filtering at simulation on the coarse grid.
- (iv) Simulation of flow past autorotating Savonius rotor with two blades is considered at $Re = 1.96 \cdot 10^5$.
- (v) Computational results are in good qualitative agreement with the experimental data.

Conflicts of Interest

The authors declare that there are no conflicts of interest regarding the publication of this paper.

Acknowledgments

This research is partially supported by Russian Ministry of Education and Science (Project no. 9.2422.2017/PP) and Russian Federation President Grant for Young Russian Ph.D. Scientists (Project no. MK-7431.2016.8).

References

- [1] P.-A. Krogstad and J. A. Lund, "An experimental and numerical study of the performance of a model turbine," *Wind Energy*, vol. 15, no. 3, pp. 443–457, 2012.
- [2] N. N. Sorensen, J. A. Michelsen, and S. Schreck, "Navier-stokes predictions of the NREL phase VI rotor in the NASA Ames 80-by-120 wind tunnel," in *Proceedings of the 2002 ASME Wind Energy Symposium*, pp. 94–105, Reno, Nev, USA, January 2002.
- [3] K. Rogowski and R. Maroński, "CFD computation of the savonius rotor," *Journal of Theoretical and Applied Mechanics*, vol. 53, no. 1, pp. 37–45, 2015.
- [4] R. Gupta and K. K. Sharma, "Flow physics of a combined Darrieus-Savonius rotor using computational fluid dynamics (CFD)," *Int. Research J. Eng. Science, Technology and Innovation*, vol. 1, pp. 1–13, 2012.
- [5] L. Oggiano, "CFD Simulations on the NTNU Wind Turbine Rotor and Comparison with Experiments," in *Proceedings of the Renewable Energy Research Conference, RERC 2014*, pp. 111–116, June 2014.
- [6] M. H. Mohamed, A. M. Ali, and A. A. Hafiz, "CFD analysis for H-rotor Darrieus turbine as a low speed wind energy converter," *Engineering Science and Technology, an International Journal*, vol. 18, no. 1, pp. 1–13, 2015.
- [7] R. Mittal and G. Iaccarino, "Immersed boundary methods," in *Annual review of fluid mechanics. Vol. 37*, vol. 37 of *Annu. Rev. Fluid Mech.*, pp. 239–261, Annual Reviews, Palo Alto, CA, 2005.
- [8] Y. Cheny and O. Botella, "The LS-STAG method: A new immersed boundary/level-set method for the computation of incompressible viscous flows in complex moving geometries with good conservation properties," *Journal of Computational Physics*, vol. 229, no. 4, pp. 1043–1076, 2010.
- [9] S. Osher and R. Fedkiw, *Level Set Methods and Dynamic Implicit Surfaces*, vol. 153, Springer, New York, NY, USA, 2003.
- [10] H. A. van der Vorst, "BI-CGSTAB: a fast and smoothly converging variant of BI-CG for the solution of nonsymmetric linear systems," *SIAM Journal on Scientific and Statistical Computing*, vol. 13, no. 2, pp. 631–644, 1992.
- [11] P. Wesseling, *An Introduction to Multigrid Methods*, John Wiley & Sons, Chichester, UK, 1992.
- [12] J. van Kan, C. Vuik, and P. Wesseling, "Fast pressure calculation for 2D and 3D Time dependent incompressible flow," *Numerical Linear Algebra with Applications*, vol. 7, no. 6, pp. 429–447, 2000.
- [13] I. Marchevsky and V. Puzikova, "OpenFOAM iterative methods efficiency analysis for linear systems solving," *Proceedings of the Institute for System Programming of RAS*, vol. 24, pp. 71–86, 2013.
- [14] V. V. Puzikova and I. K. Marchevsky, "Application of the LS-STAG immersed boundary method for numerical simulation in coupled aeroelastic problems," in *Proceedings of the Joint 11th World Congress on Computational Mechanics, WCCM 2014, the 5th European Conference on Computational Mechanics, ECCM 2014 and the 6th European Conference on Computational Fluid Dynamics, ECFD 2014*, pp. 1995–2006, esp, July 2014.
- [15] V. V. Puzikova, "Construction of Level-Set Function for an Airfoil of Arbitrary Topology when Modelling a Flow past It Using the LS-STAG Method," in *Herald of the Bauman Moscow State Technical University. Natural Sciences*, pp. 163–173, 2012.
- [16] R. G. Lyons, *Understanding Digital Signal Processing*, Pearson Education, 2010.
- [17] R. E. Sheldahl, B. F. Blackwell, and L. V. Feltz, "Wind tunnel performance data for two- and three-bucket savonius rotors," *J Energy*, vol. 2, no. 3, pp. 160–164, 1978.
- [18] P. N. Shankar, *National Aeronautical Laboratory, AE-TM-3-76*, National Aeronautical Laboratory, Bangalore, India, 1976.

Research Article

Optimal Sizing for Wind/PV/Battery System Using Fuzzy c -Means Clustering with Self-Adapted Cluster Number

Xin Liu,¹ Hong-Kun Chen,¹ Bing-Qing Huang,² and Yu-Bo Tao³

¹School of Electrical Engineering, Wuhan University, Wuhan 430072, China

²Shandong Electric Power Research Institute, Jinan 250001, China

³State Grid Jiangsu Electric Power Maintenance Branch Company, Nanjing 210013, China

Correspondence should be addressed to Hong-Kun Chen; chkinsz@163.com

Received 24 April 2017; Revised 14 July 2017; Accepted 16 August 2017; Published 26 September 2017

Academic Editor: Yuanzheng Li

Copyright © 2017 Xin Liu et al. This is an open access article distributed under the Creative Commons Attribution License, which permits unrestricted use, distribution, and reproduction in any medium, provided the original work is properly cited.

Integrating wind generation, photovoltaic power, and battery storage to form hybrid power systems has been recognized to be promising in renewable energy development. However, considering the system complexity and uncertainty of renewable energies, such as wind and solar types, it is difficult to obtain practical solutions for these systems. In this paper, optimal sizing for a wind/PV/battery system is realized by trade-offs between technical and economic factors. Firstly, the fuzzy c -means clustering algorithm was modified with self-adapted parameters to extract useful information from historical data. Furthermore, the Markov model is combined to determine the chronological system states of natural resources and load. Finally, a power balance strategy is introduced to guide the optimization process with the genetic algorithm to establish the optimal configuration with minimized cost while guaranteeing reliability and environmental factors. A case of island hybrid power system is analyzed, and the simulation results are compared with the general FCM method and chronological method to validate the effectiveness of the mentioned method.

1. Introduction

Hybrid power systems (HPS) [1, 2], especially those dependent on renewable energy generations (REGs), such as solar photovoltaic (PV), together with wind turbine generations (WTGs), have been regarded as the most promising configurations for remote areas power supply, since it is neither economical nor practical for delivering power over long distances. Although these clean energies provide significant contributions and opportunities, the unpredictable nature [3] of these resources has posed serious challenges to power systems [4, 5]. In the context of remote HPS, the greatest obstacle is to maintain power balance, because the adjustable capacity depends merely on REGs and batteries [6]. Hence, the dynamic characteristic of the wind speed and solar irradiance, together with the power management of batteries, should be investigated to obtain practical configurations for HPS.

In previous literature, various methods have been introduced for sizing optimization of HPS. The stochastic nature of the REGs has been investigated with several probabilistic and

chronological methods. The autoregressive moving average (ARMA) is utilized to model the uncertainties of wind generation, photovoltaic (PV) power, and load in [3, 7, 8]. However, methods for parameters estimation of ARMA are always somewhat cumbersome. Reference [9] put forward an efficient approach for sizing optimization in a stand-alone HPS with Hybrid Big Bang-Big Crunch algorithm. Reference [10] analyzed the different results obtained by four heuristic algorithms; nevertheless the uncertainties of renewable energies have not been considered detailedly. Reference [11] suggested a method for technical and economic optimization in an isolated PV system; the solar radiation classification and power supply reliability calculation are performed hourly. However, only the cluster corresponding to the minimum solar radiation is selected, which may not be suitable in the context of HPS. The other investigations are based on gross chronological data [12, 13] where the computation time is always too unbearable. In [14], the traditional fuzzy c -means (FCM) is adopted, which divides the data of wind speed, solar radiation, and load evenly. Thus the inherent characteristics of the data are handled in a somewhat arbitrary way.

This proposed methodology will be complementary to the previous studies and take a step further. First of all, time series analysis [15] was used to describe the characteristic of hourly wind and solar and load data with FCM, the function of which is to group the elements of data sets that have analogous characteristics. Considering that FCM is sensitive to the initialization number of clusters [16], a parameters self-adaptive method is introduced to optimize the initial state. Furthermore, the Markov model [17] is combined to obtain the system scenarios of HPS. Then the correlation and time dependency of data sets are maintained with the time-dependent clusters of the renewable generations and load power consumption. The optimal sizes for WTGs, PV, DG, and batteries are determined with the genetic algorithm (GA), in which a power balance strategy is designed to ensure that the capitalized and operational costs are minimized and the reliability requirements, CO₂ emission, and batteries constraints are preserved at the same time.

The remaining parts of the article can be demonstrated in the following manner. The models of the components in HPS and the technique of FCM with self-adapted clustering number are introduced in Section 2. Section 3 presents the objective function and constraints for optimal sizing method in HPS. Section 4 utilizes a case of stand-alone hybrid system located in Hainan, China, to verify the advantage of the proposed methodology, where the comparison between the self-adapted FCM model and the traditional model with chronological data is analyzed. In Section 5, conclusions are summarized and the relationship between reliability and cost is discussed.

2. Models of the Components in HPS

2.1. The Components in HPS

2.1.1. WTGs Generation System. The output power of each WTG [10, 18] is obtained by (1), and the power curve of IEC 61400-12 standard is displayed in Figure 1.

$$P_W(t) = \begin{cases} 0, & 0 \leq v \leq v_{ci}, \\ av^3(t) - bp_r, & v_{ci} \leq v \leq v_r, \\ p_r, & v_{ci} \leq v \leq v_{co}, \\ 0, & v_{co} \leq v. \end{cases} \quad (1)$$

The parameters a and b are calculated by

$$a = \frac{p_r}{(v_r^3 - v_{ci}^3)}, \quad (2)$$

$$b = \frac{v_{ci}^3}{(v_r^3 - v_{ci}^3)},$$

where v denotes the rated wind speed, v_{ci} and v_{co} are, respectively, the cut-in wind speed and cut-off wind speed. p_r means the rated power of WTGs.

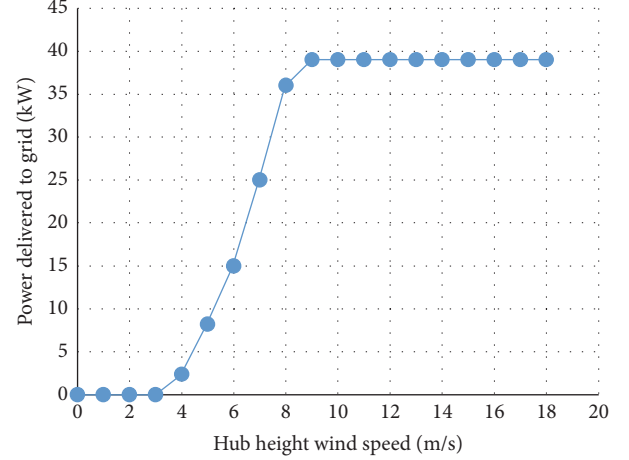


FIGURE 1: Power curve of IEC 61400-12 standard.

The overall wind power P_W^t can be derived with (3), and the total wind energy E_W^t can be obtained with (4):

$$P_W^t = N_W \times p_W^t, \quad (3)$$

$$E_W^t = P_W^t \times \Delta t, \quad (4)$$

where N_W is the number of wind turbines and Δt is the time step.

2.1.2. PV System. For each PV panel, the output power can be obtained [10] with

$$p_{PV} = p_{pvr} \times \left(\frac{G}{G_{Ref}} \right) \times [1 + \alpha_T (T_c - T_{Ref})], \quad (5)$$

where $p_{PV}(t)$ denotes the PV module power at time t . p_{pvr} means the rated power, G means the solar irradiance, and G_{Ref} means the referenced solar irradiance, in 1000 W/m². T_{Ref} means the referenced temperature on the surface of panels, which can be set to be equal to 25°C. α_T means the temperature-coefficients of PV panels, and it can be set to be equal to -3.7×10^{-3} . The temperature T_c of each cell is deduced with

$$T_c = T_{air} + \left(\left(\frac{(T_{stc} - 20)}{800} \right) \times R \right), \quad (6)$$

where T_{air} is the atmospheric temperature. R means the solar irradiance and T_{stc} means the standard operation cell temperature and set to be 25°C.

The overall wind power P_{PV}^t can be obtained with (7), and the total wind energy E_{PV}^t can be calculated with (8):

$$P_{PV}^t = N_{PV} \times p_{PV}^t, \quad (7)$$

$$E_{PV}^t = P_{PV}^t \times \Delta t, \quad (8)$$

where the number of PV panels is given with N_{PV} .

2.1.3. Battery Bank and the Power Balance Strategy. To accommodate the stochastic behavior of PV and wind resources, battery banks are widely utilized for hybrid power systems. The power balance strategy is mainly based on the flexibility of batteries and diesel generations. The diesel generator in [14] is the only adjustable power generation without consideration of storage devices. Thus the power balance strategy is limited to only one pattern, namely, the diesel generators run to make up for the power shortage of renewable energies. To maximize the utilization of REG and minimization of diesel generation, a power balance strategy is illustrated in Figure 2.

2.2. FCM with Self-Adaptive Cluster Number. In this section, FCM clustering is modified to identify the operation state of HPS. The calculation complexity can be significantly optimized considering the number of states will be much less than the 8760 h in the chronological methods. Traditional FCM clustering algorithm can only deal with a prescribed data set with clustering number given in advance, which is not flexible in the context of large data sets. A new validity function [19] is introduced to construct the proportion of compactness and divergence; thus the cluster number can be obtained according to the given data set.

2.2.1. FCM Clustering for HPS. The FCM clustering algorithm established by Dunn and then further improved by Bezdek has been used extensively.

The given data set is divided into c clusters relating to some given criterions to optimize an objective function. The problem can be formulated as

$$\begin{aligned} \min J_m(U, V) &= \sum_{i=1}^c \sum_{j=1}^n u_{ij}^m d_{ij}^2, \\ \sum_{i=1}^c u_{ij} &= 1, \quad 1 \leq j \leq n. \end{aligned} \quad (9)$$

An effective partition of a given data set should be divergent and compacted. The degree of compactness and divergence are evaluated with a clustering validity function. Hence, a new validity function is adopted in

$$L(c) = \frac{\sum_{i=1}^c \sum_{j=1}^n u_{ij}^m \|v_i - \bar{x}\|^2 / (c-1)}{\sum_{i=1}^c \sum_{j=1}^n u_{ij}^m \|x_j - v_i\|^2 / (n-c)}, \quad (10)$$

where m is the fuzzy weighting index and greater than 1 and c means the clustering number. n is the subscript index of the data set X , in which x_j ($j = 1, 2, \dots, n$) is each pattern. x_j ($j = 1, 2, \dots, n$) is the clustering prototype. $\|\cdot\|$ means the statistical distance of the very data set. The central vector of the overall data is given with $\bar{x} = (1/n) \sum_{i=1}^c \sum_{j=1}^n u_{ij}^m x_j$.

2.2.2. Clustering Procedure. Then, the FCM algorithm with self-adapted clustering number is outlined with the proposed validity function $L(c)$. The clustering procedure is illustrated in Figure 3.

The partition matrix $U(0)$ is set as an initial condition; merely two local values of $L(c)$ are required to be compared

since the solution is locally minimized of the object function, which validates the effectiveness of Step 4 in Figure 3.

In [14], the cluster number for WTGs is selected by evenly dividing the range between the cut-in and cut-off wind speed. The selection of cluster number of PV and load is the same. However, the inner uncertain nature of the wind resource may be disregarded by this means, and the accuracy of this method may be reduced significantly.

In this paper, the cluster numbers for WTGs, PV, and load are obtained via the method proposed in Section 3.1. More specifically, the wind speed v , solar irradiance, and load power can be divided into C_{WT} , C_{PV} , and C_{LD} clusters coherently. The cluster centers P_{Wc} , P_{Pvc} , and P_{LDc} are the representative in this cluster, namely, the representative state of wind speed, solar radiation, and load.

2.2.3. The Markov Stochastic Process. In the analysis of a stochastic process, the *Markov* chain is an effective method to relate the probability of a state with the frequency of the corresponding event. The operation states are $P_{WT}(c_{WT})$, $P_{PV}(c_{PV})$, and $P_{LD}(c_{LD})$, where c_{WT} , c_{PV} , and c_{LD} are the state indices obtained by the proposed method in Section 3.1. Take a wind farm with four Markov states as an example, shown in Figure 4. The state transfer probability and failure rate among different states are given with λ and μ , respectively.

If p_c , $c = 1, 2, \dots, C$, are probabilistic for C states (C is the cluster number), then they should satisfy

$$\sum_{c=1}^C p_c = 1, \quad (11)$$

$$[T] [p_1, \dots, p_C]^t = 0.$$

The diagonal elements $T_{c,c}$ are equal to the negative-sum of each off-diagonal element at column c of transition probability matrix φ , and the elements in other positions correspond, respectively, to φ .

$$\begin{aligned} \varphi_{i,j} &= P(X_{t+1} = j | X_t = i), \\ \sum \varphi &= 1, \\ \varphi_{i,j} &= \frac{n_{i,j}}{N_i}, \\ & \quad i \neq j, \end{aligned} \quad (12)$$

where $n_{i,j}$ denotes the transition number from state i to j , and N_i means the number of states i . Rate of departure (RD) is the modulus of the diagonal elements; the frequency (F_i) and duration for state i (D_i) can be formulated as

$$F_i = p_i \sum_{j=1, j \neq i} \varphi_{i,j}, \quad i = 1, 2, \dots, c, \quad (13)$$

$$D_i = \frac{1}{\sum_{j=1, j \neq i} \varphi_{ij}}, \quad i = 1, 2, \dots, c.$$

The system states of HPS are mainly determined by the combination of WT and PV states, which also determine the state of DG and batteries.

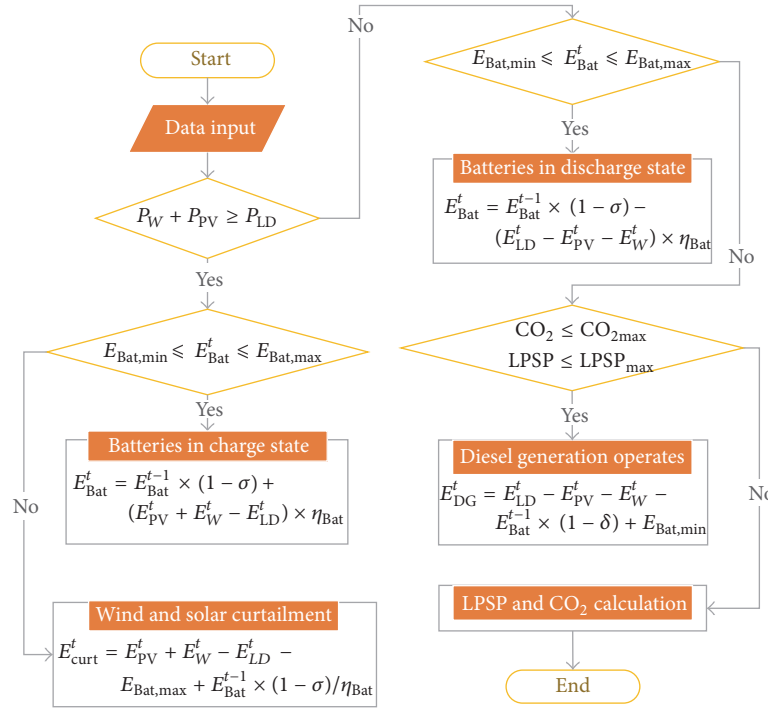


FIGURE 2: Power balance strategy of HPS.

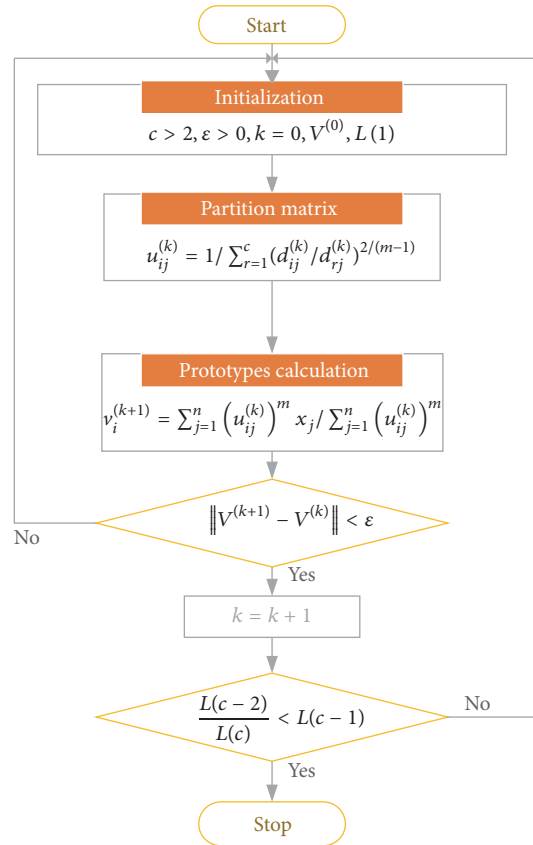


FIGURE 3: Self-adapted clustering procedure.

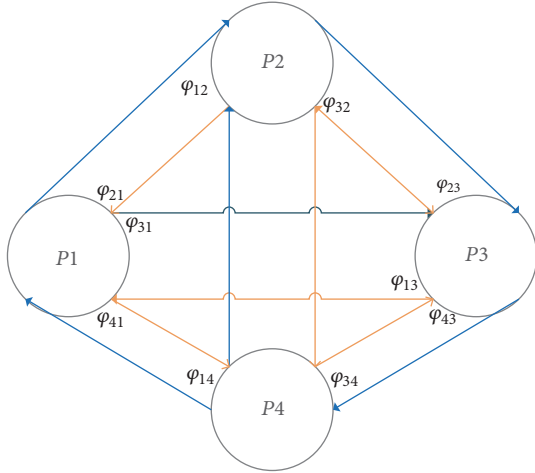


FIGURE 4: Four-state Markov model.

3. Sizing Optimization

3.1. Objective Functions. In the proposed optimal sizing methodology of HPS, the main goal is to determine the amounts of each kind of DG. For a given system load, the objective can be set for the overall cost optimization.

$$\text{Min } CF(x) = \min \sum N_i C_{i,j}, \quad (14)$$

where subscript i denotes the type of generations, namely, WT, PV, DG, and batteries, and j contains the cost of the unit, installation, and fuel consumption of the HPS.

The fuel consumption of the DGs using fossil fuel is given with

$$f(P_d) = a + b \cdot P_d + c \cdot P_d^2. \quad (15)$$

Then the cost model of a diesel generator is

$$C_d = (c_1 \cdot P_{dr} + c_2 \cdot P_{dr} + f(P_d) \cdot c_3) \cdot N_d. \quad (16)$$

For the DGs using renewable energy resources like WG and PV, the operation cost can be ignored. For the DGs using fossil fuel, the operation cost should be accumulated in the studied period. The combustion of fossil fuel will contribute to the emission of CO₂ and gaseous pollutants. The ramping characteristics of diesel generation are neglected in the article since the time resolution is set to be one hour.

In (17), the fuel consumption cost C_d can be obtained.

$$C_{dsum}^{\text{fuel}} = \sum_{h=1}^{8760} C_d^{\text{fuel}}(P_d(h)). \quad (17)$$

By means of FCM clustering, it can be reduced to

$$C_{dsum}^{\text{fuel}} = C_d^{\text{fuel}}(P_d(c')) \times F(c') \times D(c') \times 8760, \quad (18)$$

where P_d can be obtained with the proposed power balance strategy.

3.2. Constraints. On the basis of normal operation in the stand-alone HPS, in order to associate the reliability factor and environmental factors, the main constraints of the proposed methodology are as follows.

3.2.1. Power Balance in the Given Time Resolution. The foundation of the sizing optimization problem is the power balance. The power balance strategy in this paper is illustrated in Figure 2 (power balance strategy of HPS). The power balance equation is

$$\sum_{j=1}^{N_{x,i,t}} P_{i,t,j} = P_{L,t}, \quad (19)$$

where $N_{x,i,t}$ means output power of each kind of DG in the given time interval t , the length of which is associated with the length of the planning period and is set to be 1 h in this paper.

3.2.2. The Minimum and Maximum Scale of the DGs

$$N_i^{\min} \leq N_i \leq N_i^{\max}, \quad (20)$$

where the subscripts max and min mean the maximum and minimum restraints for DG scales, respectively.

3.2.3. Battery Constraints. At time t , the value of charge level for each battery bank should satisfy

$$E_{\text{Bat,min}} \leq E_{\text{Bat}}(t) \leq E_{\text{Bat,max}}. \quad (21)$$

The battery banks capacity (S_{Bat}) sets the maximum value of charge level ($E_{\text{Bat,max}}$) and the depth of discharge (DOD) determines the minimum value of charge level for the batteries ($E_{\text{Bat,min}}$).

$$E_{\text{Bat,min}} = (1 - \text{DOD}) \times S_{\text{Bat}}. \quad (22)$$

3.2.4. Reliability Index. LPSP (loss of power supply probability) is selected for its simplicity, which can be derived from the division of total time of power unbalance and the studied period with

$$\text{LPSP} = \frac{\sum_{t=1}^{\text{TP}} (E_{\text{Load}}(t) - E_{\text{Gen}}(t))}{\sum_{t=1}^T E_{\text{Load}}(t)}. \quad (23)$$

The subscript “max” signifies the maximum limits.

3.2.5. Environmental Factors. The CO₂ emission of the DGs using fossil fuel can be obtained with (24), when considering it in the total period, and should be constrained by a maximum CO₂^{max}.

$$\text{CO}_2 = d + e \cdot Pd + f \cdot Pd^2 \quad (24)$$

$$\text{CO}_2 \leq \text{CO}_2^{\max}. \quad (25)$$

In this article, d , e , and f of a 30-kW diesel generator are set to be 0.028144, 0.001728, and 0.0000017.

3.3. Using Genetic Algorithm to Get Optimal Solution. The genetic algorithm (GA) is chosen to solve the sizing problem considering its ability to obtain a globally optimal solution for optimization problems. It is inspired by the process

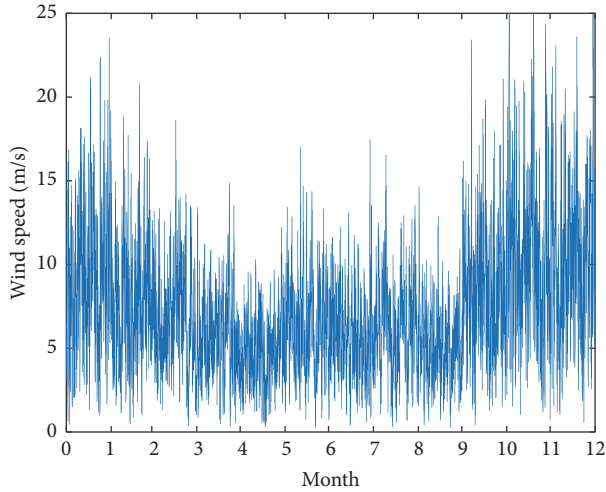


FIGURE 5: Wind speed.

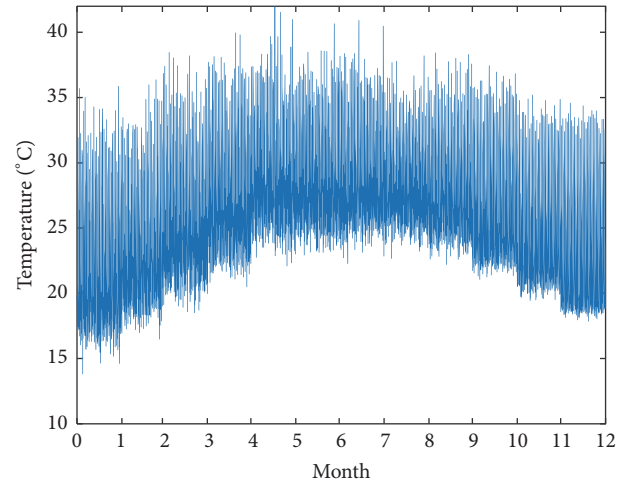


FIGURE 7: Temperature.

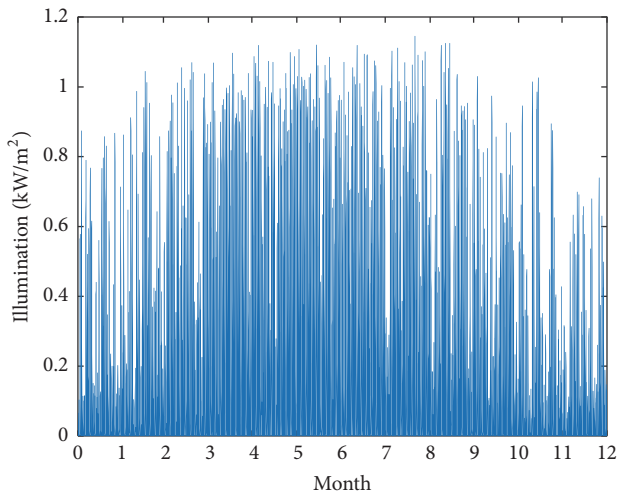


FIGURE 6: Illumination rate.

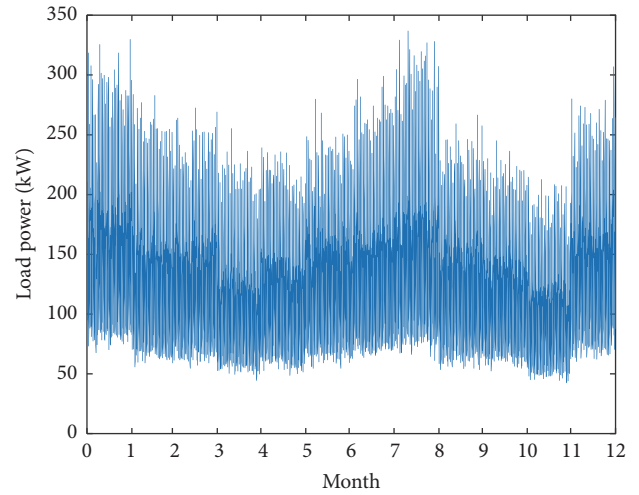


FIGURE 8: Load profile.

of biological evolution, namely, crossover, mutation, and selection. The population of individual solutions is repeatedly modified with a “fitness” function, typically related to the objective function.

In this article, the optimization problem (14)~(25) is handled with GA, where the variables N_{WT} , N_{PV} , N_{DG} , and N_{BAT} are linked to form the gene strings in the state variable (chromosome), and (14) is set to be the fitness function.

4. Results

4.1. Case Introduction. The data from an island in Hainan province of China are used to analyze the proposed problem. There are abundant wind and solar resources in this island.

4.2. Simulation Results and Analysis. The monthly average wind speed, solar irradiation, temperature, and load power profile consumption are shown in Figures 5–8.

Firstly, the wind speed v , illumination G , and temperature T are imported to the HPS model to obtain the power output

of WTGs (P_W) and PV (P_{PV}). Then the cluster numbers for WT, PV, and load are obtained via the method proposed in Section 2.1. The cluster centers V_c , G_c , and L_c are, respectively, the representative states for wind speed, solar irradiance, and load, illustrated in Tables 1–3.

According to the simulation results from self-adaptive FCM, the optimal cluster numbers for wind WT, PV, and LD are 10, 5, and 8. Namely, each WT has 10 states, each PV has 5 states, and the overall load has 8 states. There are 80 possible states for the renewable energy generations as a whole. It can be noted here that the scenario of HPS has been significantly simplified.

The operation scenario considered here is greatly simplified to be the aggregation of clustering states. The outputs of DGs and batteries are also determined by these states, according to the power balance strategy demonstrated before.

For a new state, the probability is the multiplication of state probabilities for every individual WTG, PV, and LD. The frequency F and duration time D for a new scenario can be obtained likewise.

TABLE 1: Markov model of WT/35 kW.

State (c1)	Pw/kW	ps	RD	$F/(oc \cdot h^{-1})$	D (h)
1	0.20	0.08	0.47	0.03	2.15
2	3.90	0.09	0.65	0.05	1.53
3	7.48	0.15	0.52	0.08	1.92
4	10.99	0.08	0.82	0.07	1.22
5	14.56	0.08	0.59	0.05	1.69
6	18.08	0.09	0.62	0.12	1.61
7	21.86	0.09	0.85	0.08	1.18
8	25.89	0.06	0.72	0.06	1.39
9	30.19	0.09	0.84	0.08	1.20
10	34.87	0.19	0.76	0.07	1.32

TABLE 2: Markov model of PV/200 W.

State (c1)	P_{PV}/W	ps	RD	$F/(oc \cdot h^{-1})$	D (h)
1	1.37	0.61	0.37	0.22	2.71
2	83.14	0.10	0.62	0.06	1.63
3	37.23	0.13	0.44	0.06	2.29
4	134.05	0.09	0.59	0.05	1.69
5	188.58	0.07	0.26	0.02	3.82

TABLE 3: Markov model of load.

State (c1)	P_{PV}/W	ps	RD	$F/(oc \cdot h^{-1})$	D (h)
1	135.66	0.16	0.67	0.11	1.49
2	83.78	0.18	0.56	0.10	1.77
3	156.19	0.17	0.74	0.13	1.34
4	217.17	0.07	0.82	0.05	1.23
5	182.49	0.10	0.63	0.07	1.60
6	63.81	0.17	0.22	0.04	4.46
7	111.11	0.13	0.51	0.06	1.96
8	268.08	0.03	0.28	0.01	3.61

Then the results from chronology-based, traditional FCM based, and the self-adapted clustering number based GAs are compared; results are illustrated in Table 4. GA is capable of realizing global optimization but cannot guarantee it. The chronological-based method requires 8760 iterative loops, and the traditional FCM based method needs 920 ($=23 * 4 * 10$) iterative loops, and the proposed method needs 400 ($=10 * 5 * 8$) iterative loops.

It should be noted that the wind energy is superfluous in the winter nights. The output power of PV panels is redundant in the summer daytimes.

It can be found that chronology-based method is the most time-consuming due to complicate loops. With regard to the overall cost, the proposed method still has advantages. Figure 9 shows the iteration performance for the mentioned algorithms.

The proposed self-adapted FCM clustering model is superior to traditional method in two aspects:

- (1) Compared to chronological-based methods, with the reduction of investigated data set, the number of system scenarios of HPS can be significantly reduced,

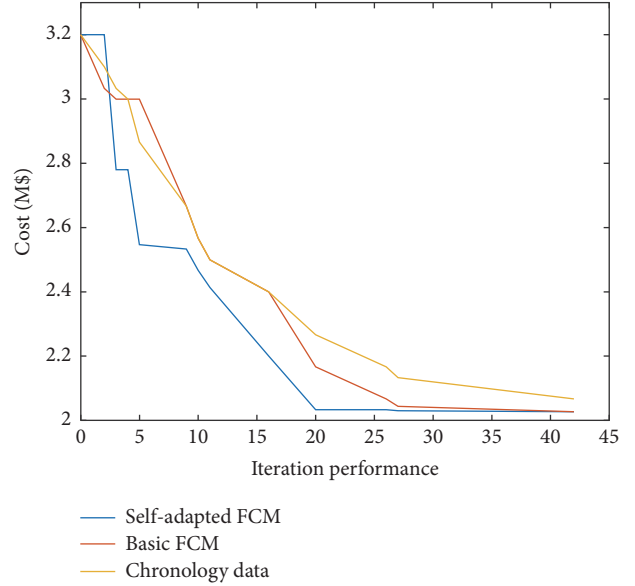


FIGURE 9: Iteration performance comparison.

and the computation burden and CPU time can be significantly reduced, shown in Table 4.

- (2) Compared to the traditional FCM based method, the clustering numbers of data sets are inherently obtained and optimized, which increases the probability to obtain a global optimum solution. While the traditional method simply makes the partition by uniform division, the scenarios selection is somewhat arbitrary and disregards the inner stochastic characteristic of the data sets. Thus the basic FCM based method finally obtains a locally optimized solution.

In the proposed method, the benefits of the renewable energies are thought to be the reduction of CO_2 and the improvement of LOSP, which has been set as constraint to the very problem. Considering the impacts of different reliability index on the investment cost, let CO_2^{\max} be 30000 kg/y. The overall investment cost grows higher as the reliability request ($LPSP_{\max}$) increases, as shown in Figure 10. The impact of CO_2 is similar to the $LPSP$ index.

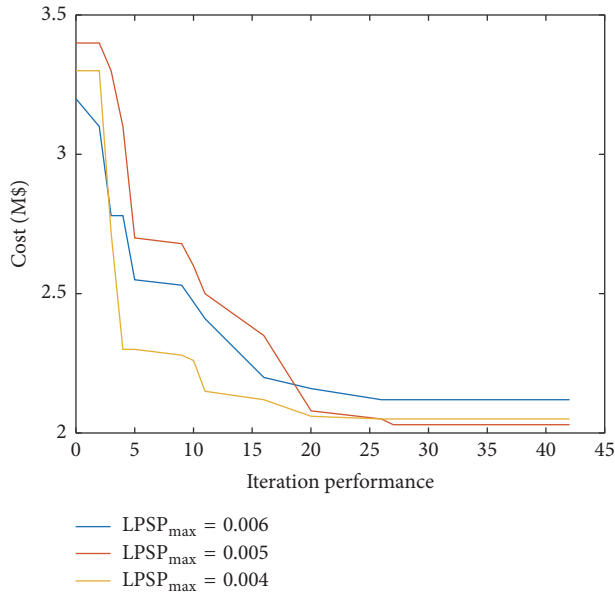
Actually, the benefits of the reduction of CO_2 and the improvement of LOSP are negatively related to the cost optimization procedure. We have modified the discussion on this issue in our revised manuscript.

5. Conclusion

In this paper, a novel method utilizing the self-adapted FCM clustering combined with the Markov model and GA is proposed to determine the best mix of HPS. A power balance strategy is also designed to guide the optimization process. The self-adapted FCM clustering can handle the stochastic characteristics of REGs, and the Markov model can significantly reduce the operational scenarios of REGs. The proposed method has comparable competitive overall cost, and it can be concluded that the benefits of the reduction of

TABLE 4: Performance comparison.

Method	N_w	N_{PV}	N_d	N_{bat}	Cost/M\$	CO ₂ /kg	Time/s
Proposed method	15	126	62	864	2,03M	556,000	27.5
Basic FCM	10	96	56	956	2.20M	542,000	27.8
Chronology-based	13	104	64	886	2.06M	560,000	126

FIGURE 10: Sensitivity analysis of $LPSP_{max}$ and cost.

CO₂ and the improvement of LOSP are negatively related to the cost optimization procedure.

The future work will include the following:

- (1) Improving the clustering model to further study the correlation among renewable resources
- (2) Adding the local and global control strategy to the power balance analysis process
- (3) Extending the proposed method to the operation plan stage of the HPS.

Conflicts of Interest

The authors declare that there are no conflicts of interest regarding the publication of this paper.

References

- [1] R.-J. Wai, S. Cheng, Y.-F. Lin, and Y.-C. Chen, "Installed capacity selection of hybrid energy generation system via improved particle-swarm-optimisation," *IET Generation, Transmission and Distribution*, vol. 8, no. 4, pp. 742–752, 2014.
- [2] J. G. McGowan and J. F. Manwell, "Hybrid wind/pv/diesel system experiences," *Renewable Energy*, vol. 16, no. 1-4, pp. 928–933, 1999.
- [3] A. Arabali, M. Ghofrani, M. Etezadi-Amoli, and M. S. Fadali, "Stochastic performance assessment and sizing for a hybrid power system of Solar/Wind/Energy Storage," *IEEE Transactions on Sustainable Energy*, vol. 5, no. 2, pp. 363–371, 2014.
- [4] R. R. Barton, "Presenting a more complete characterization of uncertainty: Can it be done," in *Proceedings of the in Proceedings of the Simulation Society research workshop (INFORMS '07)*, pp. 26–60, 2007.
- [5] E. Ela and M. O'Malley, "Studying the variability and uncertainty impacts of variable generation at multiple timescales," *IEEE Transactions on Power Systems*, vol. 27, no. 3, pp. 1324–1333, 2012.
- [6] A. Keane, L. F. Ochoa, C. L. T. Borges et al., "State-of-the-art techniques and challenges ahead for distributed generation planning and optimization," *IEEE Transactions on Power Systems*, vol. 28, no. 2, pp. 1493–1502, 2013.
- [7] A. Mohamed Abd El Motaleb, S. Kazim Bekdache, and L. A. Barrios, "Optimal sizing for a hybrid power system with wind/energy storage based in stochastic environment," *Renewable and Sustainable Energy Reviews*, vol. 59, pp. 1149–1158, 2016.
- [8] E. Koutroulis, D. Kolokotsa, A. Potirakis, and K. Kalaitzakis, "Methodology for optimal sizing of stand-alone photovoltaic/wind-generator systems using genetic algorithms," *Solar Energy*, vol. 80, no. 9, pp. 1072–1088, 2006.
- [9] S. Ahmadi and S. Abdi, "Application of the Hybrid Big Bang-Big Crunch algorithm for optimal sizing of a stand-alone hybrid PV/wind/battery system," *Solar Energy*, vol. 134, pp. 366–374, 2016.
- [10] A. Maleki and F. Pourfayaz, "Optimal sizing of autonomous hybrid photovoltaic/wind/battery power system with LPSP technology by using evolutionary algorithms," *Solar Energy*, vol. 115, pp. 471–483, 2015.
- [11] K. Benmouiza, M. Tadj, and A. Chekneane, "Classification of hourly solar radiation using fuzzy c-means algorithm for optimal stand-alone PV system sizing," *International Journal of Electrical Power and Energy Systems*, vol. 82, pp. 233–241, 2016.
- [12] M. Mosadeghy, R. Yan, and T. K. Saha, "A time-dependent approach to evaluate capacity value of wind and solar PV generation," *IEEE Transactions on Sustainable Energy*, vol. 7, no. 1, pp. 129–138, 2016.
- [13] L. Xu, X. Ruan, C. Mao, B. Zhang, and Y. Luo, "An improved optimal sizing method for wind-solar-battery hybrid power system," *IEEE Transactions on Sustainable Energy*, vol. 4, no. 3, pp. 774–785, 2013.
- [14] Y.-Y. Hong and R.-C. Lian, "Optimal sizing of hybrid wind/PV/diesel generation in a stand-alone power system using markov-based genetic algorithm," *IEEE Transactions on Power Delivery*, vol. 27, no. 2, pp. 640–647, 2012.
- [15] S. N. Gopiya Naik, D. K. Khatod, and M. P. Sharma, "Analytical approach for optimal siting and sizing of distributed generation in radial distribution networks," *IET Generation, Transmission and Distribution*, vol. 9, no. 3, pp. 209–220, 2015.
- [16] X. Yejun, "Fitzwilliam College," in *Proceedings of the 10th International Conference on Computer Science & Education (ICCSSE'15)*, pp. 22–24, Fitzwilliam College, Cambridge University, Cambridge, UK, 2015.

- [17] A. S. Dobakhshari and M. Fotuhi-Firuzabad, "A reliability model of large wind farms for power system adequacy studies," *IEEE Transactions on Energy Conversion*, vol. 24, no. 3, pp. 792–801, 2009.
- [18] L. Chen, H. Chen, Z. Shu, G. Zhang, T. Xia, and L. Ren, "Comparison of inductive and resistive SFCL to robustness improvement of a VSC-HVDC system with wind plants against DC fault," *IEEE Transactions on Applied Superconductivity*, vol. 26, no. 7, pp. 1–8, 2016.
- [19] Y. Li and F. Yu, "A new validity function for fuzzy clustering," in *Proceedings of the International Conference on Computational Intelligence and Natural Computing (CINC '09)*, vol. 1, pp. 462–465, IEEE, June 2009.

Research Article

Variable Ratio Hydrostatic Transmission Simulator for Optimal Wind Power Drivetrains

Jose M. Garcia-Bravo,¹ Ivo N. Ayala-Garcia,² and Juan L. Cepeda-Aguilar³

¹Purdue University, West Lafayette, IN, USA

²Universidad Tecnológica de Querétaro, Santiago de Querétaro, QRO, Mexico

³Universidad de los Andes, Bogotá, Colombia

Correspondence should be addressed to Jose M. Garcia-Bravo; jmgarcia@purdue.edu

Received 20 May 2017; Accepted 20 July 2017; Published 28 August 2017

Academic Editor: Lei Chen

Copyright © 2017 Jose M. Garcia-Bravo et al. This is an open access article distributed under the Creative Commons Attribution License, which permits unrestricted use, distribution, and reproduction in any medium, provided the original work is properly cited.

This work presents a hydromechanical transmission coupled to an electric AC motor and DC generator to simulate a wind power turbine drive train. The goal of this project was to demonstrate and simulate the ability of a hydrostatic variable ratio system to produce constant electric power at varying wind speeds. The experimental results show that the system can maintain a constant voltage when a 40% variation in input speed is produced. An accompanying computer simulation of the system was built and experimentally validated showing a discrete error no larger than 12%. Both the simulation and the experimental results show that the electrical power output can be regulated further if an energy storage device is used to absorb voltage spikes produced by abrupt changes in wind speed or wind direction.

1. Introduction

Wind power generators are a technology that contributes to sustainable energy and low impact to the environment. However, some of the challenges that the current wind power industry face are high installation and maintenance costs and reliability issues [1–4]. To be able to reduce the cost of wind power energy in general, the wind power industry must invest resources in developing wind power technologies that decrease the total cost of the produced energy. This can be done if wind power turbines operate efficiently at broader wind speed ranges, while maintaining optimum electrical generator shaft speeds, so they can generate more electric power regardless of the wind speed. There is a great impact on the turbine reliability when major components of the wind power turbine like the gearbox or the generator fail because this creates an extended mean time to repair (MTTR) [4–6]. Therefore, reducing failure and maintenance of these major components reduces the cost of operation of the wind power turbine, which in turn reduces the cost of energy itself.

The power coefficient C_p in (1) is a parameter used for measuring the efficiency of the wind energy captured by the

turbine; this coefficient represents the ratio of the mechanical power output of the turbine to the power input from the wind.

$$C_p = \frac{\eta_d}{\eta_m \eta_g}. \quad (1)$$

η_d is the aerodynamic efficiency of the turbine and η_m and η_g are the electric generator efficiency and the gearbox efficiency, respectively [7]. The maximum theoretical achievable C_p is 59%; this condition, which is derived from fluid mechanics principles is known as the Betz limit [7]. The direct consequence of this limit is that no more than 59% of the available power in the wind can be captured.

The tip speed ratio λ (see (2)) is parameter used to define the ratio between the tangential velocity of the blade and the wind speed. The family of plots shown in Figure 1 illustrates the effect of the tip speed ratio on the power coefficient C_p for various pitch angles of the same blade.

$$\lambda = \text{TSR} = \frac{\omega R}{V} = \frac{2\pi RN}{V}, \quad (2)$$

where ω is the rotational speed of the blades, R is the radius of the wind turbine, and V is the wind speed. As

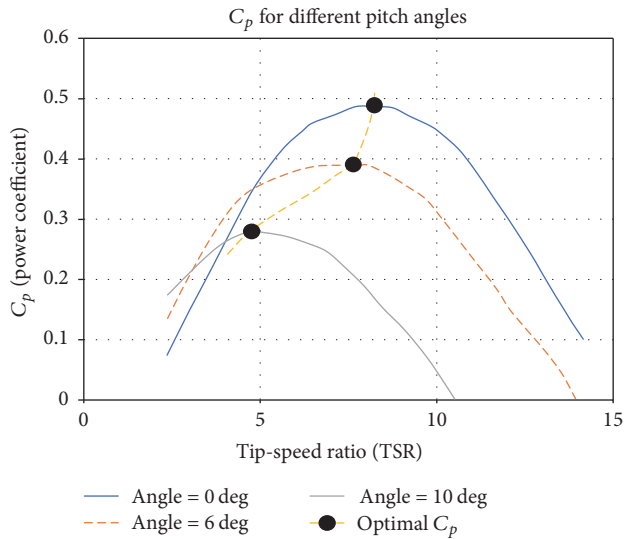


FIGURE 1: Power coefficient versus tip speed ratio [8].

the wind speed varies, the pitch angle of the blade needs to be adjusted to operate at the optimal C_p . Inevitably, when the wind speed varies, the shaft speed of the generator also changes because the rotor's shaft is directly (direct drive) or indirectly (gearbox) coupled to the generator's shaft. That means that the electric generator will produce electric power at variable frequencies that need to be conditioned using power electronics to match the constant frequency standard of the electric grid. The challenge of using this approach is the increased complexity, cost, weight, and size of the wind turbine components and it reduces its efficiency and reliability. Additionally, most common current electric generators operate more efficiently at their constant rated shaft speed, which is normally a single value between 1800 and 2200 RPM. This is particularly true, for field induced generators, but it also affects permanent magnet motors because the amount of power produced is proportional to the input shaft speed.

Various studies [9–15] have proposed the use of hydrodynamic, hydrostatic, or mechanical continuously variable transmissions (CVT) instead of using fixed or variable speed gearboxes; the objectives of incorporating a CVT to replace the gearbox are to improve the overall reliability of the wind turbine, reduce the weight of the nacelle components, reduce down-time, and significantly reduce the cost of installation and operation. The use of power electronics systems used to convert the electric output of the generator with the grid is known [11] to reduce the captured wind power in the 93–94% range for wind speeds between 6 and 11 m/s.

When replacing the fixed ratio mechanical gearbox or the power electronics systems in a wind power drive train with a CVT, the overall efficiency of the turbine will be increased because the generator's shaft will turn at its optimal speed while maintaining an ideal tip speed ratio λ to achieve a maximum power coefficient C_p [7]. While the hydraulic hydrostatic transmission will introduce a power loss due to its overall efficiency of approximately 86–93%, the cost,

reliability, and maintenance benefits of implementing this solution would offset the ~1–12% loss in energetic efficiency.

The hydrostatic transmission will be the focus of this project because it is a technology that has been proven to be reliable and cost effective. Additionally, hydrostatic transmissions allow novel and flexible designs where the generator is placed at the floor level for easier, less costly, and safer maintenance. A hydrostatic transmission is a variable speed rotary drive that consists of one or more positive displacement hydraulic pumps connected to one or more positive displacement hydraulic motors. The main function of the hydrostatic transmission is to convert mechanical power into hydraulic power (pressure and flow) and after transmitting it through piping or hoses convert it back into mechanical power to be used in an application. A hydrostatic transmission fitted with a fixed or a variable displacement (flow) pump and a fix or a variable displacement motor allows the output shaft to deliver a nearly constant power at varying speeds, similar to the requirement for wind power turbines.

The work by Thul et al. [9] provided theoretical evidence that these types of transmissions would dampen the large torque impulses created from wind gusts and turbulence, which translates into lower loads on the bearings of the generator, therefore increasing their life. Preliminary simulation results from Thul et al. [9] and Yang et al. [12] revealed that a wind power turbine fitted with pitch control and or a continuously variable transmission could operate at an optimal power coefficient even at speeds close to the cut in speed (minimum operating speed); this would allow capturing more energy from the wind at these lower speeds and capturing more power at the turbine's rated speed.

The main challenge for using hydrostatic transmissions in wind power generation is the lack of pumps and motors that can match the power requirements of current mid-sized (250 kW to 750 kW) and large sized wind power turbines (750 kW or more); most of the larger displacement pumps are rated for a little less than 250 kW. Researchers investigating the use of hydrostatic transmissions for wind power use have recurred to three alternatives: (1) limiting the wind power capacity to less than 250 kW [9], (2) using more than one pump and more than one motor to meet the flow requirements of larger size wind turbines [11], and (3) designing hydrostatic transmissions with an experimental large displacement pump. Wind power turbines larger than 150 kW are typically fitted with three phase alternating current (AC) generators at 690 V; this current is then sent to a transformer to increase the voltage several thousand volts up to 30,000 volts, making it up for transmission in high voltage lines [16].

The aim of this project was to design, build, and test a small scale experimental bench system with the flexibility to simulate various wind speed profiles. At the same time, the principal objective was to integrate control algorithms for measuring and demonstrating a variable ratio hydrostatic transmission.

The design of the simulator encompasses two associated fields: hydraulics and electrical systems. The first system is involved in the transmission of the mechanical energy from the wind turbine into the electrical generator by using a hydrostatic transmission. The second system, is in charge of

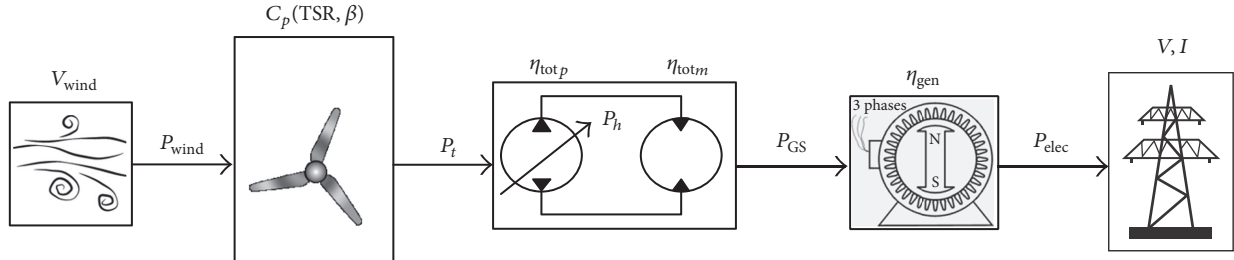


FIGURE 2: Power flow through the system.

controlling the different gear ratio of the system to maintain a constant voltage output and also adjusting the simulated wind speed.

2. Theoretical Approach

This study section focuses on the flow of power through the system, as it is depicted in Figure 2. The magnitude of the power available in the wind P_{wind} is quantified using the expression in

$$P_{wind} = \frac{1}{2} \rho A V^3, \quad (3)$$

where ρ is the density of the air at the altitude at the wind turbine is location, A is the transversal area that is being passed by the wind, in this case the area swept by the blades while it is spinning, and V is the velocity of the wind.

The power that the turbine extracts from the wind (P_t), as it was mentioned in the background section, is calculated using the power coefficient using (3):

$$P_t = C_p(TSR, \beta) P_{wind} = \frac{1}{2} C_p \rho A V^3. \quad (4)$$

The power extracted by the turbine is equal to the power on the shaft, if the rotor is assumed to be rigid (no torsion).

$$P_t = \omega_{TS} T_{aero}. \quad (5)$$

Then, the mechanical power from the rigid shaft is converted into hydraulic power by a hydrostatic pump.

$$P_h = \eta_{p_{tot}} P_t. \quad (6)$$

And the hydraulic power is defined as

$$P_h = \Delta p Q. \quad (7)$$

The total efficiency of the pump ($\eta_{p_{tot}}$) is the product between the volumetric (η_{vol}) and the mechanical (η_{mec}) efficiencies of the pump. The volumetric efficiency of a hydraulic machine is defined as the ratio between the real flow produced and the theoretical flow. Meanwhile, the mechanical efficiency is equal to the ratio between the real torque and the theoretical torque required to drive the pump.

D is the hydraulic machine displacement and n is the shaft speed in RPM.

$$\eta_{vol} = \frac{Q}{Dn}, \quad (8)$$

$$\eta_{mec_p} = \frac{D\Delta p}{T}.$$

Once the fluid is pressurized by the pump, it is transported by the hoses to the hydraulic motor where the power is transformed back into mechanical power and coupled to an electrical generator shaft.

$$P_{GS} = \eta_{tot_m} P_h. \quad (9)$$

The total efficiency in the case of the hydraulic motor is similar to the pump; the total efficiency is the same product between the volumetric and mechanical efficiency. The volumetric efficiency is expressed the same way; the difference is in the mechanical efficiency; the expressions are reversed.

$$\eta_{mec_m} = \frac{T}{D\Delta p}, \quad (10)$$

where T corresponds to the ideal hydraulic machine's shaft torque and ω is the rotational speed. Power on the generator shaft is expressed in the following equation.

$$P_{GS} = \omega_{GS} T_{elec}. \quad (11)$$

Finally, the energy is transformed from mechanical power to electrical power by means of the generator using the electromagnetic theory.

$$P_{elec} = \eta_{gen} P_{GS}. \quad (12)$$

3. Materials and Methods

3.1. Wind Speed. The rotational energy generated by a wind power turbine is proportional to the kinetic energy in the wind. The simulator replaces the wind turbine by a Brook Crompton Americas, 3-phase, 60 Hz, NEMA 56 electric motor (BF4N.33-2). The variation of the kinetic energy of the wind is simulated with the inclusion of a Teco Westinghouse electric inverter (JNEV-101-H1). The electric inverter varies the frequency at the motor power lines from 0 Hz

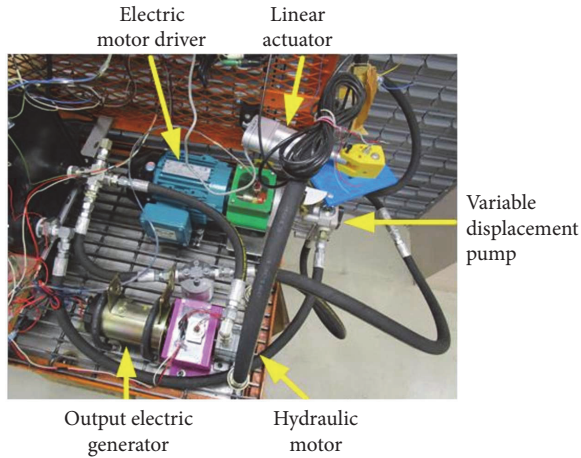


FIGURE 3: Test bench hardware setup.

to its nominal value of 60 Hz, proportionally affecting the rotational shaft speed of the motor between approximately 0 to 1800 rpm. These values of the frequency are assumed to be linearly proportional to the input wind speed, where 0 Hz corresponded to 0 wind speed and 60 Hz corresponded to the maximum permissible wind speed on a small wind power turbine (<50 kW) of approximately 15 m/s.

3.2. Hydraulic System. The electric motor is coupled to a 10.3 cc/rev variable displacement pump (Hydro-Gear, PG-1HCC-DL1X). This is the first component of a hydrostatic transmission, transducing the mechanical power from the electric motor into hydraulic power. The hydraulic power is then transmitted to a fixed displacement hydraulic gear motor (Double A Hydraulics, MFG 2), which converts the hydraulic energy back into mechanical energy. The hydraulic motor is coupled to a permanent magnet generator (GS Electric, B4CPM-102T) which converts the mechanical energy into electrical energy.

The variable displacement hydraulic pump regulates the amount of energy transferred to the hydraulic motor by adjusting the angle of the swashplate, hence adjusting the volumetric flow rate delivered by the pump. Regardless of the mechanical energy generated by the electric motor, the hydraulic power delivered to the hydraulic motor is adjusted to maintain an approximated constant power. The adjustment of the swashplate is accomplished by means of a linear actuator attached to the pump trunnion arm. The simulator regulates the angle according to the amount of the electrical energy required at the output of the DC generator. The rotation of the generator's shaft generates a current proportional to the rotational speed, which in turn is rectified into a DC signal (Figure 3).

3.3. Control. The wind speed is simulated by adjusting the driving frequency of the 3-phase electric motor. The frequency range can be adjusted from 0 to 60 Hz. The actual rotation speed depends on the mechanical load applied at the rotor. The wind profile tested is described in Section 5.

The driving frequency is controlled by using the EI. The frequency can be manually adjusted using a knob or via an analog signal at a predefined input port of the EI. The convenience of using an analog signal to control the frequency relies on the ability to implement an automatic system that programmatically changes the frequency following a given pattern or data set. This feature allows the system to simulate a wind profile.

Mechanical coupling between the electric motor and the hydraulic pump is achieved by the use of a jaw type couplings. These couplings include an elastomer insert between metal hubs. The insertion of the nonmetallic elastomer creates the opportunity to place a proximity sensor (Allen-Bradley, 872C-D3NN12-D4) to measure the rotational speed. A revolution of the rotor is measured by the number of teeth sensed. On a three teeth hub, a full revolution occurs when six teeth are sensed.

The rotational displacement of the rotor is transduced into hydraulic flow and pressure at the variable hydraulic pump. This variable capability is of crucial importance for the system. By adjusting the flow, the energy transduced by the electric generator can be controlled, hence maintaining a constant output voltage independent of the wind speed.

The flow rate at variable hydraulic pump is achieved by adjusting the angle of the swashplate. The swashplate is attached to a trunnion arm that can be externally manipulated to control the flow. A linear actuator is connected to the trunnion arm. The direction and rate of displacement of the actuator are performed by a power driver connected to a personal computer.

The hydraulic pump is connected to a hydraulic motor via hydraulic hoses. A flow meter and pressure sensor measure these two parameters at one of the hoses that connect the pump to the motor. Due to the nature of the system, the hydraulic flow is allowed to go in only one direction.

The hydraulic motor then transfers the energy to an electric generator. The mechanical coupling is accomplished through a jaw type coupling, where the rotational speed is measured using a hall effect sensor (Cherry, MPI1005).

The permanent magnets of the electric generator create the excitation field necessary to induce current on the stationary coil. Additionally, a rectifier circuit converts the resulting AC voltage from the coil into a DC signal which is measured using the voltmeter (Tenma, 72-7735). Figure 4 shows a schematic representation of the hardware components.

3.4. Instrumentation and Control Algorithm. The instrumentation includes two hall effect sensors, a flow meter, and a pressure sensor. All these signals are sensed using a data acquisition card DAQ (NI USB-6221) connected to the personal computer. The multimeter is connected directly to the PC via its serial port.

Two output signals are controlled by the system, driving frequency at the EI, and flow rate at the hydraulic pump. The frequency is adjusted by an analog signal generated at the DAQ card, while the flow rate is controlled by adjusting the length of the linear actuator connected to the trunnion of the hydraulic pump.

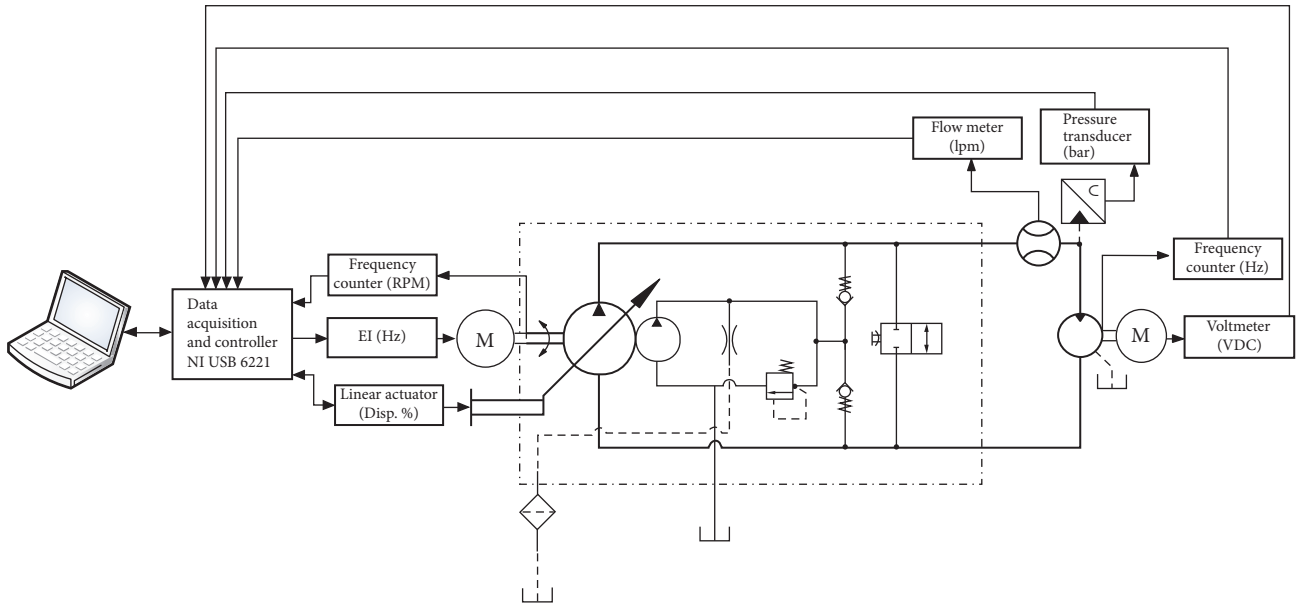


FIGURE 4: Schematic representation of test bench hardware setup.

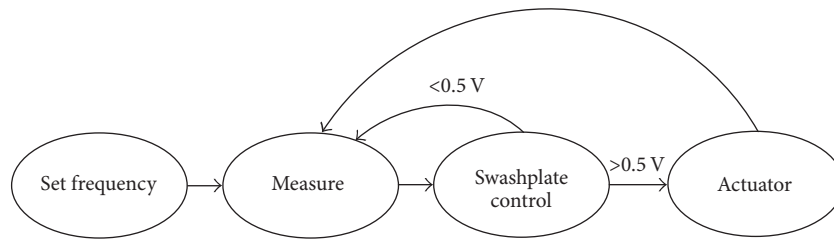


FIGURE 5: Control flow path.

The control algorithm follows a state machine architecture. Each state corresponds to a particular activity in the system as presented in Figure 5. The system starts by setting the desired frequency at the motor driver. This frequency corresponds to a particular simulated wind speed. Then, different variables are measured in the system: selected frequency, revolutions per minute (RPM) at the motor driver, RPM at the generator, hydraulic flow rate, pressure at outlet of the variable displacement pump, actuator position, and voltage at the electric motor.

The control of the variable displacement hydraulic pump is achieved by adjusting the swashplate using a linear actuator. A proportional control commands the adjustment of the actuator stroke length, either reducing or increasing it. The adjustment is performed until the signal error reaches $\pm 0.5\text{ V}$ from the desired output voltage at the DC generator.

4. System Characterization

4.1. Hardware Characterization. The system was characterized to identify its operating range: frequency and DC output voltage. In the first series of tests, the angle of the variable swashplate was kept constant, starting at 25% of its maximum flow, increasing in steps of 25%, up to 100% displacement.

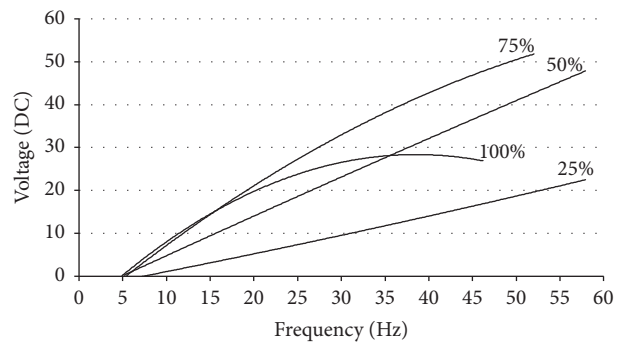


FIGURE 6: Voltage generation at different swashplate angles.

The control system was disabled and the electric load was the voltmeter. Figure 6 shows the polynomial fits of the collected voltage data; the fitted data is shown here to cleanly depict the frequency trends at various pump displacement values. In this figure, it can be seen that at 25% pump displacement the system can generate a maximum of 22 V. The maximum output voltage increases with the swash plate angle, up to 52 V. It is important to notice that increasing the swash plate angle does not necessarily imply reaching a higher output voltage.

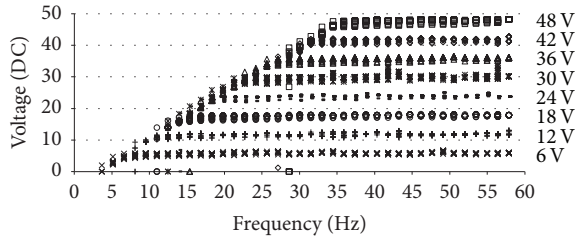


FIGURE 7: Voltage generation for different frequencies.

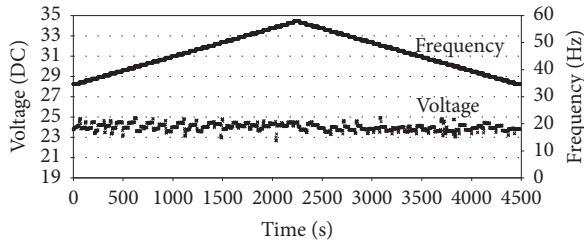


FIGURE 8: Voltage control for a constant ratio of frequency change.

This can be observed for the case when the angle is 100%. The voltage follows a similar path as per 75%; however at around 20 V the voltage decreases as the frequency increases. This can be explained because of the reduced capacity (displacement) of the hydraulic motor with respect to the pump. Because of its smaller size, the motor cannot admit 100% of the pump output; this creates an increase in the system pressure that in turn dampens the hydraulic pump, reducing the speed of the rotor. Hence, a hydraulic motor with a larger input capacity can produce a larger output voltage.

Due to the hardware constrains, it was decided to operate the system with a maximum output voltage of 48 V to avoid overheating of the input electric motor when the damping increases at the hydraulic pump. A second set of tests investigated the performance of the control at different output voltages. The frequency decreases on each case steadily by 1.5 Hz from 58 Hz down to the point where the rotor at the electric motor stops rotating due to damping. From Figure 7 it can be seen that there is a minimum voltage that any given frequency can generate, which follows the following equation.

$$V_{\min} = 1.5F - 4.5, \quad (13)$$

where V_{\min} represents the minimum DC voltage and F is the generator's frequency in Hz.

To evaluate the performance of the controller, the output voltage set-point was fixed to 24 V, while the input frequency was varied between 35 and 58 Hz every 60 s, as shown in Figure 8. In all the cases the electric load at the DC generator was the voltmeter with a 10 M Ω input impedance.

Figures 9 and 10 present a detailed view of the test when the input frequency was increased and decreased, respectively. Right after the frequency changes, the output voltage increases its error relative to the set-point. Few seconds later, the system adjusts the flow to reduce this error to a maximum of ± 0.5 V error band.

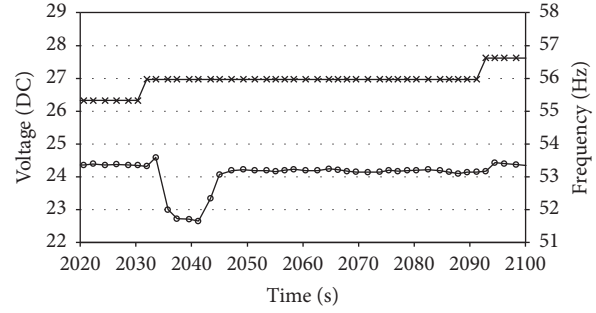


FIGURE 9: System adjustment as the frequency increases by 1.5 Hz.

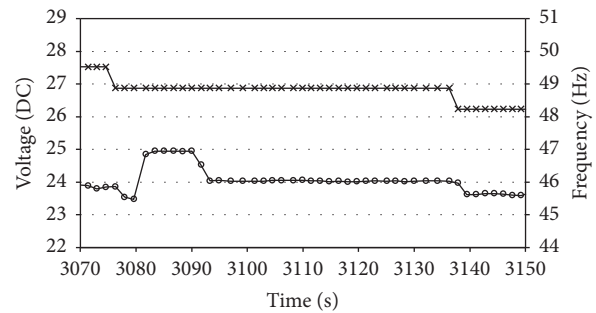


FIGURE 10: System adjustment as the frequency decreases by 1.5 Hz.

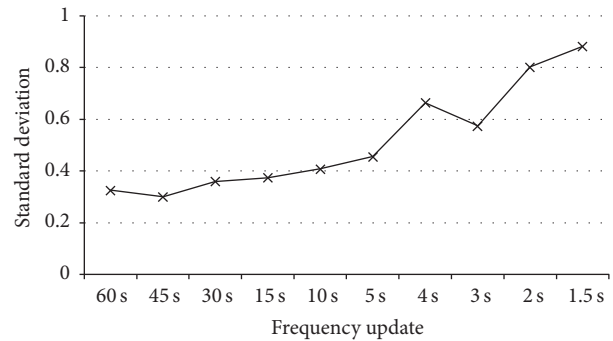


FIGURE 11: Standard deviation at various controller update rates.

The previous test was repeated reducing the time of the intervals between frequency changes, from 60 s to 1.5 s. Figure 11 shows the standard error deviation as the interval was reduced. The error increases as the time reduces; the system becomes less stable. At higher rates of change, the system cannot maintain the set voltage at the same pace as the frequency.

4.2. Computational Model of the System. A computational model of the hardware was built using Matlab Simulink. The system characterization presented in the previous section was used to model the hydraulic and electric systems present in the test bench. Figure 12 shows the full implementation

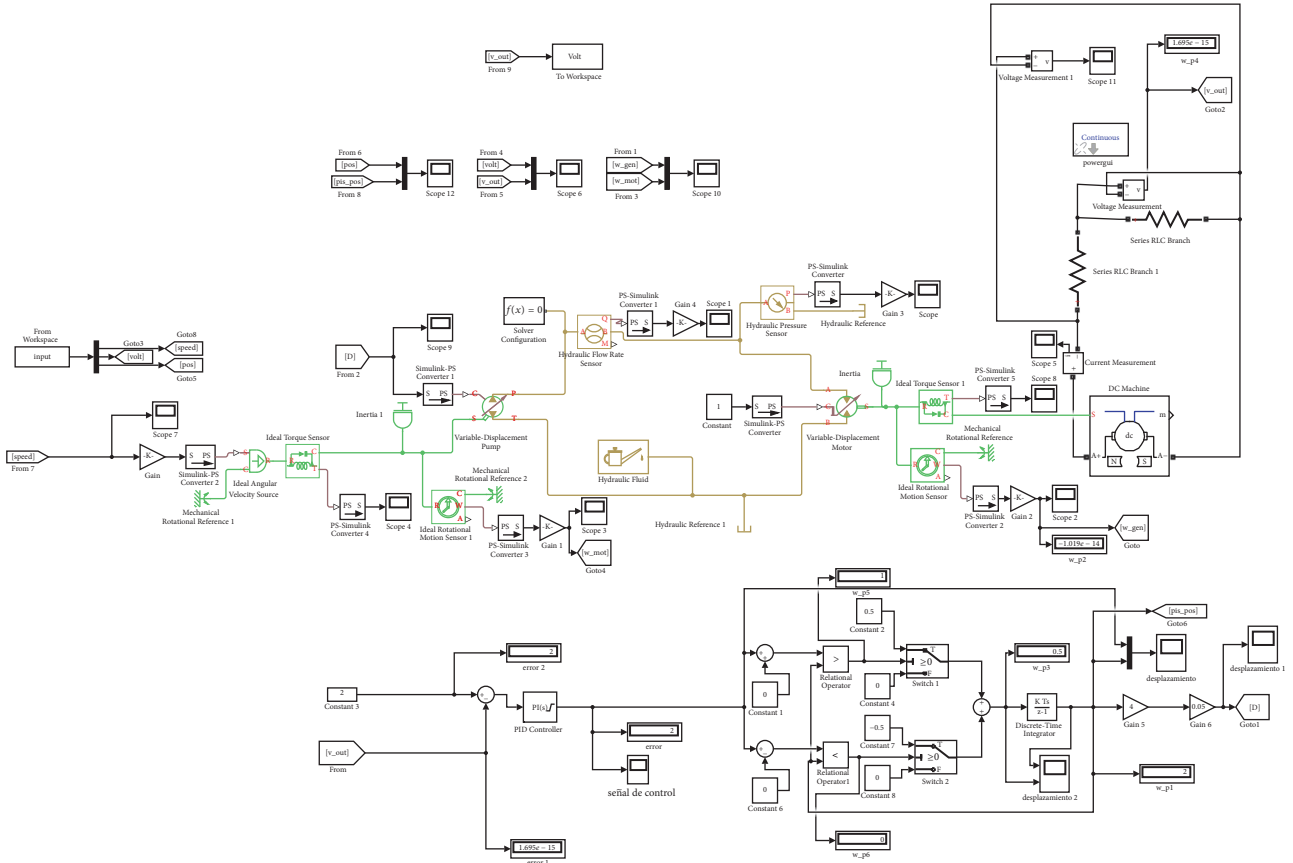


FIGURE 12: Computational model of the hydraulic wind power drive train.

TABLE 1: Model main parameters.

Parameter	Units	Value
Input shaft speed	RPM	Variable
Electric motor inertial mass	Kg·m ²	0.0008
Pump displacement	cm ³ /rev	18.02
Fluid viscosity	cSt	55.4
Fluid density	Kg/m ³	890
Bulk modulus	bar	14560
Hydraulic motor displacement	cm ³ /rev	0.29
Electric motor armature resistance	ohms	0.6
Torque constant	N·m/A	0.159

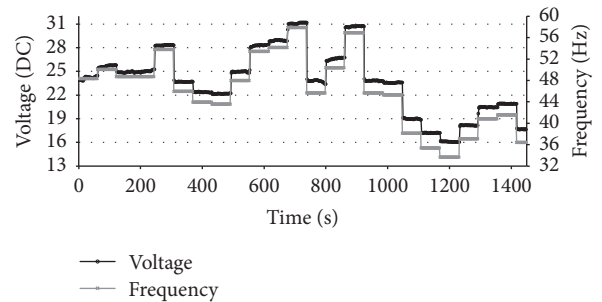


FIGURE 13: Voltage generation with control disabled.

of the model. The simulation included all of the hydraulic components, the DC electric generator, the controller, and the DC linear actuator. All of these models were validated using the experimental data and are summarized in Table 1.

5. Results and Discussion

A wind profile obtained from a real wind power turbine was used to evaluate the system. The data depicted in Figure 13 represents the wind measurements obtained over a period of 24 hours, one data point every hour. The data points were used in weighted estimates to span from 32 Hz to 58 Hz

to represent wind speeds between 0.4 and 17.2 m/s. These frequencies were used to drive the electric motor effectively simulating a variable wind speed.

An initial test evaluated the response of the system as the simulated wind was being changed. In this first test no control was enabled. The electric generator was connected to a 24 V gear motor to simulate a constant load. The gear motor was estimated to consume an approximate 6 W of power. The results of this test are shown on Figure 13. The variable hydraulic pump was adjusted at the beginning of the test to generate 24 V at 47 Hz. The voltage at the generator follows the same path as the driving frequency of the electric

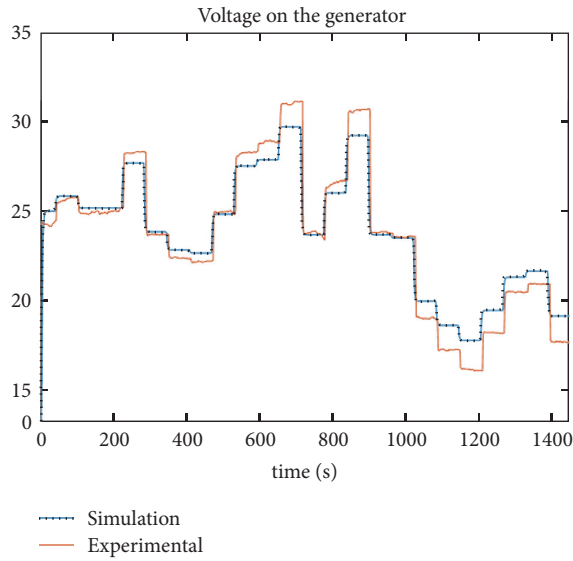


FIGURE 14: Voltage output for a varying wind speed input with control disabled.

motor, as expected. This case represents a fix gear ratio drive train, where the connection between the nacelle and the electric generator is fixed. This means the amount of power captured from the wind is reduced when the wind speed is lower than the nominal wind speed. However, if the wind speed is higher than the nominal value, the aerodynamic efficiency of the turbine is reduced to accommodate the optimal generator speed. At a certain high wind speed above the cut-off speed the nacelle is repositioned so that the turbine spins at a lower RPM. The generator output shown in Figure 13 demonstrates that undesirable variable voltage outputs are obtained at variable winds speeds; this system would be inefficient because the generated electric power would need to be rectified and regulated in order to be used by an electrical application.

The computational model was tested using the disabled controller. A comparison between the experimental data and the simulation is shown in Figure 14. The simulation followed the experimental results very closely with an accuracy as low as 12.5% at the worst case at 29 volts DC. The simulation was able to dynamically replicate the input signal without a significant time delay.

In the next experiment, the control was enabled and the test was performed under the same conditions described for the first experiment. It can be observed in Figure 15 that the system automatically adjusts itself to maintain a constant 24 V despite the input frequency. Overshoots can be observed when the frequency changes significantly; however, the voltage returns to the set-point within an average of 15 sec. These overshoots could be reduced if a hydraulic accumulator or another energy storage device was added to the system. A hydraulic accumulator is a device that captures hydraulic energy by storing pressurized fluid in a vessel; the pressurized vessel will increase its pressure as more fluid is pushed into the accumulator. Likewise the pressurized energy is released when the fluid is evacuated from the vessel. The

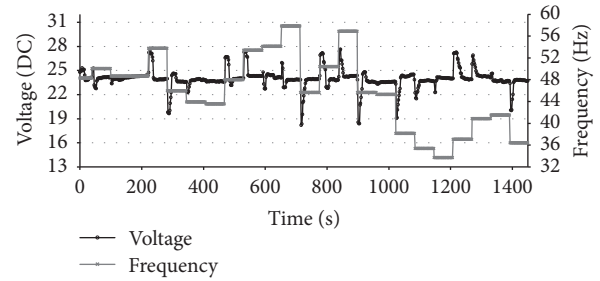


FIGURE 15: Hydraulic wind power drive train with enabled controller.

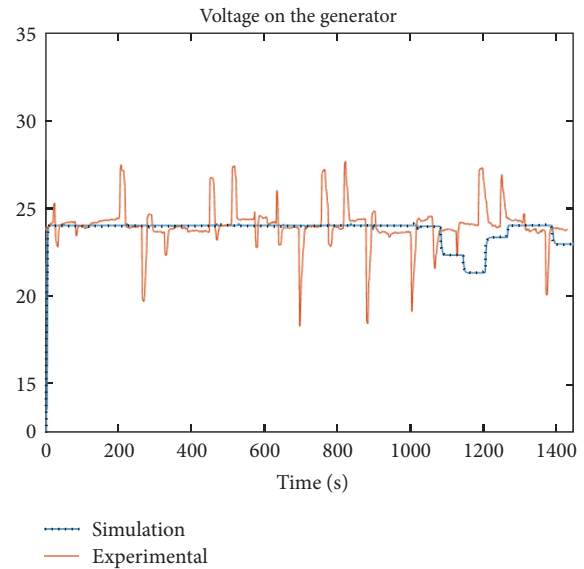


FIGURE 16: Voltage output for a varying wind speed input with control enabled.

accumulator contains a gas chamber that is allowed to change in volume such that when pressurized fluid rushes into the accumulator, the gas chamber is compressed, hence storing energy in the form of pressurized gas.

Results by Dutta et al. [17] show an estimated 4.1% percent increase in energy production on a 50 kW turbine by adding a 60 lt. accumulator. They also revealed how power generation can be regulated by absorbing voltage peaks and drops by adding such a hydraulic component.

The plot in Figure 16 shows a comparison of the simulated and the experimental behavior of the DC voltage generator when the controller is enabled. The simulation results show a lower magnitude of the overshoots when the frequency (wind speed) is changed, which means that the simulated system has not completely captured the dynamic effects of the physical system. There were instances where some drift from the desired voltage value was observed for the region of lower wind speeds recoded between 1100 s and 1200 s. This means the simulated controller was not able to adjust the angle of the swash plate in the pump to maintain a 24 VDC output at frequencies below 36 Hz. On the other hand, the experimental results also show that the experimental controller used was not able to effectively maintain the desired output at or

below this simulated speeds corresponding to approximately 14.96 m/s.

6. Conclusions

A system capable of simulating a small wind power turbine drive train fitted with an infinitely variable transmission was built and tested in laboratory conditions. This system was demonstrated to effectively maintain the electric power output constant despite the input conditions at the nacelle, that is, a hydromechanical solution to maintain the RPM of the electric generator constant regardless of the simulated wind speed. The simple control strategy used to maintain the output voltage of the DC generator proved to be an acceptable method to improve wind power turbine generation at speeds higher than 15 m/s for a small wind power generator (10–100 kW). New control strategies will be implemented in the test setup for an improved wind speed range and dynamic behavior. Lastly, the experimental results show that adding an energy storage device could be an effective and inexpensive method to absorb voltage overshoots created by wind gusts and sudden changes in wind direction.

Conflicts of Interest

The authors declare that they have no conflicts of interest.

References

- [1] P. J. Tavner, J. Xiang, and F. Spinato, "Reliability analysis for wind turbines," *Wind Energy*, vol. 10, no. 1, pp. 1–18, 2007.
- [2] F. Spinato, P. J. Tavner, G. J. W. Van Bussel, and E. Koutoulakos, "Reliability of wind turbine subassemblies," *IET Renewable Power Generation*, vol. 3, no. 4, pp. 387–401, 2009.
- [3] J. Carroll, A. McDonald, and D. McMillan, "Failure rate, repair time and unscheduled O&M cost analysis of offshore wind turbines," *Wind Energy*, vol. 19, no. 6, pp. 1107–1119, 2016.
- [4] J. Ribrant and L. Bertling, "Survey of failures in wind power systems with focus on Swedish wind power plants during 1997–2005," in *Proceedings of the 2007 IEEE Power Engineering Society General Meeting, PES*, usa, June 2007.
- [5] A. Froger, M. Gendreau, J. E. Mendoza, E. Pinson, and L.-M. Rousseau, "Solving a wind turbine maintenance scheduling problem," *Journal of Scheduling*, pp. 1–24, 2017.
- [6] Y. Su, J. D. Kern, and G. W. Characklis, "The impact of wind power growth and hydrological uncertainty on financial losses from oversupply events in hydropower-dominated systems," *Applied Energy*, vol. 194, pp. 172–183, 2017.
- [7] F. Ben Amar, M. Elamouri, and R. Dhifaoui, "Energy assessment of the first wind farm section of Sidi Daoud, Tunisia," *Renewable Energy*, vol. 33, no. 10, pp. 2311–2321, 2008.
- [8] E. Muljadi and C. Butterfield, "Pitch-controlled variable-speed wind turbine generation," *IEEE Transactions on Industry Applications*, vol. 37, no. 1, Article ID 903156, pp. 240–246, 2001.
- [9] B. Thul, R. Dutta, and K. Stelson, "Hydrostatic transmission for mid-size wind turbines," *Wind Energy Plants*, pp. 1017–1022, 2011.
- [10] M. Deldar, A. Izadian, and S. Anwar, "Reconfiguration of a wind turbine with hydrostatic drivetrain to improve annual energy production," in *Proceedings of the 7th Annual IEEE Energy Conversion Congress and Exposition, ECCE 2015*, pp. 6660–6666, can, September 2015.
- [11] J. Schmitz, N. Vatheuer, O. Reinertz, and H. Murrenhoff, "Hydrostatic drive train in wind energy plants," in *Proceedings of International Fluid Power Conference and Exposition*, pp. 1017–1022, Las Vegas, 2011.
- [12] Z. Yang, M. Krishnamurthy, and J. M. Garcia, "Modeling and control of a continuously variable planetary transmission for a small wind turbine drivetrain," in *Proceedings of the ASME 2013 Conference on Smart Materials, Adaptive Structures and Intelligent Systems*, pp. 10–1115, Snowbird, UTAH, 2013.
- [13] X. Zhao and P. Maißer, "A novel power splitting drive train for variable speed wind power generators," *Renewable Energy*, vol. 28, no. 13, 2003.
- [14] S. Hamzehlouia, A. Izadian, A. Pusha, and S. Anwar, "Controls of hydraulic wind power transfer," in *Proceedings of the 37th Annual Conference of the IEEE Industrial Electronics Society, IECON 2011*, pp. 2475–2480, aus, November 2011.
- [15] A. Pusha, M. Deldar, and A. Izadian, "Efficiency analysis of hydraulic wind power transfer system," in *Proceedings of the 2013 IEEE International Conference on Electro/Information Technology, EIT 2013*, usa, May 2013.
- [16] Danish Wind Industry Association, "Wind Power Generators," Wind Turbine Generators, 2017.
- [17] R. Dutta, F. Wang, B. F. Bohlmann, and K. A. Stelson, "Analysis of short-term energy storage for midsize hydrostatic wind turbine," *Journal of Dynamic Systems, Measurement and Control, Transactions of the ASME*, vol. 136, no. 1, Article ID 011007, 2014.

Research Article

A Comparison of Off-Grid-Pumped Hydro Storage and Grid-Tied Options for an IRSOFC-HAWT Power Generator

Mahdi Majidniya,¹ Kobra Gharali,¹ and Kaamran Raahemifar²

¹Department of Mechanical Engineering, University of Tehran, Tehran, Iran

²Department of Electrical & Computer Engineering, Ryerson University, Toronto, ON, Canada

Correspondence should be addressed to Kobra Gharali; kgharali@ut.ac.ir

Received 7 April 2017; Revised 12 May 2017; Accepted 4 June 2017; Published 10 July 2017

Academic Editor: Yuanzheng Li

Copyright © 2017 Mahdi Majidniya et al. This is an open access article distributed under the Creative Commons Attribution License, which permits unrestricted use, distribution, and reproduction in any medium, provided the original work is properly cited.

An Internal Reforming Solid Oxide Fuel Cell (IRSOFC) is modeled thermodynamically; a Horizontal Axis Wind Turbine (HAWT) is designed; the combined IRSOFC-HAWT system should create a reliable source of electricity for the demand of a village located in Manjil, Iran. The output power of HAWT is unstable, but by controlling the fuel rate for the IRSOFC it is possible to have a stable power output from the combined system. When the electricity demand is over the peak or the wind speed is low/unstable/significantly high, the generated power may not be sufficient. To solve this problem, two scenarios are considered: connecting to the grid or using a Pumped Hydro Storage (PHS). For the second scenario, the extra produced electricity is saved when the production is more than demand and can be used when the extra power is needed. The economic analysis is done based on the economic conditions in Iran. The results will show a period of return about 9.5 and 13 years with the levelized cost of electricity about 0.0747 and 0.0882 \$/kWh for the first and second scenarios, respectively. Furthermore, effects of some parameters such as the electricity price and the real interest rate are discussed.

1. Introduction

Making a balance between energy productions and energy demands is a challenging issue for Renewable Energy (RE) systems. Energy production from RE sources is affected by low efficiencies, high capital costs, unreliable energy sources, and environmental impacts. Recently, combined systems are introduced to create efficient and economical power sources and mostly to overcome the unreliability of RE systems such as wind turbines. Based on the local conditions and the main energy source, the way that systems are combined varies. One of the options is combining the systems with a fuel cell. A fuel cell is a Renewable Energy source with controllable output electricity. A fuel cell has a short startup time. It is possible to add or remove cells immediately from the power cycle without any trouble. An SOFC is a common type of fuel cells for power plant applications. Recent studies include an SOFC in the power generation systems. In the following, some of the recent combinations of SOFC with other systems are discussed.

Soheyli et al. [1] analyzed a combined system in a hypothetical hotel in Kermanshah, Iran. The final optimized system was a combination of 10 wind turbines, 430 PV modules, 11 SOFCs, 106 batteries, and 2 heat storage tanks. Their results showed that the fuel consumption and pollution were decreased 263 and 353 times, respectively. Fathy [2] studied a system including photovoltaic modules, wind turbines, and fuel cells in Egypt. Obara et al. [3] used a numerical analysis to stabilize photovoltaic cyclic fluctuations by using a governor-free control of an SOFC and a flywheel inertia system. Hosseini et al. [4] analyzed a combination of photovoltaic-electrolyzer, SOFC, and a heat recovery unit for a residential area. The system supported an absorption chiller and a heat recovery steam generator using the excess heat of an SOFC. They conducted an energy and exergy analysis of the system. Vigneysh and Kumarappan [5] studied a combination of photovoltaic cells, an SOFC, and a battery energy storage system. For making a balance between power generation and consumption, a fuzzy logic method was applied. The SOFC was a backup generator. It reached its

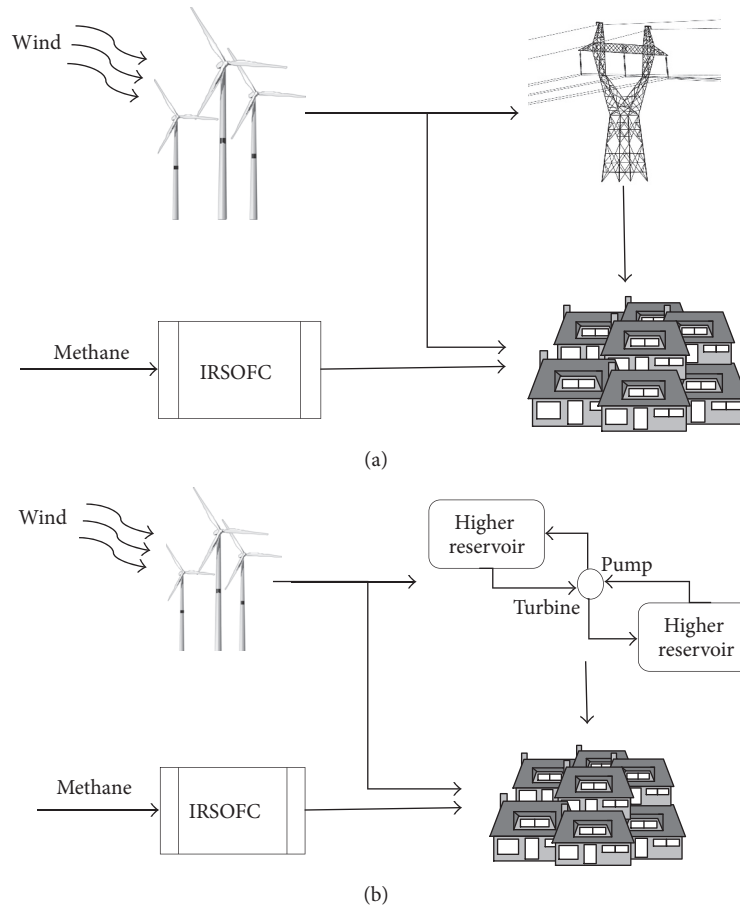


FIGURE 1: Schematic of the system: (a) first scenario and (b) second scenario.

rated power when the charge of the battery energy storage system was at the minimum limit. Tenfen and Finardi [6] presented a mathematical model to manage the energy from a microgrid. They modeled a micro turbine and an SOFC and combined them with a battery bank, photovoltaic cells, and a wind turbine. Akikur et al. [7] developed a mathematical model for a reversible SOFC combined with photovoltaic cells. To produce 100 kW of electricity, they investigated thermodynamically and economically three modes: a solar-SOFC mode for low solar radiation, a solar-solid oxide steam electrolyzer mode for high solar radiation, and an SOFC mode at night. Bai et al. [8] modeled and controlled an SOFC with photovoltaic cells. They used two PI controllers using an artificial bee colony.

It was shown that the combination of an SOFC with a wind turbine or photovoltaic cells is a state-of-the-art topic. In this study, a PHS is also added to a combined system of a HAWT and an IRSOFC. The system can run on grid or off grid with the aid of PHS as an energy storage component. The results are compared based on the economic and thermodynamic analysis to study the feasibility of each scenario; this comparison has not been done before based on the knowledge of the authors. In addition, the systems should fulfill the power demand of a village located in Manjil,

Iran. The parameters are chosen based on the local economic and environmental conditions, making this study unique. It should be noticed that the system is sized based on monthly average wind speed and the needed electricity. That means the wind speed may not always match the needed electricity. For solving this problem, the two following scenarios are introduced.

The First Scenario (Figure 1(a)). The system is connected to the grid. It is possible to sell and buy electricity from the grid. The electricity can be sold to the grid when the produced electricity is more than demand. The electricity can be bought from the grid when the production cannot meet the demand. It is assumed that the prices of the selling and buying electricity are the same.

The Second Scenario (Figure 1(b)). The system is not connected to the grid. The extra electricity production of the wind turbine is saved by a Pumped Hydro Storage (PHS) system and can be released when it is needed. A PHS is a system that contains a pump, a turbine, and two reservoirs, a higher reservoir and a lower one. During high electricity production, the PHS pumps the water from the lower reservoir to

the higher one to save the energy. When the electricity is needed, the water goes from the higher reservoir to the lower one through a turbine. Because of the pump and the turbine efficiencies and the other losses, some of the energy will be lost during these processes. To make up this energy, the size of the HAWT has been increased. The size of the PHS is assumed to be equal to the maximum needed electricity minus maximum production of the IRSOFC.

The case study is to produce power for a village with 100 houses located in Manjil, Iran. An economic analysis will show the possibility of the study.

Based on two scenarios, the main components, the IRSOFC and the HAWT, are modeled and designed in Sections 2 and 3. The economic method is described in Section 4. After validating the IRSOFC and the HAWT in Section 5, the results of the modeling and the economic analysis are discussed in Section 6.

2. Thermodynamic Modeling of IRSOFC

The modeling of components is done by home codes. The assumptions of the fuel cell modeling are

- (i) ideal gases,
- (ii) linear variation of enthalpy,
- (iii) working in a steady condition,
- (iv) being isolated with no heat exchange,
- (v) no contact resistance,
- (vi) ignoring radiation heat transfer between the gas canal and the solid container,
- (vii) tubular cells and stack.

2.1. Direct Internal Reformer. For a fuel cell consuming natural gas, an internal or an external reformer is needed. Since an external reformer needs a cooling system and is less cost-effective than an internal one, the internal reformers are preferred [9].

In the internal reforming process, the occurring reactions are very endothermic, while the heat is provided by the fuel cell. The reactions in this process are the steam reforming reaction ($x \Rightarrow \text{CH}_4 + \text{H}_2\text{O} \rightarrow \text{CO} + 3\text{H}_2$) and the gas water shifting reaction ($y \Rightarrow \text{CO} + \text{H}_2\text{O} \rightarrow \text{CO}_2 + \text{H}_2$). According to these reactions, natural gas transforms to hydrogen in the fuel cell. Hydrogen takes part in an electrochemical reaction ($z \Rightarrow \text{H}_2 + (1/2)\text{O}_2 \rightarrow \text{H}_2\text{O}$). Here, x , y , and z are the molar rate progress of reforming, shifting, and electrochemical reactions, respectively [10]. This molar rate progress is calculated based on the relation among the equation constants, the temperature, and the pressure of the gasses.

TABLE 1: IRSOFC resistivity constants [12].

	A ($\Omega\cdot\text{cm}$)	B (K)	δ (cm)
Anode	0.00298	1392	0.01
Cathode	0.00811	-600	0.19
Electrolyte	0.0294	-10350	0.004
Internal connections	0.1256	-4690	0.0085

2.2. Reversible Voltage. The reversible voltage (E_{rev}) of the cell can be found by using Nernst equation:

$$\begin{aligned} E_{\text{rev}} &= E^\circ + \Delta E = \frac{-\Delta G^\circ}{n_e F} + \frac{-\Delta G}{n_e F} \\ &= \frac{-\Delta G^\circ}{2F} + \frac{RT}{2F} \ln \frac{p_{\text{H}_2} p_{\text{O}_2}^{0.5}}{p_{\text{H}_2\text{O}}}. \end{aligned} \quad (1)$$

Because of the irreversibilities, the voltage of a real fuel cell is less than that of a reversible one. These irreversibilities are called overpotentials. Overpotentials can be divided into three categories: Ohmic (η_{Ohm}), activation (η_{Act}), and concentration (η_{Conc}). The magnitude of these overpotentials grows as current density increases, which results in reducing the voltage of the cell. The cell voltage can be described as ([11])

$$E = E_{\text{rev}} - (\eta_{\text{Act}} + \eta_{\text{Ohm}} + \eta_{\text{Conc}}). \quad (2)$$

2.2.1. Ohmic Overpotential. Ohmic overpotential (η_{Ohm}) can be calculated as

$$\eta_{\text{Ohm}} = ir, \quad (3)$$

where r is the resistance:

$$r = \delta\rho. \quad (4)$$

δ is the thickness (Table 1) of components and ρ is the resistivity:

$$\rho = A \exp\left(\frac{B}{T}\right). \quad (5)$$

A and B are resistivity constants (Table 1).

2.2.2. Activation Overpotential. Butler–Volmer equation [13] describes

$$i = i_0 \left\{ \exp\left(\beta \frac{n_e F \eta_{\text{Act}}}{RT}\right) - \exp\left(- (1 - \beta) \frac{n_e F \eta_{\text{Act}}}{RT}\right) \right\}. \quad (6)$$

β is the heat transfer coefficient and i_0 is the exchange current density. The heat transfer coefficient is the ratio of the exchange in the potential drop which results in changing the rate of constants. The value of β for a fuel cell is 0.5. For $\beta = 0.5$, (6) can be

$$i = 2i_0 \sinh\left(\frac{n_e F \eta_{\text{Act}}}{2RT}\right). \quad (7)$$

TABLE 2: Values of activation overpotential constants [11].

		Cathode	Anode
γ	A/m ²	1.49×10^{10}	2.13×10^8
E_{Act}	kJ/mol	110	160

Therefore,

$$\eta_{Act,An} = \frac{2RT}{n_e F} \sinh^{-1} \left(\frac{i}{2i_{0,An}} \right), \quad (8)$$

$$\eta_{Act,Ca} = \frac{2RT}{n_e F} \sinh^{-1} \left(\frac{i}{2i_{0,Ca}} \right).$$

Equation (7) should be applied to both anode and cathode [13].

$$i_{0,An} = \gamma_{An} \left(\frac{p_{H_2}}{p_{ref}} \right) \left(\frac{p_{H_2O}}{p_{ref}} \right) \exp \left(-\frac{E_{Act,An}}{RT} \right), \quad (9)$$

$$i_{0,Ca} = \gamma_{Ca} \left(\frac{p_{O_2}}{p_{ref}} \right)^{0.25} \exp \left(-\frac{E_{Act,Ca}}{RT} \right)$$

γ (preexponential factor) like the activation energy (E_{Act}) depends on electrode materials [11] (Table 2).

2.2.3. Concentration Overpotential. Concentration overpotential can be calculated as

$$\eta_{Conc} = \frac{RT}{n_e F} \left(1 - \frac{i}{i_l} \right), \quad (10)$$

where i_l is the limiting current density. Considerable growth of concentration overpotential will be observed if the current density meets its limit.

3. HAWT Modeling

A home code for designing a HAWT is written based on Blade Element Momentum (BEM) method. For a rotor of a HAWT with the radius (R), the blade should be divided into some sections or elements. Each section (i) has a distance r from the hub of the rotor.

For each element, the local chord of the blade ($c(r)$) can be calculated from Schmitz formulation [14]:

$$c(r) = \frac{8\pi r}{NC_L} \left(1 - \cos \left(\frac{2}{3} \tan^{-1} \left(\frac{R}{r\lambda_r} \right) \right) \right). \quad (11)$$

λ_r is the local tip speed ratio, N is the number of blades, and C_L is the lift coefficient. The power coefficient (C_p) of the turbine is determined from the following equation [15]:

$$C_p = \frac{8}{\lambda_R N} \sum_{i=k}^N F_i \sin^2 \varphi_i (\cos \varphi_i - \lambda_{ri} \sin \varphi_i) \cdot (\sin \varphi_i + \lambda_{ri} \cos \varphi_i) \left[1 - \frac{C_D}{C_L} \cos \varphi_i \right] \lambda_{ri}^2, \quad (12)$$

where F is Prandtl's correction factor, φ is the angle between the resultant velocity and the rotor plane, and C_D is the drag coefficient.

3.1. Corrections. In (12), F is Prandtl's correction factor. This factor is calculated as [16]

$$F = \frac{2}{\pi} \cos^{-1} (e^{-f}), \quad (13)$$

$$f = \frac{N}{2} \frac{R-r}{r \sin \varphi} = \frac{N}{2} \frac{1-r/R}{(r/R) \sin \varphi}.$$

Another correction applied to the modeling is based on the Reynolds number. For the variable range of the Reynolds number, Hernandez and Crespo [17] suggested a correction in which the lift coefficient remains unchanged and the drag coefficient is corrected:

$$C_D = C_{D,ref} \left(\frac{Re_{ref}}{Re} \right)^{0.2}. \quad (14)$$

Re_{ref} is the Reynolds number in which the drag coefficient ($C_{D,ref}$) of the blade is computed and Re is the Reynolds number based on the working conditions.

Glauert correction is also applied in this modeling to calculate the induced velocities.

4. Economic Modeling

Economic analysis is developed based on the Annualized Cost of System (ACS). In this method, revenues and costs are converted to a uniform annuity payment. ACS is the combination of annualized capital cost (C_{acap}), annualized replacement cost (C_{arep}), annualized maintenance cost (C_{amain}), and annualized operating cost (C_{aope}) [18].

ACS

$$= C_{acap} (\text{total instrument}) + C_{arep} (\text{total instrument}) + C_{amain} (\text{total instrument}) + C_{aope} (\text{labor cost} + \text{fuel cost} + \text{insurance cost}). \quad (15)$$

Annualized capital cost of the system is

$$C_{acap} = C_{cap} \cdot CRF(i, Y_{proj}), \quad (16)$$

$$CRF(i, Y_{proj}) = \frac{i(1+i)^{Y_{proj}}}{(1+i)^{Y_{proj}} - 1}.$$

C_{cap} is the capital cost of each component in terms of US dollar and Y_{proj} is the lifetime of each component in terms of years. The rate of payback (CRF) calculates the present value of the annual cost (a set of annual homogeneous cash flows). The annual real interest rate (i) is

$$i = \frac{j-f}{1+f}. \quad (17)$$

In (17), f is annual inflation rate and j is the nominal interest rate. For an initial cost of equipment, see Table 3.

TABLE 3: Initial capital costs of instruments ([18–20]).

Component	Cost
Compressor	$C_{\text{comp}} = 91562 \left(\frac{\dot{W}_{\text{comp}}}{445} \right)^{0.67}$
Heat exchanger	$C_{\text{HX}} = 8500 + 409 (A_{\text{HX}})^{0.85}$
IRSOFC	$C_{\text{SOFC}} = (n_{\text{cells}} \pi D_{\text{cell}} L_{\text{cell}}) (2.96 T_{\text{cell}} - 1907)$
IRSOFC auxiliary component	$C_{\text{aux,SOFC}} = 0.1 C_{\text{SOFC}}$
Inverter	$C_{\text{inv}} = 10^5 \left(\frac{\dot{W}_{\text{cell}}}{500} \right)^{0.7}$
GT	$C_{\text{GT}} = \dot{W}_{\text{GT}} (-98.328 \ln(\dot{W}_{\text{GT}}) + 1318.5)$
Combustion chamber	$C_{\text{cc}} = (1 + \exp(0.018 T_{\text{GT}} - 26.4)) \times \left(\frac{46.08 \dot{m}_{\text{cc}}}{0.995 - P_{\text{GT}}/P_{\text{cc}}} \right)$
HAWT	1300 (\$/kW)
PHS	2000 (\$/kW)

The annual replacement cost for this project is considered to be zero; that means the lifetime of the components is equal to the lifetime of the project. For each element, 5% of the initial cost is considered for the cost of the maintenance [18].

The annual costs of labor, fuel, and insurance are considered as the annual operating costs [18].

4.1. Net Present Value (NPV). The NPV in the engineering economics is one of the standard methods to evaluate the economic plans:

$$\text{NPV} = \frac{\text{ACS}}{\text{CRF}(i, Y_{\text{proj}})}. \quad (18)$$

NPV is the present value of installing and operating the system over its lifetime in a project. The higher the amount of NPV is, the more profitable the project is. If NPV is negative, the project will lose money and it is infeasible in terms of economics [18].

4.2. Levelized Cost of Product (LCOP). The LCOP is the average cost of total usable power production capacity of the system [18]:

$$\text{LCOP} = \frac{\text{ACS}}{\text{SOPC}}. \quad (19)$$

The SOPC is Summation of Product Costs in a year.

4.3. Other Economic Parameters. Since the LCOP is based on total cost in the lifetime of the project, the Prime Cost (PC) is used based on the market price [18]:

$$\text{PC} = \frac{\text{OFC}}{\text{VOP}}. \quad (20)$$

The OFC or Operating Flow Costs include operating cost, fuel cost, labor cost, and the insurance cost for a year. The VOP is the Volume of Product in a year.

The period of return (POR) is the ratio of the capital costs to the Net Annual Benefit (NAB). Projects with a shorter

POR are more attractive for the investment compared to plans which have longer periods. The POR means the total time to earn the entire initial capital by the profit [18]:

$$\text{POR} = \frac{C_{\text{Cap}}}{\text{NAB}}. \quad (21)$$

C_{Cap} is the capital cost. The NAB is the subtraction of income taxes from Annual Benefit (AB). AB can be calculated as [18]

$$\text{AB} = \text{SOPC} - \text{OFC}. \quad (22)$$

5. Validation

5.1. IRSOFC. The modeled fuel cell is validated with a model proposed by Pirkandi et al. [10] (Figures 2(a)–2(d)). The fuel cell was run based on Pirkandi et al.'s [10] condition which was a tubular fuel cell at 1273 K and 100 kPa with 0.85 of fuel utilization factor and 9000 A/m² of limiting current density. The fuel composition was 97% methane, 1.5% carbon dioxide, and 1.5% nitrogen. The air composition was 21% oxygen and 79% nitrogen. In Figure 2, the variation of total voltage and overpotentials are compared with the results of Pirkandi et al. [10]. Since the compared curves are close, the current model is valid and reliable. Increasing the current density (i) enriches the overpotential values (Figures 2(a)–2(c)), resulting in decreasing the cell voltage (Figure 2(d)).

5.2. HAWT. The home code is validated by the experimental work of Khalfallah and Koliub [21] for a three-bladed HAWT. The current home code was run for the referred conditions. The output powers from the home code were compared with the results of Khalfallah and Koliub [21] from cut-in wind speed to the designed wind speed, where the maximum power is accessible. As it is shown in Figure 3, the overall agreement between two curves is visible.

6. Results and Discussion

The required power for the targeted village is 320 kW, but, in this study, the generated power of 347 kW is considered.

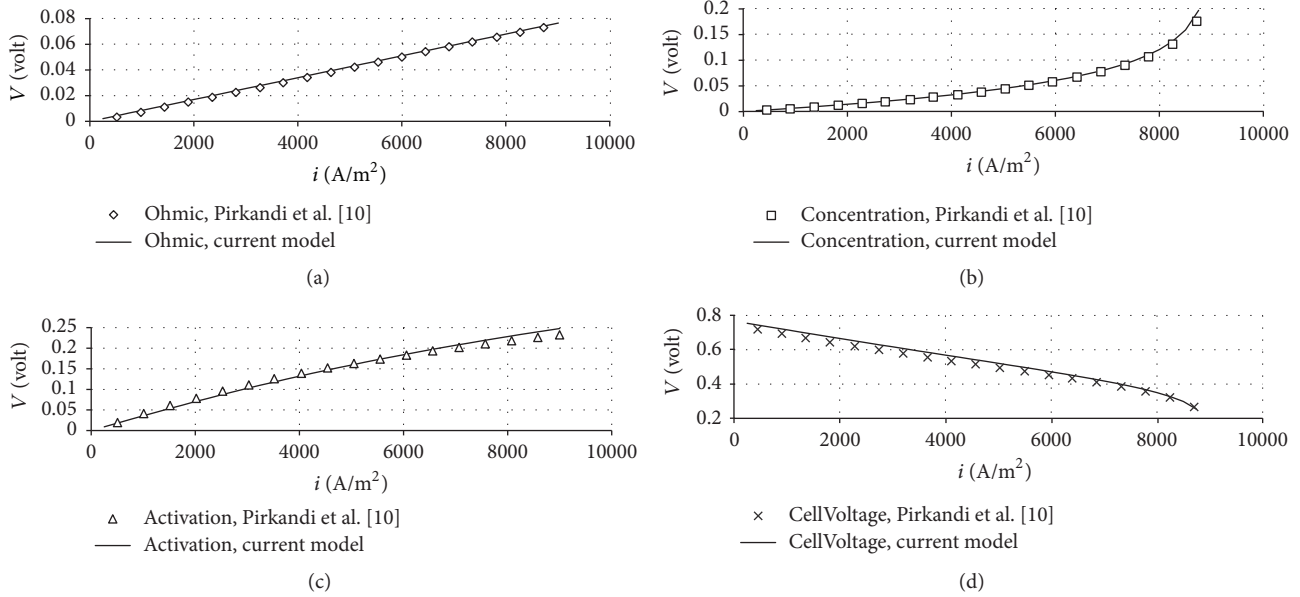


FIGURE 2: IRSOFC validation: (a) ohmic overpotential, (b) concentration overpotential, (c) activation overpotential, and (d) cell voltage.

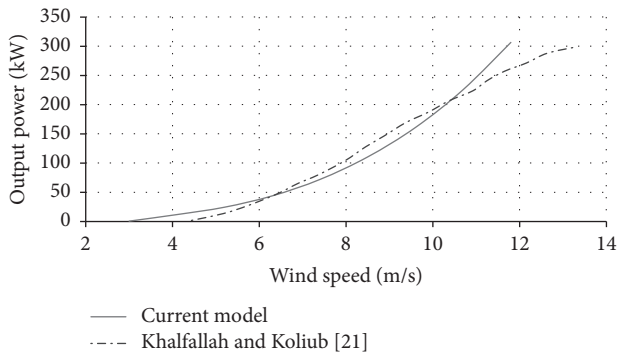


FIGURE 3: Validation of HAWT.

Then, based on 347 kW power which is assumed to be the targeted power demand, an IRSOFC and a HAWT are modeled.

6.1. Designed HAWT. Based on 10-year NASA records [22], the monthly averaged wind speeds at 50 meters above the surface of the earth for Manjil, north of Iran, were extracted. According to these data, a stall regulated wind turbine with nominal wind speed at 7.9 m/s is chosen. For the selection of airfoils, the blade is divided into three parts. An airfoil from the S-serious NREL families is selected for each part.

The details of the design of the wind turbine for two scenarios are provided in Table 4. As it was mentioned in the second scenario (off-grid IRSOFC-HAWT-PHS) the size of HAWT will increase because of the PHS efficiency and energy loss. The rated power of the HAWT for the first scenario is 347 kW. For the second scenario, the rated power is increased about 30%.

The chosen airfoil profiles were shown in Figure 4. The S818 airfoil, a thin airfoil, is used at the tip to absorb the

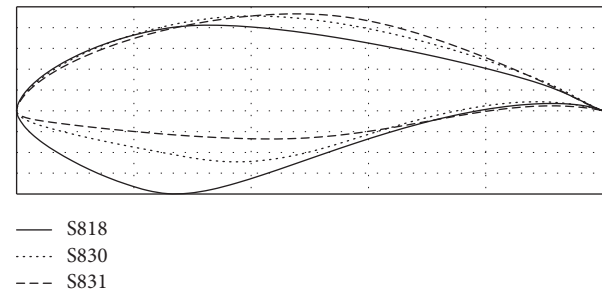


FIGURE 4: Selected airfoils.

TABLE 4: Details of the modeled HAWT.

	First scenario	Second scenario
Tip speed ratio	6	6
Number of blades	3	3
Rotor diameter (m)	58.14	66.14
Blade radius (m)	26.67	30.34
Hub height (m)	50	50
Airfoils	S818, S830, S831	S818, S830, S831

maximum power. From the tip to the root, the airfoils become thicker. S830 and S831 are the airfoils used for the mid and the root of the blade, respectively. The variations of blade pitch (φ) and the chord during the blade are shown in Figure 5. The behaviors of both scenarios are almost the same.

After designing the HAWT and based on the wind speed variations, monthly power generation from the HAWT for both scenarios is shown in Figure 6. Because of the low wind speed from September to February, the power production of the HAWT has the lowest values in these months. In July and August, the power reaches its maximum values as the wind is so strong.

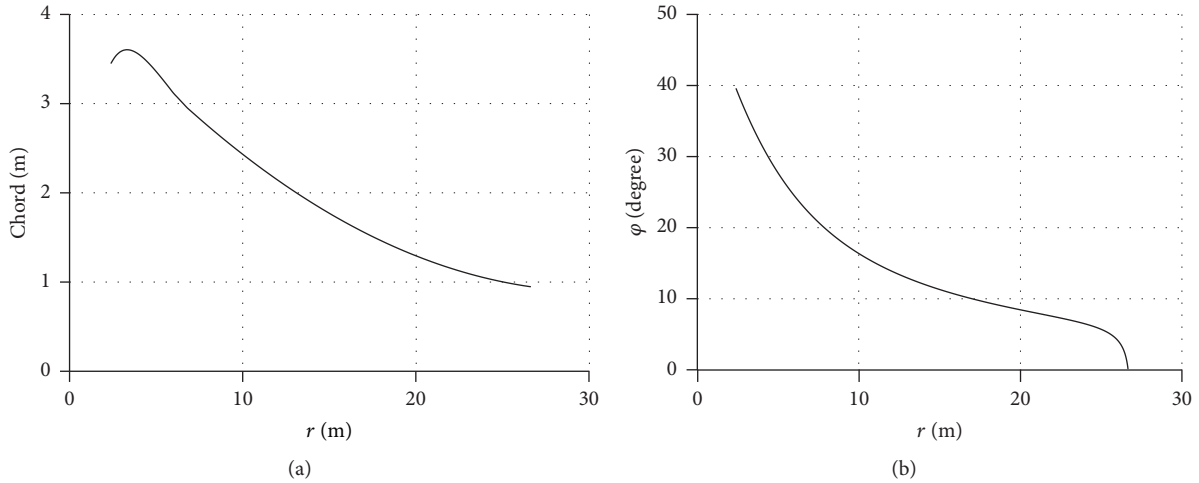


FIGURE 5: Variation of (a) chord and (b) φ during the blade.

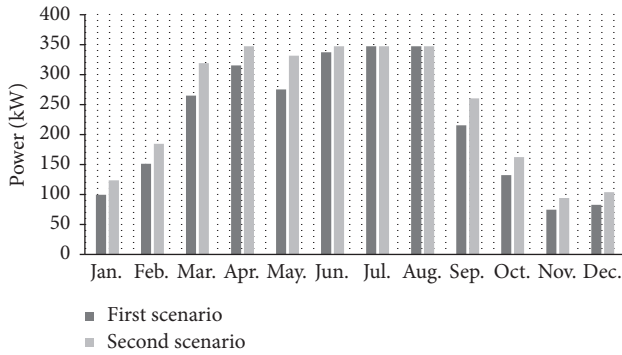


FIGURE 6: Monthly power generation from the HAWT.

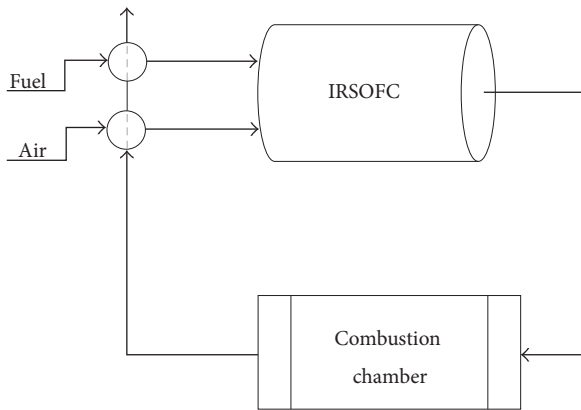


FIGURE 7: A schematic of the IRSOFC cycle.

6.2. *IRSOFC Model.* IRSOFC works at 1 bar pressure. The fuel that is fed to the IRSOFC is methane. A schematic of it is shown in Figure 7. The details of the IRSOFC inputs are provided in Table 5.

According to the power generated by the wind turbine during a year (Figure 6), the rest of the needed power should

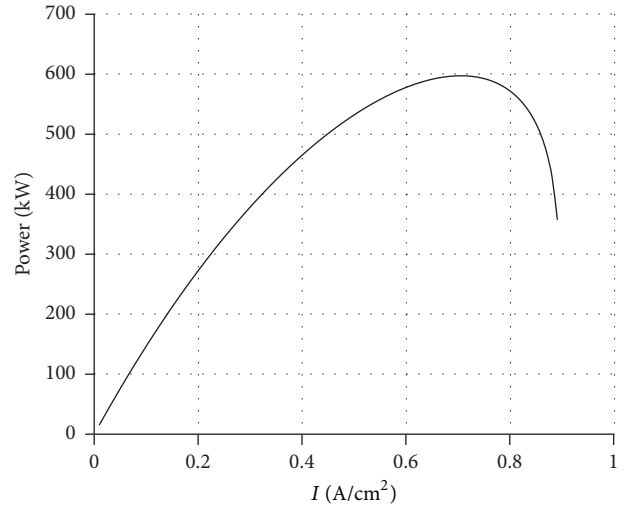


FIGURE 8: Variation of IRSOFC power production versus current density (first scenario).

be generated by the IRSOFC. The results of IRSOFC modeling for both scenarios are shown in Table 6. The fuel flow rate in Table 6 is based on a full load operation. The IRSOFC does not work under full load all the time but using full load fuel flow rate for the whole year in economic analysis will provide a safety margin that the village will always have stable electricity.

In the second scenario, the size of the PHS equals 94 kW, which is the difference between the power demand and the IRSOFC capacity. Power and efficiency variation versus current density for the first scenario are shown in Figures 8 and 9, respectively. There is no significant difference between the results of two scenarios. As it is shown, increasing current density (up to 0.65 A/cm^2) increases the power but decreases the efficiency of the system because the fuel consumption strongly depends on the current density. Thus, the current density of IRSOFC is set to 2000 A/m^2 .

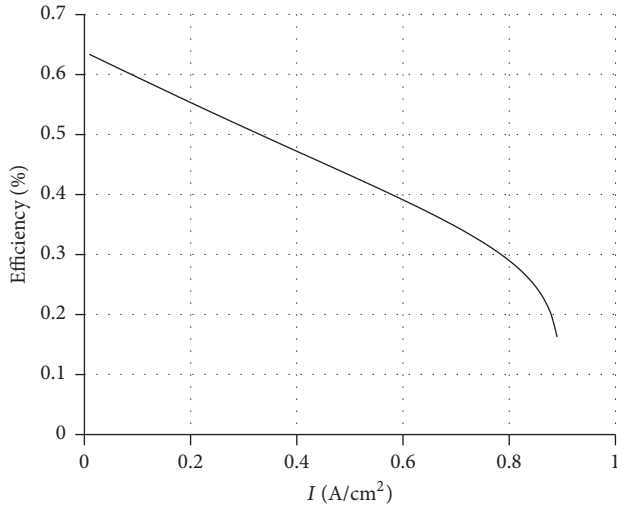


FIGURE 9: Variation of IRSOFC efficiency versus current density (first scenario).

TABLE 5: Input parameters for IRSOFC system.

Component efficiency		
Combustion chamber	95	%
Heat exchanger	80	%
Inverter	96.5	%
Pressure drop		
Heat exchanger	1	%
SOFC	2	%
Combustion chamber	1	%
SOFC input data		
Area	0.0834	m ²
Recirculation ratio	60	%
Limiting current density	9000	A/m ²
Current density	2000	A/m ²
Fuel utilization factor	85	%
Air utilization factor	25	%

TABLE 6: Results of IRSOFC modeling.

		First scenario	Second scenario
Electrical efficiency	%	55.3	55.3
Number of cells		2554	2371
SOFC power production	kW	272.5	253.0
Fuel flow rate	kg/s	0.0099	0.0091

6.3. Economic Study. It is assumed that government is going to run this project. The goal is to compare the current results with those from the conventional methods to produce electricity. Therefore, the electricity price and the fuel price are considered based on the prices for the government. For inputs and conditions, see Table 7.

Because of the size of the systems, grid connection cost (first scenario), and the PHS cost (second scenario), the economic results from two scenarios are different. The wind farm price is divided into 69% for the turbine, 12% for the

TABLE 7: Economic parameter.

Number of labors	3	
Labor's salary	500	\$/month
Project lifetime	20	Year
Price of products	0.0879	\$/kWh
Interest rate	22	%
Annual inflation rate	15.6	%
Tax	8	%
Fuel price	0.23	\$/m ³

TABLE 8: Economic results.

		First scenario	Second scenario
ACS	\$	2.2709×10^5	2.6833×10^5
C_{acap}	\$	1.0919×10^5	1.3206×10^5
C_{arep}	\$	0	0
C_{amain}	\$	6.5046×10^4	7.8674×10^4
C_{aope}	\$	5.2854×10^4	5.7591×10^4
LCOP	\$/kWh	0.0747	0.0882
NPV	\$	2.7056×10^6	3.1970×10^6
AB	\$	1.4941×10^5	1.3104×10^5
PC	\$/kWh	0.0388	0.0448
POR	Year	9.4645	13.0515

grid connection, 8% for the foundation, 3% for the internal grid, 3% for the installation, and 5% for the rest [23]. For the second scenario, the cost of grid connection is replaced by the PHS cost. The results of the economic analysis are shown in Table 8.

All economic parameters are dominated by the capital cost which is the highest in the second scenario. The POR and the PC for the second scenario are about 38% and 15% higher than those of the first one, respectively. Thus, because of the capital cost of the PHS system, the first scenario is more economical than the second scenario.

In both projects, PC is lower than the price of electricity (POP); in the first scenario, PC is 126% lower than POP and, in the second scenario, this number is 96%, which is the advantage of using renewable energies with low energy costs.

Figure 10 shows the effects of the real interest rate on economic parameters. Increasing the real interest rate decreases the NPV and increases the LCOP and the ACS of the system (Figure 10). The slopes of the curves for the second scenario are higher than those of the first scenario. The real interest rate for the current project is 0.0554 (Figure 11), which is a high value; the detailed values are provided in Table 7 for Iran. That means, in countries with the low values of the real interest rate, the project will be more profitable in particular for the second scenario. For example, 10% lessening the real interest rate can improve all parameters about 2% (Figure 10). As it is seen, the economic parameters are not too sensitive to real interest rate.

The value of POP for this project is 0.0879 (Table 7), which is shown in Figure 11. For this project, the period of return (POR) is 9.46 years for the first scenario and 13.05 years for the second one. In Figure 11, the slopes of the curves at the

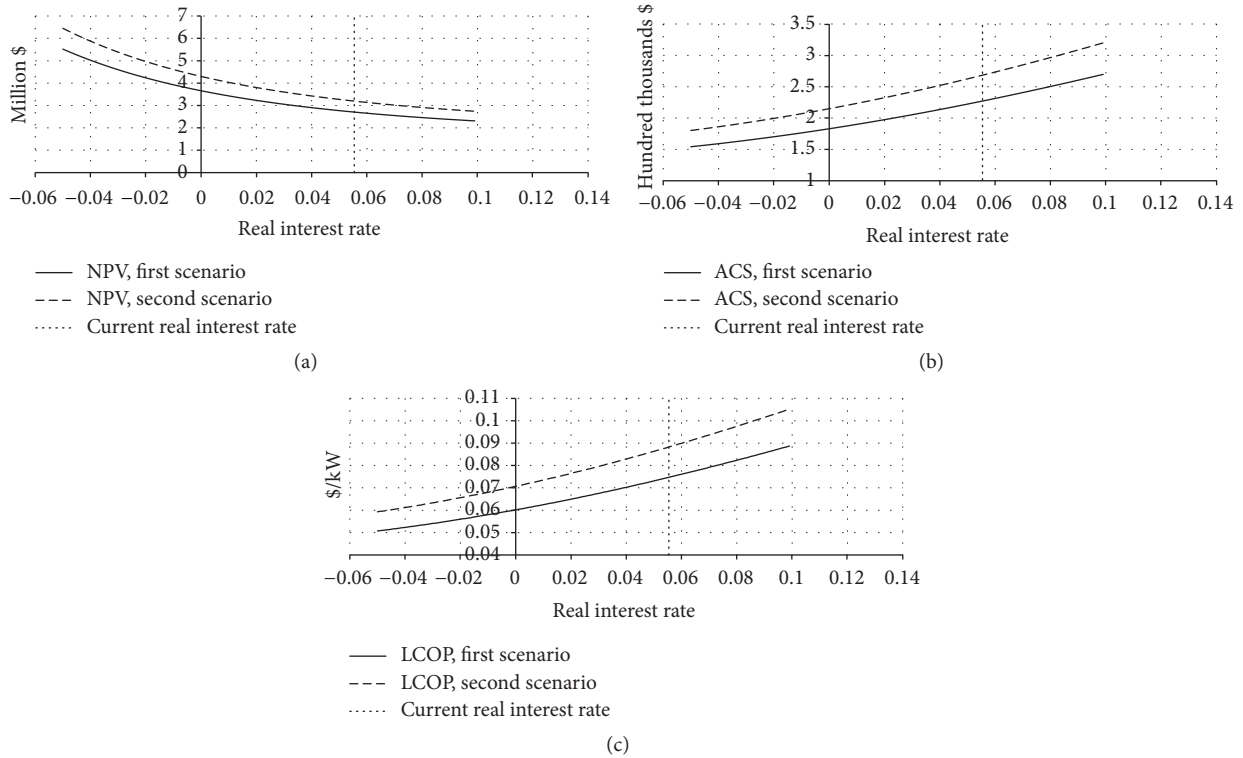


FIGURE 10: Variation of (a) NPV, (b) ACS, and (c) LCOP versus real interest rate.

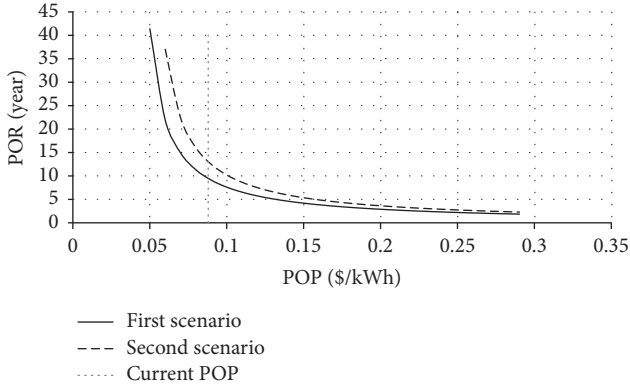


FIGURE 11: Variation of POR versus POP.

beginning are very high; then, small changes in the POP can make significant changes in the POR. For the second scenario, about 15% increase in POP decreases the POR under 10 years making the project more economical.

7. Conclusion

For a combined IRSOFC-HAWT system, thermodynamic and economic analyses were done based on two scenarios: an on-grid-IRSOFC-HAWT system and an off-grid-IRSOFC-HAWT system with a PHS. Based on the thermodynamic analysis, the best working condition for the IRSOFC was chosen and then a proper HAWT was designed to generate the demand power of a village in Manjil, Iran. The high capital

cost of the PHS dominated the economic parameters and made the second scenario the worst one from the economic point of view. The POR for the second scenario is about 3 years longer compared to that of the first scenario which was 9.46 years. Although the second scenario is less economical, for the case of having no access to the grid, this scenario makes the project possible. If the price of the electricity or the POP was increased only 15%, around 30% of the years of the POR would be reduced, making the second scenario more economical. In both projects, PC is lower than the price of electricity (POP), which is the advantage of using renewable energies with low energy costs.

It is suggested for the future work of this study that the waste heat of the system be used directly for the heating and cooling purposes, making both scenarios more profitable.

Nomenclature

- A: Area [m^2]
- AB: Annual Benefit [\$]
- A, B: Constants [—]
- ACS: Annualized Cost of System [\$]
- c: Chord [m]
- C: Cost [\$]
- C_D : Drag coefficient [—]
- C_L : Lift coefficient [—]
- C_p : Power coefficient [—]
- CRF: Capital Recovery Factor [—]
- D: Diameter [m]
- E: Cell voltage [V]

E_{Act} :	Activation energy [kJ/mol]
f :	Annual inflation rate [—]
F :	Prandtl's correction factor [—]
F :	Faraday constant [C]
i_0 :	Exchange current density [A/m^2]
i :	Current density [A/m^2]
i :	Real interest rate [—]
I :	Current density [A/cm^2]
i_j :	Limiting current density [A/m^2]
j :	Nominal interest rate [—]
L :	Length [m]
LCOP:	Levelized Cost of Product [$\$/\text{kW}$]
\dot{m} :	Mass flowrate [kg/s]
n :	Number of cells [—]
N :	Number of blades [—]
NAB:	Net Annual Benefit [$\$$]
n_e :	Number of electrons [—]
NPV:	Net Present Value [$\$$]
OFC:	Operating Flow Cost [$\$$]
p :	Partial pressure [—]
P :	Pressure [bar]
PC:	Prime Cost [$\$/\text{kW}$]
POP:	Price of Product [$\$/\text{kW}$]
POR:	Period of return [year]
r :	Resistance [Ω]
r :	Radius [m]
R :	Universal gas constant [J/mol]
R :	Radius [m]
Re:	Reynolds number [—]
SOPC:	Summation of Product Cost in a year [$\$$]
T :	Temperature [K]
VOP:	Volume of Product [kW]
\dot{W} :	Power [Watts]
x, y, z :	Molar rate [mol/s]
Y :	Year [—].

Greek Letters

β :	Heat transfer coefficient [—]
γ :	Preexponential factor [A/m^2]
δ :	Thickness [cm]
ΔG° :	Gibbs free energy changes at standard condition [—]
η :	Overpotential [V]
λ_r :	Tip speed ratio at radius r [—]
ρ :	Resistivity [$\Omega\cdot\text{cm}$]
φ :	Angle between the resultant velocity and the rotor plane [degree].

Subscript

acap:	Annualized capital cost
Act:	Activation
amain:	Annualized maintenance cost
An:	Anode
aope:	Annualized operating cost
arep:	Annualized replacement cost
Ca:	Cathode
Cap:	Capital
cc:	Combustion chamber

comp:	Compressor
Conc:	Concentration
GT:	Gas turbine
HX:	Heat exchanger
i :	Section number of the blade
inv:	Inverter
proj:	Project
ref:	Reference
rep:	Replacement
rev:	Reversible.

Conflicts of Interest

The authors declare that they have no conflicts of interest.

References

- [1] S. Soheyli, M. H. Shafiei Mayam, and M. Mehrjoo, "Modeling a novel CCHP system including solar and wind renewable energy resources and sizing by a CC-MOPSO algorithm," *Applied Energy*, vol. 184, pp. 375–395, 2016.
- [2] A. Fathy, "A reliable methodology based on mine blast optimization algorithm for optimal sizing of hybrid PV-wind-FC system for remote area in Egypt," *Renewable Energy*, vol. 95, pp. 367–380, 2016.
- [3] S. Obara, J. R. Morel Rios, and M. Okada, "Control of cyclic fluctuations in solid oxide fuel cell cogeneration accompanied by photovoltaics," *Energy*, vol. 91, pp. 994–1008, 2015.
- [4] M. Hosseini, I. Dincer, and M. A. Rosen, "Hybrid solar-fuel cell combined heat and power systems for residential applications: Energy and exergy analyses," *Journal of Power Sources*, vol. 221, pp. 372–380, 2013.
- [5] T. Vigneysh and N. Kumarappan, "Autonomous operation and control of photovoltaic/solid oxide fuel cell/battery energy storage based microgrid using fuzzy logic controller," *International Journal of Hydrogen Energy*, vol. 41, no. 3, pp. 1877–1891, 2016.
- [6] D. Tenfen and E. C. Finardi, "A mixed integer linear programming model for the energy management problem of microgrids," *Electric Power Systems Research*, vol. 122, pp. 19–28, 2015.
- [7] R. K. Akikur, R. Saidur, H. W. Ping, and K. R. Ullah, "Performance analysis of a co-generation system using solar energy and SOFC technology," *Energy Conversion and Management*, vol. 79, pp. 415–430, 2014.
- [8] W. Bai, M. R. Abedi, and K. Y. Lee, "Distributed generation system control strategies with PV and fuel cell in microgrid operation," *Control Engineering Practice*, vol. 53, pp. 184–193, 2016.
- [9] S. H. Chan, H. K. Ho, and Y. Tian, "Modelling of simple hybrid solid oxide fuel cell and gas turbine power plant," *Journal of Power Sources*, vol. 109, no. 1, pp. 111–120, 2002.
- [10] J. Pirkandi, M. Ghassemi, M. H. Hamed, and R. Mohammadi, "Electrochemical and thermodynamic modeling of a CHP system using tubular solid oxide fuel cell (SOFC-CHP)," *Journal of Cleaner Production*, vol. 29–30, pp. 151–162, 2012.
- [11] J. Larminie and A. Dicks, *Fuel Cell Systems Explained*, John Wiley & Sons, West Sussex, UK, 1st edition, 2003.
- [12] S. H. Chan, K. A. Khor, and Z. T. Xia, "Complete polarization model of a solid oxide fuel cell and its sensitivity to the change of cell component thickness," *Journal of Power Sources*, vol. 93, no. 1–2, pp. 130–140, 2001.

- [13] P. Costamagna and K. Honegger, "Modeling of solid oxide heat exchanger integrated stacks and simulation at high fuel utilization," *Journal of the Electrochemical Society*, vol. 145, no. 11, pp. 3995–4007, 1998.
- [14] R. Gasch and J. Twele, Eds., *Windkraftanlagen: Grundlagen, Entwurf, Planung und Betrieb*, Springer-Verlag, 2010.
- [15] J. Manwell, *Wind Energy Explained: Theory, Design and Application*, 1st edition, 2002.
- [16] M. Hansen, *Aerodynamics of Wind Turbines*, Earthscan, Sterling, VA, USA, 1st edition, 2008.
- [17] J. Hernandez and A. Crespo, "Aerodynamic calculation of the performance of horizontal axis wind turbines and comparison with experimental results," *Wind Engineering*, vol. 11, no. 4, pp. 177–187, 1987.
- [18] M. Meratizaman, S. Monadzadeh, and M. Amidpour, "Introduction of an efficient small-scale freshwater-power generation cycle (SOFC-GT-MED), simulation, parametric study and economic assessment," *Desalination*, vol. 351, pp. 43–58, 2014.
- [19] M. Gökçek and M. S. Genç, "Evaluation of electricity generation and energy cost of wind energy conversion systems (WECSs) in Central Turkey," *Applied Energy*, vol. 86, no. 12, pp. 2731–2739, 2009.
- [20] P. Du and N. Lu, *Energy Storage for Smart Grids: Planning and Operation for Renewable and Variable Energy Resources (VERs)*, Academic Press, 2014.
- [21] M. G. Khalfallah and A. M. Koliub, "Effect of dust on the performance of wind turbines," *Desalination*, vol. 209, no. 1-3, pp. 209–220, 2007.
- [22] ASDC — Processing, archiving, and distributing Earth science data at the NASA Langley Research Center, <https://eosweb.larc.nasa.gov/> [Accessed 5 April 2017].
- [23] H. Auer, M. Stadler, G. Resch, T. Schuster, J. Twidell, and D. J. Swider, "Pushing A Least Cost Integration Of Green Electricity Into The European Grid (GreenNet)-Cost and Technical Constraints of RES-E Grid Integration," Tech. Rep., Energy Economics Group, 2006.

Research Article

Enhancing LVRT Capability of DFIG-Based Wind Turbine Systems with SMES Series in the Rotor Side

Xiao Zhou, Yuejin Tang, and Jing Shi

State Key Laboratory of Advanced Electromagnetic Engineering and Technology, R&D Center of Applied Superconductivity, Huazhong University of Science and Technology, Wuhan 430074, China

Correspondence should be addressed to Jing Shi; shijing@mail.hust.edu.cn

Received 29 March 2017; Accepted 7 May 2017; Published 13 June 2017

Academic Editor: Lei Chen

Copyright © 2017 Xiao Zhou et al. This is an open access article distributed under the Creative Commons Attribution License, which permits unrestricted use, distribution, and reproduction in any medium, provided the original work is properly cited.

The necessary Low Voltage Ride Through (LVRT) capability is very important to wind turbines. This paper presents a method to enhance LVRT capability of doubly fed induction generators- (DFIGs-) based wind turbine systems with series superconducting magnetic energy storage (SMES) in the rotor side. When grid fault occurs, series SMES in the rotor side is utilized to produce a desired output voltage and absorbs energy. Compared with other methods which enhance LVRT capability with Superconducting Fault-Current Limiter-Magnetic Energy Storage System (SFCL-MESS), this strategy can control the output voltage of SMES to suppress the transient AC voltage component in the rotor directly, which is more effective and rapid. Theoretical study of the DFIG under low voltage fault is developed; the simulation results are operated by MATLAB/Simulink.

1. Introduction

Wind energy generation has experienced a fast development in the last two decades [1]. DFIG is the most widely used wind turbine, but it is vulnerable to low voltage fault. Many wind turbines trip off from the grid due to the lack of LVRT capability [2].

There are many enhanced ways to solve this problem. Crowbar is a commonly used protection method to implement the LVRT capability [3–5]; it can effectively suppress overvoltage and overcurrent but it needs to absorb a large amount of reactive power from the grid, which will do harm to the grid. Improving control strategy of grid converter or rotor converter has been studied by many researchers [6–8], but it cannot work effectively when deep voltage drop occurs. Energy storage device is suitable for dynamic matching of intermittent wind power. The use of supercapacitors or batteries for WTGs has been studied by some researchers [9–11]. SMES used in DFIGs to reduce power fluctuation and alleviate the influence on power quality has been studied in some papers [12]. The application of SFCL-SMES in the rotor side of the DFIG has been carried out. But it is connected with the DFIG through a three-phase diode rectifier; thus the SFCL-MES is inserted into rotor circuit as an impedance,

which will not provide help in enhancing the controllability of the RSC.

This paper presents a new method to enhance LVRT capability of DFIG with SMES. SMES, with its high efficiency and quick response ability to power compensation, could be a good choice for ESD in DFIG. Most studies applied ESD to solve the problem which are usually in parallel with the DC side. The proposed method in this paper is to generate a desired output voltage utilizing series SMES in the rotor side. Through the analysis of the rotor side voltage under low voltage fault, counter-electromotive force generated by SMES can counteract overvoltage and then overcurrent quickly and effectively. The mathematical model of DFIG will be illustrated first. Then, behavior of the DFIG in normal situation and under low voltage fault will be analyzed and the control strategy of VSC-SMES will be introduced.

2. Math Model of DFIG

The stator windings of the DFIG wind turbine are directly connected to the grid. The rotor winding is connected to the grid via back-to-back transformers, where the converter near the grid side is called grid sided converter (GSC) while

near the rotor side converter it is called rotor sided converter (RSC). The stator voltage is provided by the grid. The rotor voltage is provided by the back-to-back transformers, which can be adjusted in frequency, phase, and amplitude.

In this paper, the control system is implemented considering a stator voltage oriented (SVO) control philosophy in the d/q reference frame [13]. In this kind of systems, the d/q -axes are aligned with the stator voltage. Thus, the park model of the DFIG can be expressed as follows:

$$\begin{aligned}
 u_{dr} &= R_r i_{dr} + \frac{d\psi_{dr}}{dt} - (\omega_1 - \omega_r) \psi_{qr} \\
 u_{qr} &= R_r i_{qr} + \frac{d\psi_{qr}}{dt} + (\omega_1 - \omega_r) \psi_{dr} \\
 u_{ds} &= R_s i_{ds} + \frac{d\psi_{ds}}{dt} - \omega_1 \psi_{qs} \\
 u_{qs} &= R_s i_{qs} + \frac{d\psi_{qs}}{dt} + \omega_1 \psi_{ds} \\
 \psi_{ds} &= L_s i_{ds} + L_m i_{dr} \\
 \psi_{qs} &= L_s i_{qs} + L_m i_{qr} \\
 \psi_{dr} &= L_m i_{ds} + L_r i_{dr} \\
 \psi_{qr} &= L_m i_{qs} + L_r i_{qr}
 \end{aligned} \tag{1}$$

where ψ is the magnetic flux, L is the inductances, u and i are voltage and current, respectively, R is the resistance, subscripts s, r, m represent the stator, rotor, and mutual, respectively, and ω_1 and ω_r are the synchronous and rotating angular frequencies ($\omega_s = \omega_1 - \omega_r$).

Once there is a grid fault, the stator voltage will change immediately because it is connected to the grid directly. But, according to the principle of flux conservation, the amplitude of stator flux will not transition. At the moment when the voltage drops, the stator flux linkage contains an AC component and a DC component, which will induce overvoltage in rotor side with different frequencies.

As analyzed in [14], the rotor back EMF voltage can be expressed as follows:

$$\begin{aligned}
 u_{rdq} &= j \frac{L_m}{L_s} \omega_s \psi_{s2dq} \\
 &\quad - j \frac{L_m}{L_s} \omega_r (\psi_{s0dq} - \psi_{s2dq}) e^{-\sigma t} e^{-j\omega_s t},
 \end{aligned} \tag{2}$$

where ψ_{s0dq} and ψ_{s2dq} are normal-state stator flux and fault-state stator flux. The rotor back EMF voltage is mainly decided by part two of (2) because the slip frequency is much smaller than rotor frequency. And the second part in (2) is decided by the stator flux which can be several times the default value.

3. Methodology of DFIG and SMES Model

Unlike SFCL-MES, this paper controls the SMES output voltage through converter switch control, which could suppress the overvoltage in rotor side.

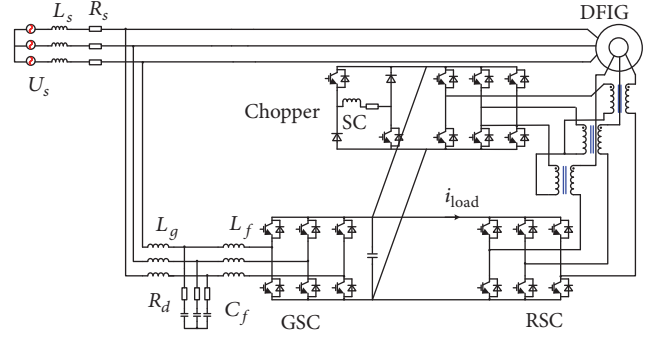


FIGURE 1: Topology of the whole system.

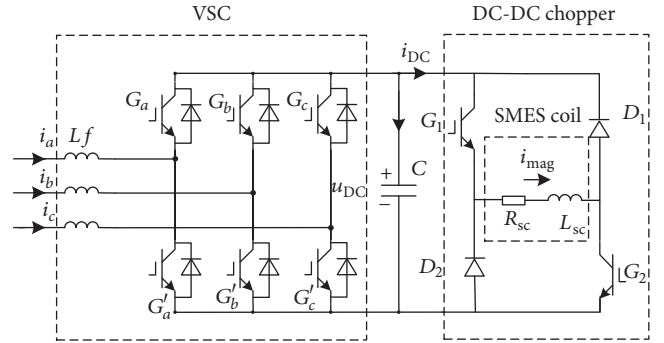


FIGURE 2: Topology of VSC-SMES.

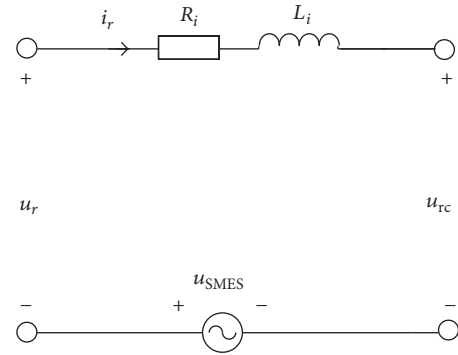


FIGURE 3: Equivalent circuit of the series SMES.

The topology of the whole system is shown in Figure 1. SMES is connected to the rotor side by a Voltage Source Converter (VSC). Topology of VSC-SMES is given in Figure 2. SMES can exchange active and reactive power with the system quickly and independently [13].

In the case of normal power supply, SMES is in standby mode. In this case, the series SMES will introduce resistance and reactance to DFIG. Thus the rotor voltage will not equate to rotor converter voltage. As shown in Figure 3, R_i and L_i are the introduced resistance and reactance, respectively. In order to eliminate the influence of the rotor voltage by series SMES, the control of series SMES is to realize

$$u_r = u_{rc}. \tag{3}$$

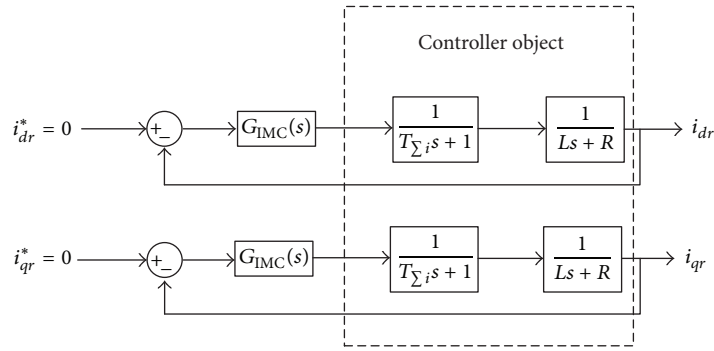


FIGURE 4: The current inner loop control stratagem.

When low voltage fault occurs, the SMES outputs the voltage to suppress the rotor back EMF voltage induced by stator; thus the rotor current is supposed to be zero when fault occurs and the rotor back EMF voltage induced by stator u_r^* can be shown as follows:

$$\begin{aligned} u_{dr}^* &= L_m \frac{di_{ds}}{dt} \\ u_{qr}^* &= L_m \frac{di_{qs}}{dt}. \end{aligned} \quad (4)$$

The stator current under grid fault after doing Laplace transform can be expressed as follows [15]:

$$\begin{aligned} i_{ds} &= \frac{(L_s + R_s)u_{ds} + \omega_1 L_s u_{qs}}{(L_s^2 s^2 + 2L_s R_s s + R_s^2 + \omega_1^2 L_s^2)} \\ &\quad - \frac{(L_s s^2 + R_s s + \omega_1^2 L_s)L_m i_{dr} - R_s \omega_1 L_m i_{qr}}{(L_s^2 s^2 + 2L_s R_s s + R_s^2 + \omega_1^2 L_s^2)} \\ i_{qs} &= \frac{(L_s + R_s)u_{qs} - \omega_s L_s u_{ds}}{(L_s^2 s^2 + 2L_s R_s s + R_s^2 + \omega_1^2 L_s^2)} \\ &\quad - \frac{(L_s s^2 + R_s s + \omega_1^2 L_s)L_m i_{qr} + R_s \omega_1 L_m i_{dr}}{(L_s^2 s^2 + 2L_s R_s s + R_s^2 + \omega_1^2 L_s^2)}. \end{aligned} \quad (5)$$

Considering that $R_s^2, R_s \omega_s L_m$ are approximately 0, the equation can be simplified as:

$$\begin{aligned} i_{ds} &= \frac{1}{L_s^2} \frac{L_s s + R_s}{s^2 + 2(R_s/L_s) + \omega_1^2} \cdot u_{ds} - \frac{L_m}{L_s} \cdot i_{dr} \\ i_{qs} &= \frac{1}{L_s^2} \frac{(-L_s \omega_1)}{s^2 + 2(R_s/L_s) + \omega_1^2} \cdot u_{ds} - \frac{L_m}{L_s} \cdot i_{qr}. \end{aligned} \quad (6)$$

According to the above analysis, if the rotor side converter could provide relative excitation voltage to u_r^* , the low LVRT capability of DFIG will be enhanced. Thus set u_r^* as the reference voltage of VSC-SMES under grid fault. The VSC-SMES reference voltage calculation process is presented in Figure 5.

3.1. SMES Control

3.1.1. VSC Control. As shown in Figure 2, through the park transformation, the mathematical model of VSC in the dq reference frame is expressed as follows:

$$\begin{aligned} L \frac{di_d}{dt} &= -Ri_d + \omega Li_q + u_{sd} - u_{DC} s_d \\ L \frac{di_q}{dt} &= -Ri_q - \omega Li_d + u_{sq} - u_{DC} s_q \\ C \frac{du_{DC}}{dt} &= \frac{3}{2} (i_q s_q + i_d s_d) - i_{chopper}. \end{aligned} \quad (7)$$

The current inner loop control of VSC adopts the internal model control strategy [14]; the control block diagram is shown in Figure 4. The closed-loop transfer function of the current inner loop is

$$W_{ci}(s) = \frac{1}{T_f^2 s^2 + 2\xi T_f s + 1}. \quad (8)$$

For achieving the purpose of rapid response of the current inner loop, let T_f be equal to 0.0002 s.

3.1.2. DC-DC Chopper Control. Chopper has two basic modes of operation: (1) magnetizing mode; (2) releasing magnetic mode. The mathematical model of chopper is

$$\begin{aligned} L_{sc} \frac{di_{mag}}{dt} &= -R_{sc} i_{mag} + (D_1 + D_2 - 1) u_{DC} \\ C \frac{du_{DC}}{dt} &= -(D_1 + D_2 - 1) i_{mag} + i_{DC}, \end{aligned} \quad (9)$$

where i_{mag} is the current of magnet and D is the switch state of each switch; if switch 1 is on, D_1 is equal to 1.

In normal operation, the control of chopper is to limit the magnet current in a setting scale. When low voltage fault happens, the control of chopper is to maintain the stability of the DC voltage. The control strategy of SMES is shown in Figure 5.

3.2. RSC Control. In normal operation, the control of d/q component of rotor current is to control the active and

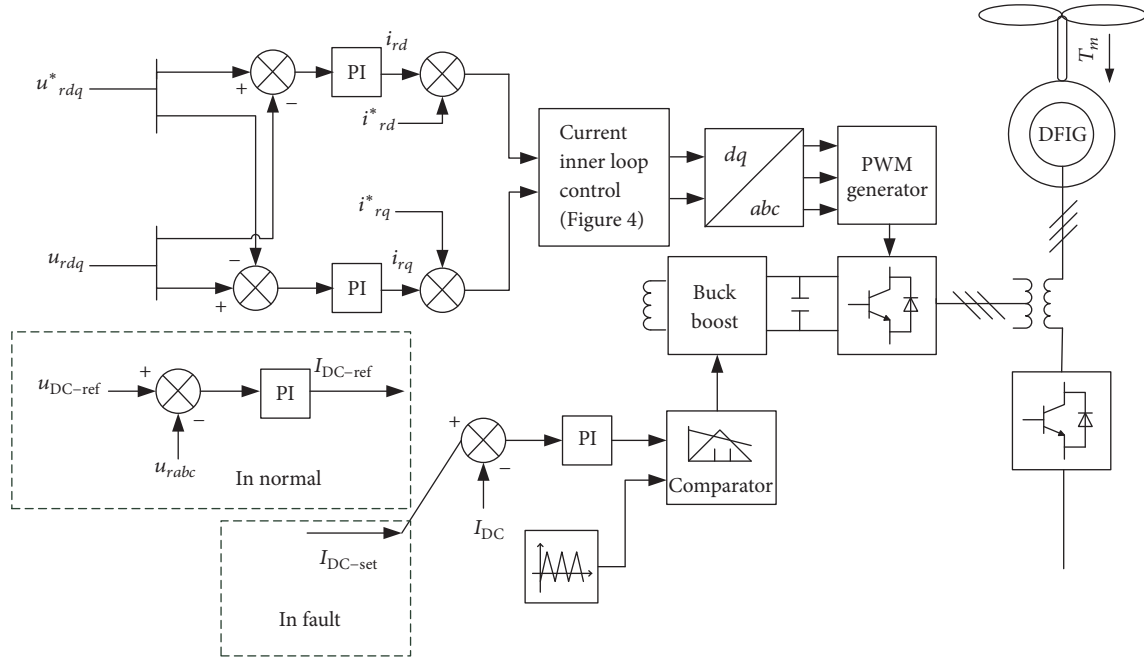


FIGURE 5: The control stratagem for SMES.

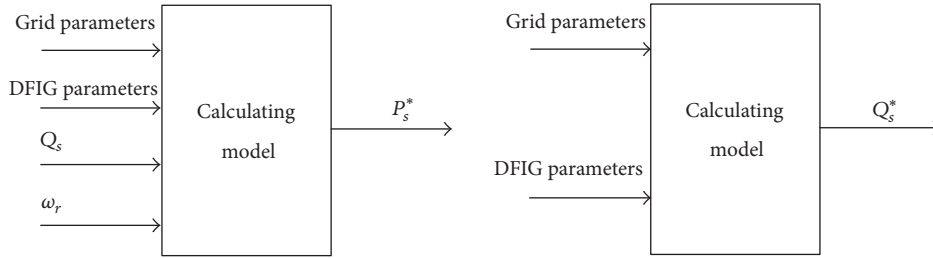


FIGURE 6: Reference power calculation model of DFIG.

reactive power of DFIG. Generally, the purpose of control system is to obtain the max wind power.

The essence of the maximum wind energy tracking is to control the DFIG output active power and control electromagnetic torque to achieve the best speed control. When the mechanical output of the wind turbine achieves maximum output power, the reference active power of DFIG P_s^* is equal to stator power P_s , as shown as follows:

$$P_s^* = \frac{1}{1-s} (P_{\max} - P_{ms}) - P_{cus}, \quad (10)$$

where P_{ms} is the mechanical loss of wind turbine and P_{cus} is the copper loss of stator, which is related to I_s and R_s . After doing identity transformation, (9) can be expressed as follows:

$$A(P_s^*)^2 + BP_s^* + C = 0 \quad (11)$$

$$A = \frac{R_s}{3U_s^2}, \quad B = 1, \quad C = \frac{1}{s-1} (k_w \omega_w^3 - P_{ms}) + \frac{R_s}{3U_s^2} Q_s.$$

The reactive reference power value Q_s^* can be calculated by achieving the lowest loss of DFIG or improving the system's ability to regulate power. In this paper, Q_s^* is calculated to achieve the lowest loss of DFIG. Thus the expression of Q_s^* is shown as follows:

$$Q_s^* = -\frac{3X_s R_r U_s^2}{R_s X_m^2 + R_r R_s^2 + R_r X_s^2}. \quad (12)$$

The reference power calculation model of DFIG is shown in Figure 6.

When a fault occurs, the control strategy of rotor converter is irrelevant. Considering SMES will absorb the wind energy, i_{dr}^* and i_{qr}^* can be set to zero to prevent the energy through the converter. Thus, the capacitor in DC side will not absorb a lot of energy and its voltage will not increase sharply. The control stratagem of RSC, in normal situation and when voltage drop happens, is shown in Figure 7.

3.3. GSC Control. The purpose of GSC control is to maintain DC capacitor voltage stability and control the factor of input

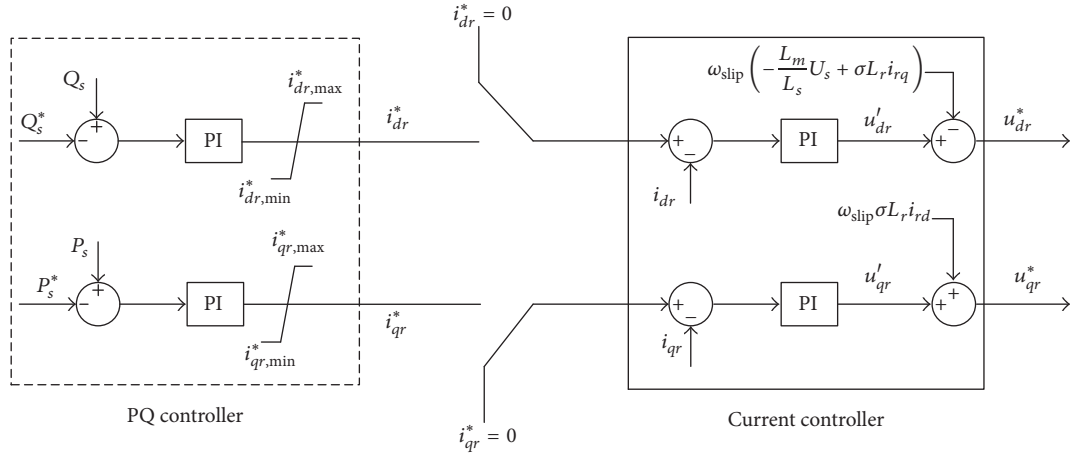


FIGURE 7: Control block diagram of the RSC.

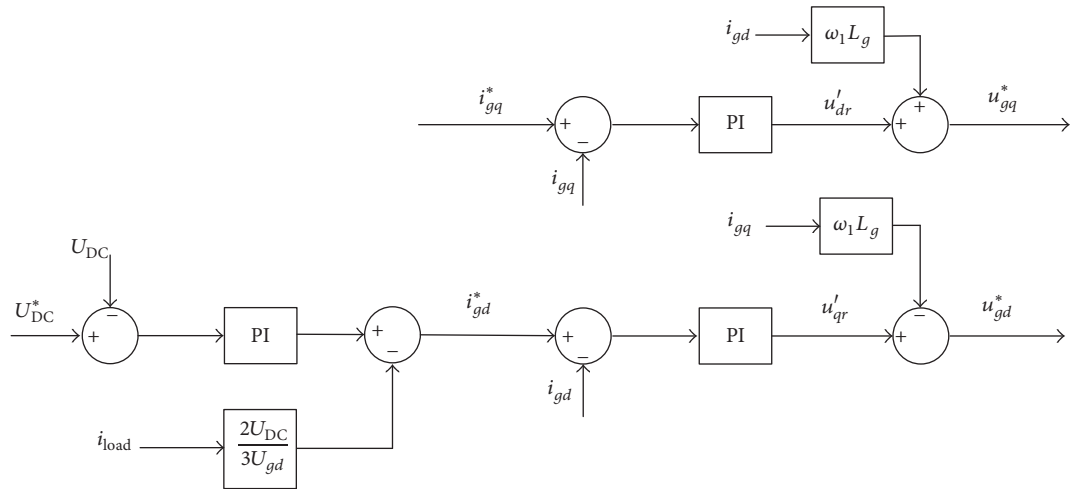


FIGURE 8: Control block diagram of the GSC.

power. The GSC control system is divided into two parts: the outer voltage loop and the inner current loop, which is shown in Figure 8. Compensation of load disturbances is achieved by feedforward of the load current i_{load} . System is decoupled by introduced current state feedback $\omega_1 L_g i_{gd}$, $\omega_1 L_g i_{gq}$.

4. Economic Analysis

Compared to other energy storage devices, SEMS has the advantage of high response speed, high efficiency, high-power density, and high cycle life characteristics. But the application of SMES in DFIG will increase the cost of the system. Therefore, the capital cost of SMES applied in DFIG is an indispensable part of DFIG's technical performance. In terms of energy storage devices, the capital costs contain energy cost \$/kWh, power cost \$/kW, and cycle cost. As the energy storage device is used in DFIG, high-power characteristic is necessary. The power costs of SMES are less

than their energy costs, and this is an indication that they are suitable for high-power applications. Table 1 shows the cost comparison for the storage technologies [16]. As can be seen from the table, SMES has a lower power cost compared to pumped-hydro storage, lithium-ion batteries and other energy storage devices. In addition, the long life of SMES makes it possible to participate in the protection of the entire life of the DFIG. In general, considering the economic and other technical performances, SMES is a good choice for ESD in DFIG.

5. Simulation Analysis and Conclusion

The simulations are carried out in MATLAB/Simulink. The simulation parameters are shown in Table 2. The simulation parameters of SMES are shown in Table 3. The purpose of the simulation is to observe the performance of the back-to-back converter when the grid fault occurs.

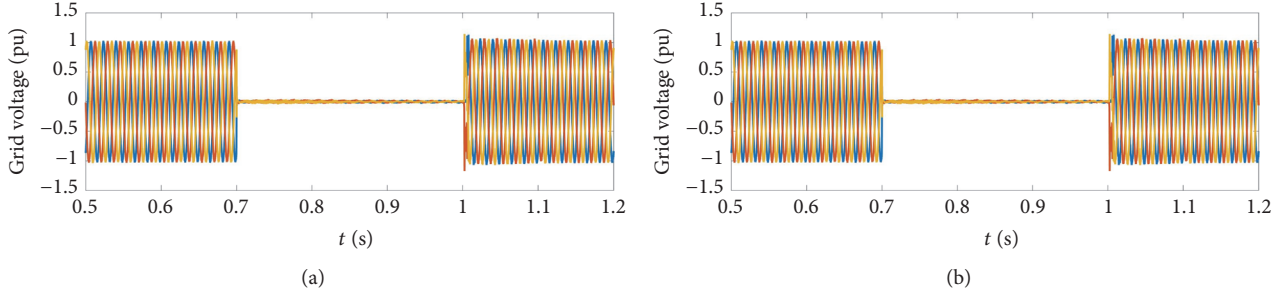


FIGURE 9: The grid voltage.

TABLE 1: Cost comparison for the storage technologies.

ESD	Capacity	Life	Power cost (\$/kW)	Energy cost (\$/kWh)
Pumped-hydro storage	100–2000 MW	>20 years	2000–4300	10–100
Compressed-air energy storage	100–300 MW	>20 years	400–1000	2–50
Flywheel energy storage	5 kW–1.5 MW	>15 years	250–350	1000–10000
Lithium-ion batteries	1–1000 kW	3000 cycles	1000–3000	1000–3800
Supercapacitors	1–100 kW	>50000 cycles	100–300	300–2000
Superconducting magnetic energy storage	10–500 kW	>20 years	200–400	500–1000
Vanadium redox battery	<10 MW	10–30 years	600–1500	150–1000

TABLE 2: DFIG parameters.

Symbol	Name	Quantity
S_N	Capacity	1.5 MW
f_N	System frequency	60 Hz
R_s	Stator resistance	0.016 p.u.
L_{ls}	Stator leakage inductance	0.16 p.u.
R_r	Rotor resistance	0.016 p.u.
L_{lr}	Rotor leakage inductance	0.16 p.u.
L_m	Magnetizing inductance	2.9 p.u.
S_b	Base capacity	1.5/0.9 MVA
f_b	Base frequency	60 Hz
V_{s_nom}	Base stator voltage (V_{rms})	575 V
V_{r_nom}	Base rotor voltage (V_{rms})	1975 V

TABLE 3: SMES parameters.

Parameter	Value
HTS material	Bi 2223
Capacity	40 kJ/600 kW
Magnet inductance (L)	0.5 H
Magnet resistance	$2 \times 10^{-5} \Omega$
Filter capacitance (C)	0.02 F
Series transformer ratio	1
Transformer resistance	$1 \times 10^{-4} \Omega$

The transient grid voltage fault occurs at 0.7 s and lasts for 300 ms. The grid voltage during fault drops to 0. The grid voltage is shown in Figure 9. Figures 10 and 11 compare the currents of stator converter and rotor converter with and without SMES. When there is no SMES, in the moment of

low voltage faults, the overcurrent of the stator and rotor side converters is almost five times larger than the normal operating range. With the proposed method, the currents of back-to-back converters are always in the affordable range. Moreover, as shown in Figure 13, the DC capacitor voltage is well suppressed during the fault. The output voltage of SMES in d/q frame is shown in Figure 12. The base voltage is the same as base rotor voltage. Figure 14 shows the transient SMES current response.

Compared to traditional control stratagem, the new control strategy with SMES can suppress the overcurrent in stator and rotor within the affordable range even when grid voltage drops to 0. The DC bus voltage can also be limited effectively.

This paper presents a new control stratagem to enhance the LVRT capability of DFIG with series SMES. By controlling the SMES output voltage with the proposed controller,

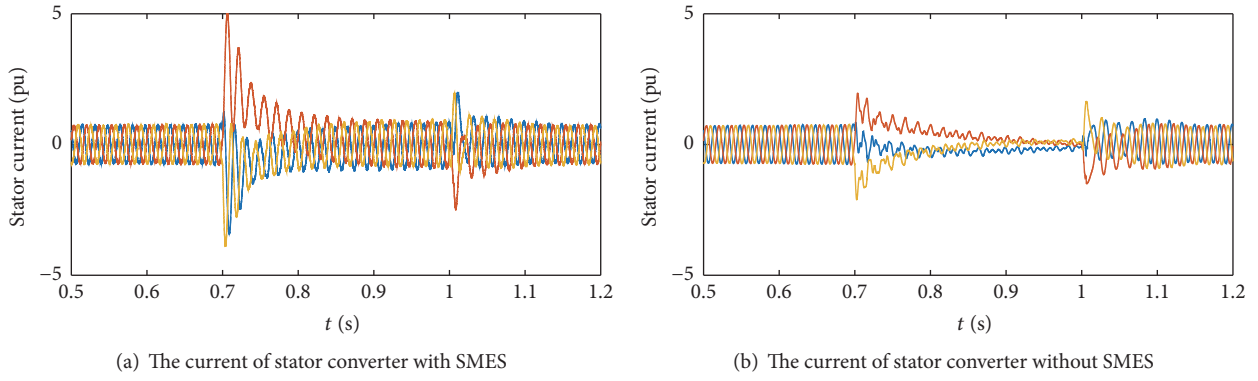


FIGURE 10

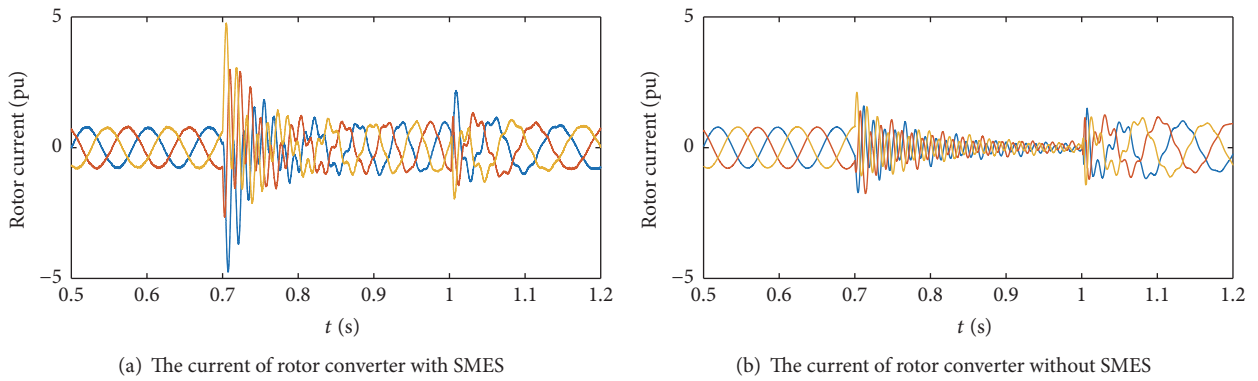


FIGURE 11

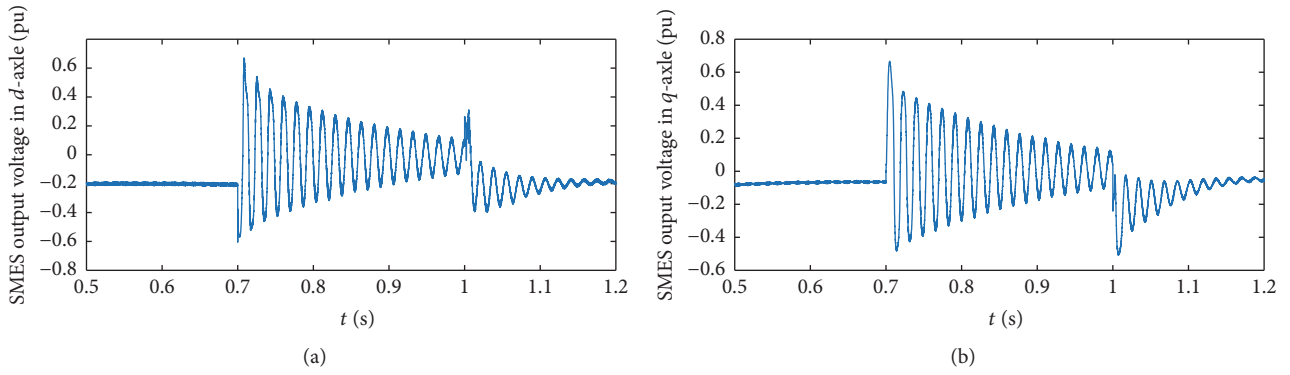


FIGURE 12: The SMES output voltage.

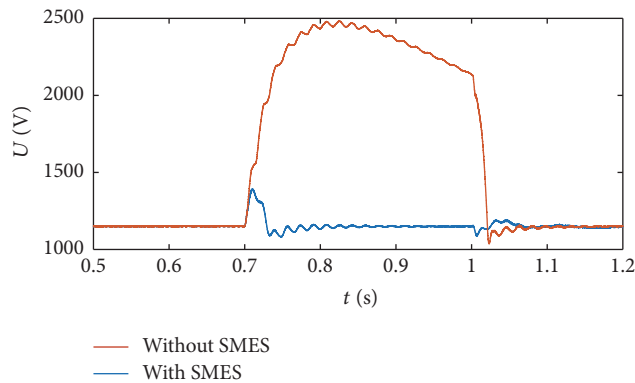


FIGURE 13: The DC voltage.

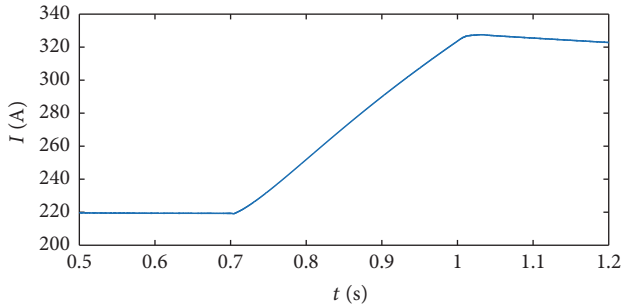


FIGURE 14: The magnet current of SMES.

the converter currents and capacitor voltage in fault are suppressed effectively. The method has been validated by simulations in MATLAB/Simulink.

Conflicts of Interest

There are no conflicts of interest regarding the publication of this paper.

References

- [1] Y.-W. Shen, D.-P. Ke, W. Qiao, Y.-Z. Sun, D. S. Kirschen, and C. Wei, "Transient reconfiguration and coordinated control for power converters to enhance the LVRT of a DFIG wind turbine with an energy storage device," *IEEE Transactions on Energy Conversion*, vol. 30, no. 4, pp. 1679–1690, 2015.
- [2] J. Liu, H. Zhang, B. Yang, and Y. Min, "Fault ride through under unbalanced voltage sag of wind energy conversion system using superconducting magnetic energy storage," in *Proceedings of the 2nd IEEE International Future Energy Electronics Conference*, Taipei, Taiwan, November 2015.
- [3] J. Niiranen, "Voltage dip ride through of a doubly-fed generator equipped with an active crowbar," in *Proceedings of the Nordic Wind Power Conference Nwpc*, 2004.
- [4] L.-L. Sun, P. Yang, and Y. Wang, "Simulation research for LVRT of DFIG based on rotor active crowbar protection," in *Proceedings of the International Conference on Sustainable Power Generation and Supply, SUPERGEN 2012*, pp. 1–7, Hangzhou, China, September 2012.
- [5] P. Su and K.-S. Zhang, "Simulation research for LVRT of DFIG with active IGBT Crowbar," *Power System Protection and Control*, vol. 38, no. 23, pp. 164–171, 2010.
- [6] J. Hu, H. Wang, Y. He, and L. Xu, "Improved rotor current control of wind turbine driven doubly fed induction generators during network unbalance," in *Proceedings of the 1st International Conference on Sustainable Power Generation and Supply, SUPERGEN '09*, pp. 1–7, Nanjing, China, April 2009.
- [7] T. K. A. Brekken and N. Mohan, "Control of a doubly fed induction wind generator under unbalanced grid voltage conditions," *IEEE Transactions on Energy Conversion*, vol. 22, no. 1, pp. 129–135, 2007.
- [8] A. G. Abo-Khalil, D.-C. Lee, and J.-I. Jang, "Control of back-to-back PWM converters for DFIG wind turbine systems under unbalanced grid voltage," in *Proceedings of the 2007 IEEE International Symposium on Industrial Electronics, ISIE 2007*, pp. 2637–2642, Vigo, Spain, June 2007.
- [9] C. Abbey and G. Joos, "Supercapacitor energy storage for wind energy applications," *IEEE Transactions on Industry Applications*, vol. 43, no. 3, pp. 763–776, 2007.
- [10] B. S. Borowy and Z. M. Salameh, "Dynamic response of a stand-alone wind energy conversion system with battery energy storage to a wind gust," *IEEE Transactions on Energy Conversion*, vol. 12, no. 1, pp. 73–78, 1997.
- [11] A. Yazdani, "Islanded operation of a doubly-fed induction generator (DFIG) wind-power system with integrated energy storage," in *Proceedings of the 2007 IEEE Canada Electrical Power Conference, EPC 2007*, pp. 153–159, Montreal, Canada, October 2007.
- [12] J. Shi, Y. Tang, Y. Xia, L. Ren, and J. Li, "SMES based excitation system for doubly-fed induction generator in wind power application," *IEEE Transactions on Applied Superconductivity*, vol. 21, no. 3, pp. 1105–1108, 2011.
- [13] Y. Zhang, Y. Tang, J. Li, J. Shi, and L. Ren, "Superconducting magnet based VSC suitable for interface of renewable power sources," *IEEE Transactions on Applied Superconductivity*, vol. 20, no. 3, pp. 880–883, 2010.
- [14] W. Guo, L. Xiao, and S. Dai, "Enhancing low-voltage ride-through capability and smoothing output power of DFIG with a superconducting fault-current limiter-magnetic energy storage system," *IEEE Transactions on Energy Conversion*, vol. 27, no. 2, pp. 277–295, 2012.
- [15] F. K. A. Lima, A. Luna, P. Rodriguez, E. H. Watanabe, and F. Blaabjerg, "Rotor voltage dynamics in the doubly fed induction generator during grid faults," *IEEE Transactions on Power Electronics*, vol. 25, no. 1, pp. 118–130, 2010.
- [16] D. O. Akinyele and R. K. Rayudu, "Review of energy storage technologies for sustainable power networks," *Sustainable Energy Technologies and Assessments*, vol. 8, pp. 74–91, 2014.

Research Article

Evaluation of Wind Energy Potential as a Power Generation Source in Chad

**Djamal Hissein Didane, Nurhayati Rosly, Mohd Fadhli Zulkafli,
and Syariful Syafiq Shamsudin**

*Department of Aeronautical Engineering, Faculty of Mechanical and Manufacturing Engineering,
Universiti Tun Hussein Onn Malaysia (UTHM), Parit Raja, 86400 Batu Pahat, Johor, Malaysia*

Correspondence should be addressed to Djamal Hissein Didane; dhdfils@gmail.com

Received 21 January 2017; Revised 17 April 2017; Accepted 30 April 2017; Published 31 May 2017

Academic Editor: Li Ren

Copyright © 2017 Djamal Hissein Didane et al. This is an open access article distributed under the Creative Commons Attribution License, which permits unrestricted use, distribution, and reproduction in any medium, provided the original work is properly cited.

Long-term wind speed data for thirteen meteorological stations, measured over a five-year period, were statistically analyzed using the two-parameter Weibull distribution function. The purpose of this study is to reveal for the first time the wind power potentials in Chad and to provide a comprehensive wind map of the country. The results show that the values of the shape and scale parameters varied over a wide range. Analysis of the seasonal variations showed that higher wind speed values occur when the weather condition is generally dry and they drop considerably when the weather condition is wet. It was also observed that the wind speed increases as one moves from the southern zone to the Saharan zone. Although the wind power at each site varies significantly, however, the potentials of most of the sites were encouraging. Nevertheless, according to the PNNL classification system, they are favorable for small-scale applications only. A few stations in the middle of Sudanian and Sahel regions are found to be not feasible for wind energy generation due to their poor mean wind speed. The prevailing wind direction for both Saharan and Sahel regions is dominated by northeastern wind, while it diverged to different directions in the Sudanian zone.

1. Introduction

The fast growing population in developing countries and their lack of access to electricity supply particularly in rural or remote areas make some of these nations face the challenge of generating more energy sources and establishing a new form of energy supply structure in an effort to meet current and future increasing electricity demands. Permanent electricity supply is considered as one of the major factors responsible for sustainable economic and social development of a nation [1]. In Chad, for example, although the country is an oil producer, access to energy is extremely limited and incessant power outage is still an everyday burden that undermines its development possibilities and needs a rapid action with a view to coping with the minimum requirement of the twenty-first century's lifestyle.

As such, the majority of people in Chad tend to rely on traditional biomass for cooking and heating purposes particularly in rural areas as it is the case for many African

nations [2]. A recent projection from the World Energy Outlook (WEO) [3] reported that more than 80% of the population in sub-Saharan Africa and 50% of the population in developing Asia depend on traditional biomass for cooking and heating. This situation has become more critical due to high fuel price in the country (considered the highest in the region) and the ever-increasing rate of the desert encroachment towards the Sahel region which forces the government to set some policies that prohibit deforestation and use of charcoal for cooking. Additionally, the government is also creating a green belt from the extreme east to the west of the country in order to halt the desertification process and to protect the region from economic and environmental impacts of land degradation.

Currently, a great deal of extensive research on wind energy is taking place almost all over the world due to the exceptional benefits that wind energy could offer. Many regional countries like Morocco, Egypt, Tunisia, Algeria, and so forth are already harvesting wind energy by establishing

wind farms in the open Sahara desert and coastal areas [4, 5]. Chad was not an exception to embrace such sustainable renewable energy source as an alternative energy since the preliminary study in the region shows that the wind conditions are favorable for wind energy adoption [5].

Chad experiences wind and sunlight throughout the year. Thus, it is interesting to explore the abundant untapped potentials of the wind and the possibilities of using the Wind Energy Conversion System (WECS) as a source of electricity in the effort to fulfill the energy requirements in the country and to reduce this exclusive dependency on biomass and fossil fuels. However, although the region is found to be situated in the midst of enormous wind power potentials, to date, there is no extensive study undertaken to assess the prospects of wind energy as an alternative source in the country, except in [6] which covered only a single city (N'djamena). Thus, this article could be the first of its kind to investigate the potentiality of wind power in Chad and it provides an initial assessment which together contributes towards the establishment of a comprehensive wind map/pattern for the country which may hopefully become the main wind energy reference for future development of wind power projects in the region.

2. Geographical Nature of Chad

Chad is a landlocked country with a 1,284,000 km² area, situated in Central Northern Africa. It is the 5th largest in the African continent and 21st in the world in terms of land mass. It is bordered by Libya from the north, Sudan from the east, the Central African Republic from the south, Niger from the west, and Cameroon and Nigeria from the southwest. It lies at 7–23° north of the equator and its larger part is Sahara desert. The vast majority of the area is flat with some plateaus around the country.

Unlike many countries in the world, the climate in Chad is highly varying throughout the country due to nonuniform geographical regions. These regions could be categorized into three in terms of geographical aspects as in Figure 1. The southern part is fertile agricultural land and is covered by tropical savanna, with a climate with longer raining season of about six months of precipitation. The raining season starts as early as May and ends around October. Meanwhile, the winter starts from November until February, and the summer takes place between February and May [7].

The region in the middle has an arid subtropical climate and it forms a belt of about 500 kilometers wide in the center of the country between the Sahara and Sudanian savanna. The raining season in this region begins a bit late with almost three months of rainfall duration. The first water drops are seen in June and then raining ends in September, while winter is between October and February. The Sahara desert occupies the northern part of the country with less population though it is the largest region as shown in Figure 1. Most of the people here are farmers and/or ranchers. Rain is less likely to be seen in this locality and these people only depend on underground water for the living. Thus, only a hotter summer or colder and dry winter exists in this region [7].



FIGURE 1: Geographical map of Chad [8].

3. Wind Data Collection

The wind data for this study are collected from the National Meteorological General Administration (Direction Générale de la Météorologie Nationale) at the Hassan Djamous International Airport in N'Djamena. The geographical coordinates of the thirteen major meteorological stations across the country are furnished in Table 1. The data extensively cover a wide range of five-year period and recorded in a monthly averaged form, at the standard 10 m height above ground level. These thirteen locations represent different geographical and climatological conditions, namely, Faya-Largeau, which is found in the Saharan zone; Abéché, Ati, Bokoro, Mao, Mongo, and N'djamena, which are located in the Sahelian zone; and Am Timan, Bousso, Doba, Pala, Moundou, and Sarh, which are situated at the Sudanian zone as shown in Figure 1.

Furthermore, although most of the data involved in this study are recent, the last observation made by some stations was in late 1978. This might be attributed to the fact that some of these stations are no longer recording such data in a consistent manner. However, due to the need to uncover the potential of these regions, they are being considered in this study by selecting five consecutive years, as it was learned that old or new data have a minor effect on the wind data assessment process as long as the study period is long enough [9, 10]. More so, [11, 12] stated that observation of less than 30 years may inherently cause variations in the long-term average, but for the sole purpose of resource assessment such period may be sufficient. However, covering longer periods would provide confidence to the interested investors that the wind potentials will be available in the coming years besides giving a more reliable evaluation [9, 10].

4. Analysis Procedure

It is commonly agreed that assessment of wind potential of a site using solely the conventional meteorological wind speed data is not sufficient. This is because depending on average wind speed alone to estimate the potential of a site might be

TABLE 1: Physical features of the meteorological stations.

Name of station	Coordinates					Elevation (m)
	Latitude (N)		Longitude (E)			
	Deg.	Min.	Deg.	Min.		
Abéché	14	40	20	50	545	
Am Timan	11	02	20	16	433	
Ati	13	14	18	18	332	
Bokoro	12	23	17	04	300	
Bouso	10	29	16	43	335	
Doba	08	42	16	50	387	
Faya-Largeau	17	55	19	06	235	
Mao	14	08	15	18	327	
Mongo	12	10	18	40	431	
Moundou	08	37	16	04	429	
N'Djaména	12	08	15	02	295	
Pala	09	22	14	55	467	
Sarh	09	09	18	22	365	

misleading [13]. This is due to the fact that the wind speed frequency distribution and persistence at a site are not constant and they vary significantly with time. As such, merely taking the average wind speed for a specific period of time does not take such consideration into account. Thus, statistical methods are used to reveal the wind characteristics of a potential site. Such statistical assessment of individual terrains or as a whole will collectively assist in establishing a clear wind map or wind pattern for a region while providing more detailed characteristics of the wind at the site such as wind distribution, stability, and direction, as the wind is known for its inherently intermittent behavior due to seasonal and temporal variations. The FirstLook software is commonly used to determine specific locations with higher wind power potentials, while the RIAM-COMPACT numerical model is responsible for suggesting the appropriate location to install a WECS during micro-siting analysis of terrains.

4.1. Weibull Distribution Function. Many statistical methods are available to closely estimate the wind power potentials and wind speed characteristics of a given terrain. Weibull distribution is among the widely accepted approaches to statistically assess the wind behavior at a particular site clearly [14]. This technique consists of several methods to evaluate the shape and scale parameters of Weibull, depending on the form of data available and the level of sophistication required [15]. In this method, the variations of wind speed are characterized by probability density function (PDF) (see (1)) and cumulative distribution function (CDF) (see (5)) [16]. The PDF indicates the fraction of time or the probability of which the wind speed prevails at a certain direction and the CDF shows the probability of which the wind speed is equal to or lower than the average speed [17].

Thus, in the current study, the meteorological data are statistically analyzed using the effective two-parameter Weibull distribution function. This approach is particularly useful in studying wind speed characteristics and wind energy density.

It is typically adopted due to its simplicity, flexibility, and ability to show good agreement with the observed data [18–26]. In addition, the majority of the known commercial software packages for Annual Energy Production (AEP) estimation are based on the two-parameter Weibull distribution function [27].

The two parameters are the dimensionless shape function, k (see (2)), and the scale function, c (see (3)), in meters per second unit. They, respectively, indicate the stability and strength of the wind at the site of interest [28].

$$f(v) = \left(\frac{k}{c}\right) \left(\frac{v}{c}\right)^{k-1} \exp\left[-\left(\frac{v}{c}\right)^k\right], \quad (1)$$

$(k > 0, v > 0, c > 1).$

$f(v)$ is the probability of observing wind speed v . c is the Weibull scale parameter and k is the dimensionless Weibull shape parameter and they are given by [15] as follows:

$$k = 0.83\bar{V}^{-0.5} \quad (2)$$

$$c = \frac{\bar{V}}{\Gamma(1 + 1/k)}. \quad (3)$$

Γ is the gamma function and \bar{V} is the average wind speed and can be expressed as

$$\bar{V} = \frac{1}{n} \left[\sum_{i=1}^n v_i \right]. \quad (4)$$

The cumulative distribution, given as in the equation below, is the integral of the probability density function:

$$F(v) = 1 - e^{-(v/c)^k}. \quad (5)$$

4.2. Wind Speed Carrying Maximum Energy. $V_{\max,E}$ represents the wind speed that carries the maximum wind energy

and it is determined using the shape and scale parameters of the Weibull distribution. It is highly significant as it can expose the maximum energy possible at the given site, and it is expressed as in (6) [29]. The wind speed that carries maximum energy is different from the highest wind speed and the average wind speed because it takes into account the scale and shape parameters of the Weibull distribution which are responsible for indicating the persistence, stability, and strength of the wind at the site under investigation as was mentioned earlier.

Thus, such estimation is quite important for the sake of revealing the wind speed that may carry the highest energy which could probably assist in knowing the maximum amount that can be expected from a particular site. Moreover, it is also used in selecting a suitable wind turbine or an appropriate rated wind speed [30]. As wind turbines perform efficiently at their rated wind speed, [31] suggests that the rated wind speed should be close to the wind speed carrying maximum energy:

$$V_{\max.E} = c \left(1 + \frac{2}{k}\right)^{1/k}. \quad (6)$$

4.3. Wind Power Density. Generating electricity from kinetic energy via wind that is flowing through a blade swept area, A , is proportional to the cube of the velocity and it can be described as follows in (7). A wind turbine starts to operate at the starting speed and produces useful energy at the cut-in speed. The corresponding power increases relative to the increase of the wind speed until the cut-out speed of the wind turbine. The maximum power is generated when the wind turbine is operated at the rated speed and power becomes constant when it operates between the rated speed and cut-out speed. At higher wind speeds above the cut-out speed, the turbine stops to avoid damage due to the higher wind velocity.

$$P(v) = \frac{1}{2} A \rho v^3. \quad (7)$$

The wind power density based on Weibull distribution analysis is calculated using the following equation [32]:

$$\frac{P}{A} = \int_0^{\infty} \frac{1}{2} \rho v^3 f(v) dv = \frac{1}{2} \rho c^3 \Gamma\left(\frac{k+3}{k}\right), \quad (8)$$

where ρ is the air density (1.225 kg/m^3) at sea level with a mean temperature of 15°C and 1 atmospheric pressure.

4.4. Wind Energy Density. After knowing the wind power density of a given site, one of the important wind characteristics could be estimated which is the wind energy density. It is the product of wind power density for a certain duration or period of time which can reveal the amount of energy density that could be expected at the site under study. The wind energy density for the desired time can easily be determined using the following equation [32]:

$$\frac{E}{A} = \frac{1}{2} \rho c^3 \Gamma\left(\frac{k+3}{k}\right) T, \quad (9)$$

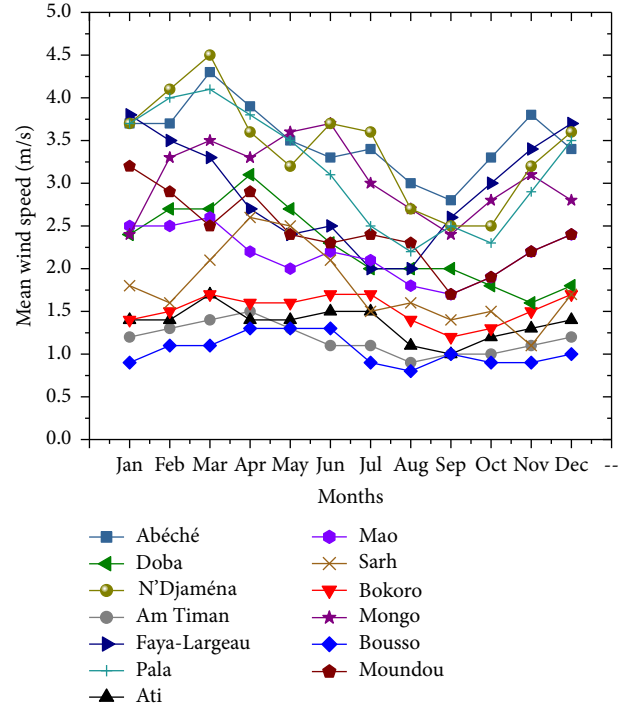


FIGURE 2: Monthly variation of wind speeds for all the selected stations.

where T is the desired time; for example, for wind energy density for a time period of one month or a year, the time, T , can be taken as 720 h or 8640 h, respectively.

5. Results and Discussion

5.1. Wind Speed Variation. The potential of wind energy in Chad was investigated at thirteen stations for a period of five years. Knowledge of monthly wind speed variations is essential to draw a clear picture of the seasonal wind speed behavior at the potential site. These fluctuations are significant in designing and selecting an appropriate WCES, energy storage, and load scheduling. These variations were determined using (4) and presented in Figure 2.

The trends of monthly and yearly mean wind speed for all the stations under investigation exhibit almost a similar pattern. The monthly mean wind speed varies in the range of 2 to 4 m/s for the Saharan region and in the range of 1 to 4 m/s for the Sahel and tropical Savanna regime. It was also observed that the wind speed tends to increase significantly when the weather condition is generally dry (November to May) and decreases considerably when the weather conditions are wet (June to October). It was learned that the highest demand for electricity is also at the dry period [6]. However, a few stations such as Bousso, Bokoro, and Am Timan maintained almost similar monthly mean wind speed throughout the year.

In general, it was established that stronger wind speed is available as one moves from south to north, towards the Sahara as depicted in Figure 3. In other words, some stations at the Savanna region have demonstrated lower wind speed

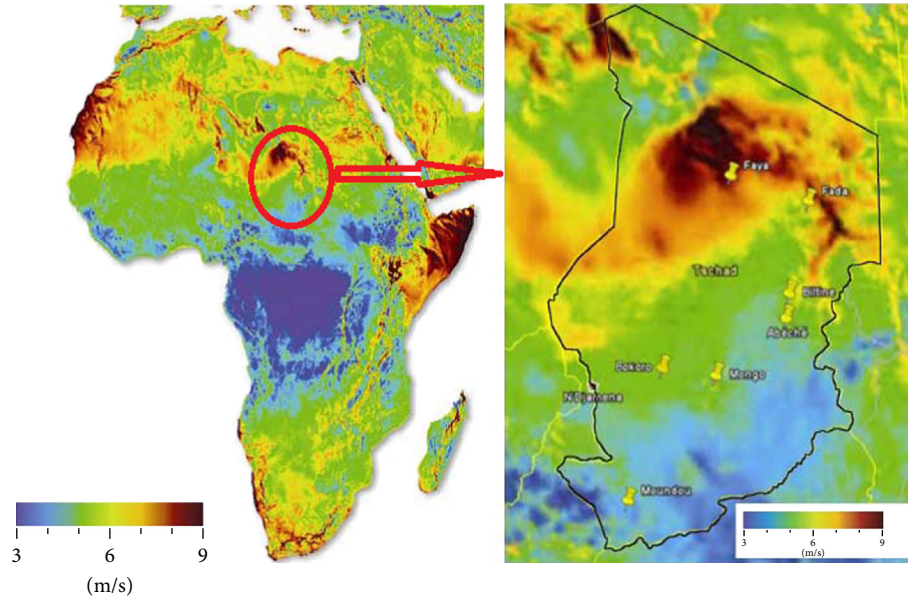


FIGURE 3: Wind speed pattern in Chad.

compared to the Sahel and Saharan regions with the exception of Ati and Bokoro. This could partly be attributed to the fact that the southern region is tropical with heavy forest and the land becomes clearer as one moves towards the north. However, it was specifically found that the stations at the middle of the Sahel and Sudanian zones showed the lowest mean wind speed with an annual average wind speed of less than 2 m/s as it is evident in Figures 2 and 3. This suggests that this area is less likely to be a potential location for wind energy harvesting.

Moreover, the seasonal wind speed variations among the three regions become more noticeable particularly during winter, though this variation is marginal between the Sahel and Saharan regions. The month March showed the highest mean wind speed with the value of 4.5 m/s, and August showed the lowest mean wind speed value of 0.8 m/s.

The results presented also showed that, within five years under study, the highest corresponding annual average wind speed at 10 m height from the ground is approximately 3.5 m/s, and it was found in the eastern part of the country at Abéché specifically, while the minimum is found at Bousso with a wind speed of 1.0 m/s. Thus, according to the PNNL (Pacific Northwest National Laboratory) classification system, wind energy potentials in Chad could only be used for small-scale applications due to the current wind conversion technologies and cost factor [32]. As such, this could probably solve the incessant power outage if a WECS is installed at every household and would also be quite useful for the ranchers who depend only on wells and use conventional methods to pump water.

However, it is worth noting that although the presented station from the Saharan region (Faya-Largeau) showed a bit lower wind speed compared to some stations in the Sahel region, data for wind speed at 30 m height proves otherwise.

Thus, the Sahara zone could be considered more promising as depicted in Figure 3.

5.2. Wind Power and Energy Density. Although wind speed characteristics are essential in drawing a clear picture of the wind potentials of a site, wind power density is believed to be a better indicator than wind speed. In this study, the wind power and energy density are evaluated using the Weibull equations (8) and (9), respectively, and tabulated in Table 3. The results illustrated in Figure 4 show that the highest value of wind power density was found at Abéché (69 W/m^2) followed by N'djamena (65 W/m^2) and Pala (55 W/m^2), whereas the lowest wind power density was observed at Bousso, Am Timan, and Ati with the value of 7, 8, and 10 W/m^2 , respectively. On the other hand, the wind energy density ranged between $59 \text{ kWh/m}^2/\text{year}$ and $603 \text{ kWh/m}^2/\text{year}$. The city of Abéché again showed the maximum value of energy with more than $600 \text{ kWh/m}^2/\text{year}$ and Bousso presented the minimum. Based on the presented data, it could be deduced that the maximum power density in Chad is around 70 W/m^2 and it is found in the eastern part of the country.

As wind speeds during the dry season are higher as compared to other periods of the year [6], interestingly, the corresponding power and energy density are also higher in this season. This clearly indicates that a WECS would produce more energy during this period for all the stations at the three distinctive geographical regions. It is also interesting to note that although some stations showed a higher value of monthly mean wind speed, the yearly mean was low due to significant seasonal variations of the site, which lead to low yearly power output. This gives an insight into using a WECS as an alternative for energy generation at such particular period of the year for that particular site.

TABLE 2: Monthly Weibull parameters (k, c).

Station	Parameter	Month											
		Jan	Feb	Mar	Apr	May	Jun	Jul	Aug	Sep	Oct	Nov	Dec
Abéché	k	1.59	1.59	1.72	1.65	1.56	1.50	1.54	1.43	1.39	1.52	1.61	1.52
	c	4.10	4.10	4.85	4.40	3.94	3.63	3.82	3.28	3.09	3.70	4.22	3.77
Am Timan	k	0.91	0.94	0.99	1.02	0.96	0.87	0.86	0.79	0.82	0.83	0.85	0.89
	c	1.17	1.27	1.44	1.56	1.32	1.05	1.00	0.81	0.88	0.91	0.98	1.10
Ati	k	0.97	0.99	1.08	0.99	0.97	1.01	1.02	0.86	0.82	0.89	0.96	0.97
	c	1.36	1.44	1.75	1.44	1.34	1.49	1.53	1.00	0.88	1.10	1.32	1.36
Bokoro	k	0.99	1.00	1.08	1.03	1.06	1.07	1.08	0.96	0.89	0.93	1.01	1.08
	c	1.41	1.46	1.75	1.58	1.68	1.73	1.75	1.34	1.10	1.22	1.49	1.75
Bouso	k	0.80	0.88	0.86	0.93	0.93	0.94	0.77	0.74	0.81	0.80	0.79	0.84
	c	0.81	1.05	1.00	1.22	1.24	1.29	0.74	0.67	0.86	0.83	0.81	0.95
Doba	k	1.28	1.37	1.36	1.46	1.35	1.24	1.17	1.16	1.16	1.12	1.04	1.10
	c	2.59	2.97	2.93	3.44	2.92	2.45	2.09	2.07	2.07	1.90	1.61	1.82
Faya-Largeau	k	1.62	1.55	1.50	1.37	1.27	1.31	1.16	1.16	1.33	1.42	1.53	1.60
	c	4.29	3.87	3.61	3.00	2.54	2.71	2.09	2.11	2.83	3.25	3.77	4.15
Mao	k	1.31	1.31	1.34	1.22	1.18	1.22	1.21	1.11	1.08	1.15	1.24	1.28
	c	2.71	2.71	2.83	2.31	2.14	2.31	2.26	1.85	1.73	2.02	2.38	2.59
Mongo	k	1.28	1.50	1.55	1.52	1.57	1.58	1.44	1.36	1.28	1.38	1.45	1.37
	c	2.61	3.61	3.87	3.70	4.01	4.08	3.35	2.97	2.59	3.06	3.40	3.02
Moundou	k	1.48	1.42	1.31	1.40	1.28	1.25	1.27	1.26	1.08	1.15	1.23	1.27
	c	3.52	3.23	2.76	3.16	2.61	2.45	2.54	2.52	1.77	2.04	2.35	2.54
N'Djaména	k	1.60	1.69	1.75	1.58	1.47	1.60	1.57	1.36	1.31	1.31	1.49	1.56
	c	4.17	4.64	5.03	4.03	3.49	4.13	3.99	2.93	2.71	2.71	3.59	3.96
Pala	k	1.59	1.66	1.68	1.63	1.54	1.45	1.31	1.22	1.30	1.27	1.41	1.54
	c	4.08	4.50	4.59	4.29	3.84	3.40	2.73	2.33	2.66	2.52	3.21	3.86
Sarh	k	1.10	1.06	1.19	1.35	1.31	1.20	1.00	1.03	0.99	1.00	0.88	1.06
	c	1.82	1.68	2.21	2.88	2.71	2.26	1.46	1.58	1.44	1.46	1.08	1.70

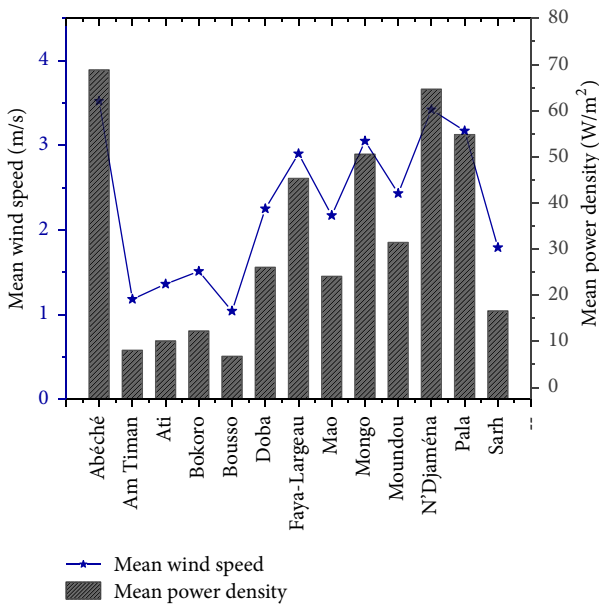


FIGURE 4: Comparison of yearly mean wind speeds and mean wind power density.

5.3. Weibull Distribution. The monthly mean scale parameter c (m/s) and shape parameter k (dimensionless) of the Weibull distribution for all the stations under study are determined using (2) and (3) and furnished in Table 2. It was observed that the shape parameter has smaller temporal variation compared to the scale parameter. The monthly values of the parameter k range between 1 and 1.6 for almost all of the stations, except for a few stations in the Savanna and Sahel zones which exhibit less than one. This indicates that such stations have poor stability and poor persistence compared to the others. The scale parameter c , which is slightly greater than average wind speed, ranges from 2 to 5 m/s for nearly all of the stations in the Sahara and Sahel zones and from 1 to 4 for most of the stations in the Sudanian region. The highest and lowest values of the dimensionless shape parameter k were observed to be 1.80 and 0.67, respectively, and they were found at Ndjamenana and Bouso. This is perhaps due to the more open and flat areas in the Sahel and Saharan regions. Thus, these higher values of the scale parameter denote that these sites are windy.

The frequency and cumulative distributions of monthly average wind speed for all the stations are presented, respectively, in Figures 5 and 6. It is obvious that all curves have

TABLE 3: Yearly Weibull parameters (k, c), average wind speed, wind speed carrying maximum energy, wind power density, and wind energy density (at 10 m height).

Station	k	c	\bar{v}	Parameters		
				$V_{max,E}$	P/A (W/m ²)	E/A (kWh/m ²)
Abéché	1.56	3.91	3.52	6.65	68.80	602.72
Am Timan	0.90	1.13	1.18	4.11	8.04	70.39
Ati	1.00	1.34	1.36	4.26	10.06	88.09
Bokoro	1.02	1.52	1.51	4.42	12.21	106.97
Bousso	0.85	0.96	1.04	4.02	6.73	58.95
Doba	1.24	2.40	2.25	5.20	26.03	228.0
Faya-Largeau	1.41	3.19	2.90	5.95	45.29	396.72
Mao	1.22	2.32	2.17	5.11	24.07	210.85
Mongo	1.45	3.36	3.05	6.11	50.54	442.77
Moundou	1.29	2.62	2.43	5.41	31.41	275.17
N'Djaména	1.53	3.79	3.42	6.54	64.63	566.18
Pala	1.48	3.51	3.17	6.26	54.80	480.01
Sarh	1.11	1.86	1.79	4.70	16.58	145.24

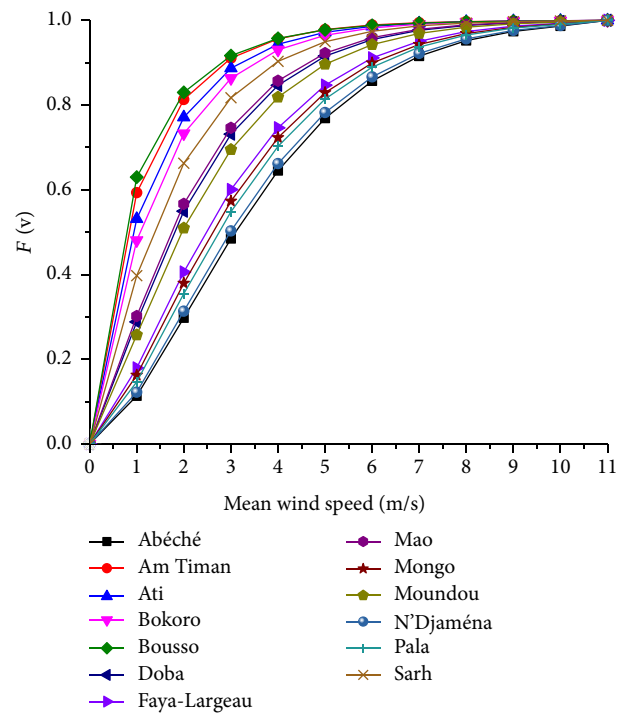
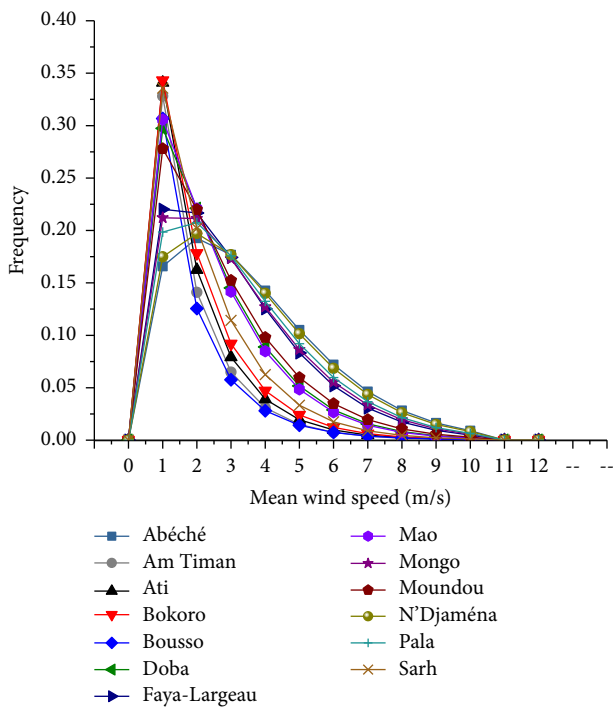


FIGURE 5: Frequency distributions of monthly mean wind speed for all stations.

FIGURE 6: Cumulative distributions of monthly mean wind speed for all stations.

a similar tendency of wind speeds on both frequency and cumulative density. However, the frequency peaks in the range of 2 to 3 m/s for the two regions in the upper part of the country and between 1 and 2 m/s for the lower part of the country. This indicates that most of the wind energy lies in these ranges. This information is very practical and can be used to determine the amount of power which can be generated in a given speed band and could also help in selecting a suitable wind turbine for each particular site.

5.4. Polar Diagrams. Evaluation of wind direction helps to expose the impact of the geographical features on the wind and to obtain the prevailing direction and magnitude of the most frequent wind. In Figures 7–12, METAR data of the year 2014 and polar diagrams for six potential sites in Chad are presented. These locations are from the three distinctive geographical zones. It was observed that the prevailing wind direction varied from zone to zone and within the same zone as well. As such, the prevailing wind direction for the stations

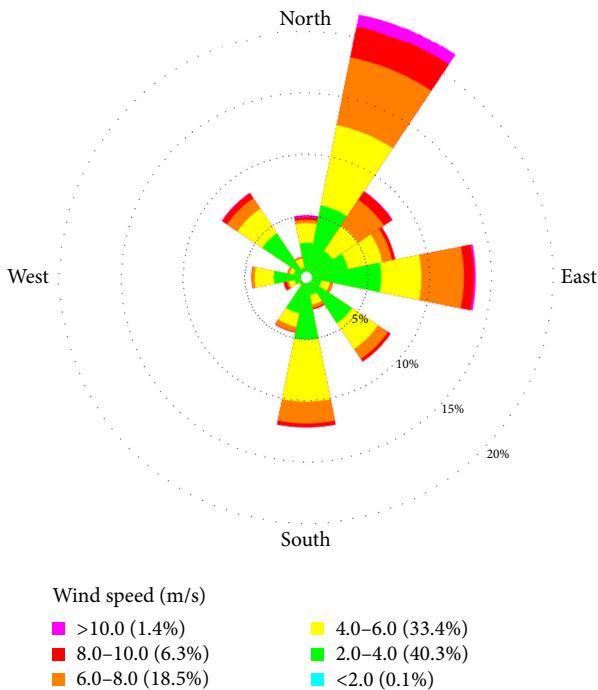


FIGURE 7: Polar diagram: wind direction for Abéché.

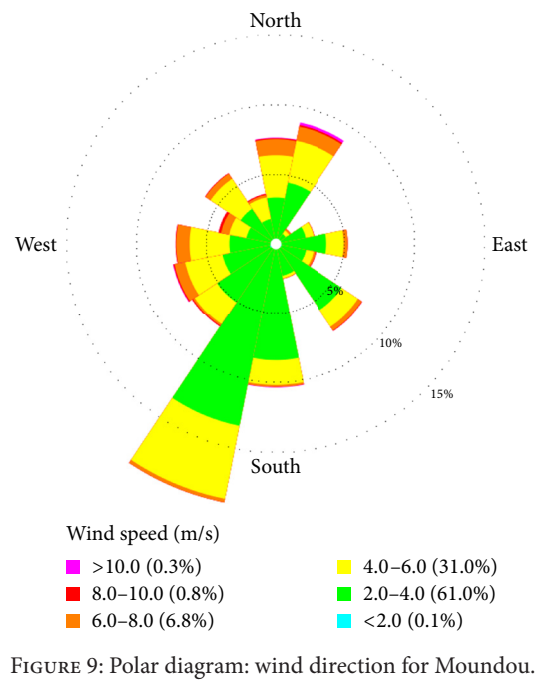


FIGURE 9: Polar diagram: wind direction for Moundou.

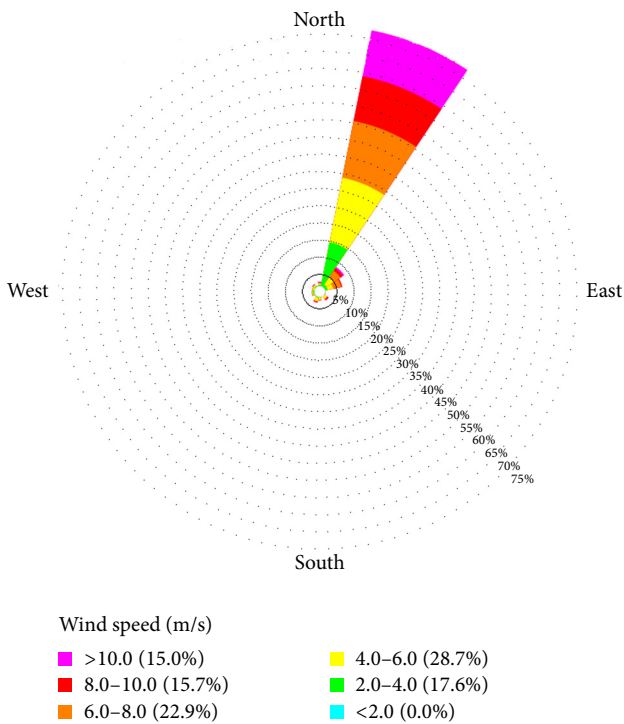


FIGURE 8: Polar diagram: wind direction for Faya-Largeau.

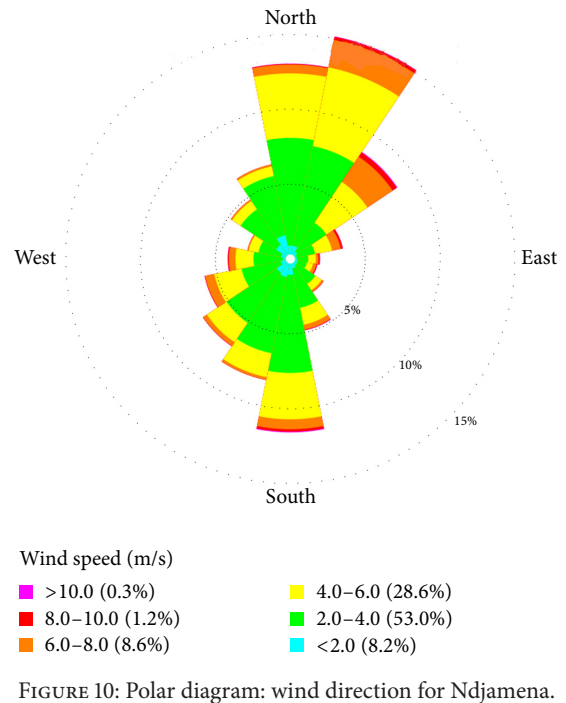


FIGURE 10: Polar diagram: wind direction for Ndjamena.

in the Saharan and Sahel zones was northeast throughout the year, while in the Sudanian zone the direction prevailed at various directions. In Moundou, for example, the most frequent wind direction was dominated by the southwestern wind. Meanwhile, in Pala and Sarh, the wind direction prevailed, respectively, in north and south directions throughout 2014.

6. Conclusion and Future Direction

In this study, the monthly and yearly wind speed distribution and wind power density for thirteen meteorological stations in Chad were evaluated. The novel two-parameter Weibull distribution function was employed to analyze the five-year period data for each site. While the data used in this study are being published for the first time, they are collected for the purpose of studying the wind energy potential and to have a comprehensive wind database or a wind map in Chad.

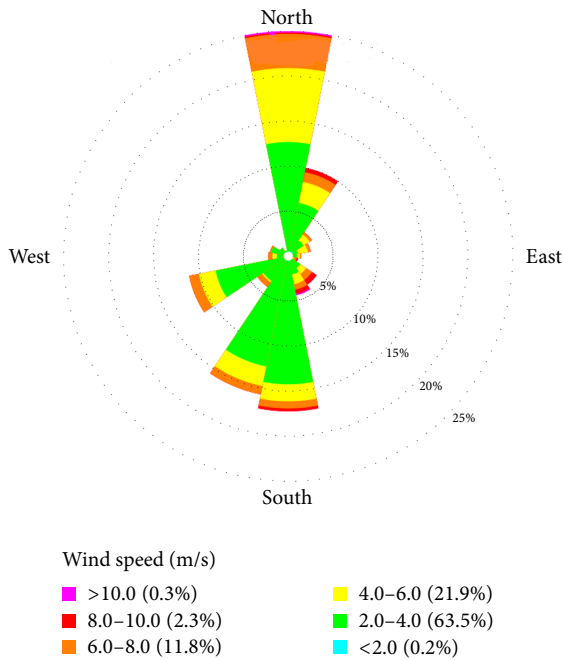


FIGURE 11: Polar diagram: wind direction for Pala.

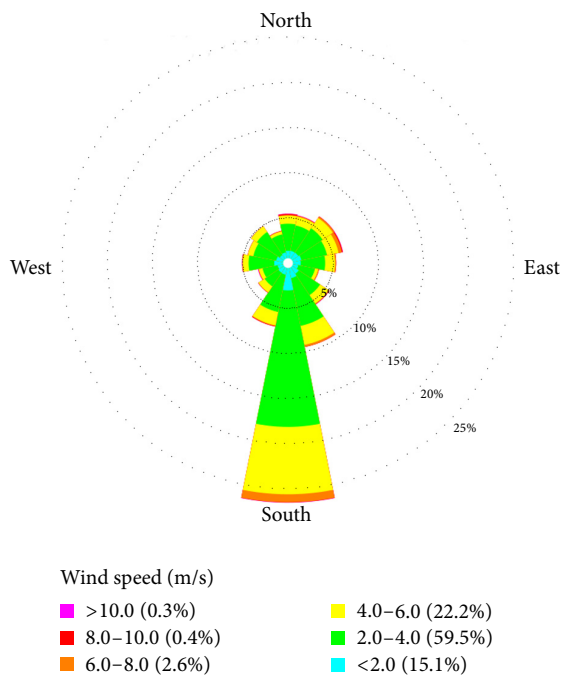


FIGURE 12: Polar diagram: wind direction for Sarh.

The seasonal variations of the mean wind speed data show that higher wind speeds are available when the weather condition is generally dry, that is, November to May, and lower wind speed is found when the weather condition is wet, that is, June to October. This trend is applicable for all the thirteen sites under investigation. Interestingly, it was learned that higher electrical energy demand in the country is also in this period (dry season).

Moreover, the data presented also revealed that the monthly mean wind speed varies in a wide range in each geographical zone. In the Sahel zone, for example, it ranged between 1 and 4 m/s, though most of the stations in this region have shown reasonably strong wind speed of more than 2 m/s. The same behavior was also noticed at the Sudanian zone.

It was observed that the sites in the middle of Sahel and Sudanian zones tend to show lower mean wind speed compared to the others. However, in general, higher wind potentials are witnessed as one moves towards the Saharan region. It is also worth noting that the peak monthly mean wind speed was 4.5 m/s and it was found in Ndjamenana in the month of March. Meanwhile, the lowest monthly average wind speed was less than a unit and was found in Bousso.

Based on yearly averaged data, the most recommended site for wind energy generation in Chad would be Abéché, followed by Ndjamenana, Pala, Mongo, and Faya-Largeau, which are the stations that possess mean wind speed of more than 3 m/s at 10 m height above ground level. These sites exhibited wind power density in the range of 45–69 W/m² and corresponding wind energy density values ranged between 400 and 600 kWh/m²/year. However, although the wind energy potential in Chad is promising for most of the sites under study for small-scale applications, it is concluded that few stations in the middle of Sudanian and Sahel regions (Am Timan, Bousso, Bokoro, and Ati) are not feasible for wind energy generation due to their weak mean wind speed of around 1 m/s.

In terms of wind direction, the prevailing wind direction for both Saharan and Sahel region was dominated by north-eastern wind. However, the wind direction in every station at the Sudanian region prevailed at different directions. The most probable wind speed direction was southwest in Moundou, dominated by northern wind in Pala and southern wind in Sarh.

It is recommended in the future to develop a wind map at the other parts of the Saharan region and some locations close to Lake Chad. The data should be recorded at various heights above ground level and it will then be used for developing wind atlas for Chad which will encourage the development of wind energy projects in the country.

Conflicts of Interest

The authors declare that there are no conflicts of interest regarding the publication of this paper.

Acknowledgments

The authors would like thank Universiti Tun Hussein Onn Malaysia for providing financial support of this research under Grant U416. The authors also wish to express their sincere gratitude to the National Meteorological General Administration (ASECNA) in Chad for the provision of the meteorological data.

References

- [1] Y. S. Mohammed, M. W. Mustafa, and N. Bashir, "Status of renewable energy consumption and developmental challenges in Sub-Sahara Africa," *Renewable and Sustainable Energy Reviews*, vol. 27, pp. 453–463, 2013.
- [2] K. S. P. Kumar and S. Gaddada, "Statistical scrutiny of Weibull parameters for wind energy potential appraisal in the area of northern Ethiopia," *Renewables: Wind, Water, and Solar*, vol. 2, no. 1, p. 1, 2015.
- [3] International Energy Agency (IEA), *World Energy Outlook, 2016*, <http://www.worldenergyoutlook.org/resources/energy-development/energyaccessdatabase>.
- [4] A. S. Ahmed, "Wind energy as a potential generation source at Ras Benas, Egypt," *Renewable and Sustainable Energy Reviews*, vol. 14, no. 8, pp. 2167–2173, 2010.
- [5] A. D. Mukasa, E. Mutambatsere, Y. Arvanitis, and T. Triki, "Development of wind energy in Africa," Report, African Development Bank, 2013.
- [6] D. H. Didane, A. A. Wahab, S. S. Shamsudin, N. Rosly, M. F. Zulkafli, and S. Mohd, "Assessment of wind energy potential in the capital city of Chad, N'Djamena," *AIP Conference Proceedings*, vol. 1831, no. 1, p. 020049.
- [7] C. McSweeney, M. New, and G. Lizcano, *UNDP Climate Change Country Profiles, Chad, 2010*, http://www.geog.ox.ac.uk/research/climate/projects/undp-cp/UNDP_reports/Chad/Chad.hires.report.pdf.
- [8] Wikivoyage, 2016 <https://en.wikivoyage.org/wiki/Chad>.
- [9] S. Rehman, "Wind energy resources assessment for Yanbo, Saudi Arabia," *Energy Conversion and Management*, vol. 45, no. 13–14, pp. 2019–2032, 2004.
- [10] R. Kose, M. A. Ozgur, O. Erbas, and A. Tugcu, "The analysis of wind data and wind energy potential in Kutahya, Turkey," *Renewable and Sustainable Energy Reviews*, vol. 8, no. 3, pp. 277–288, 2004.
- [11] I. Y. Lun and J. C. Lam, "A study of Weibull parameters using long-term wind observations," *Renewable Energy*, vol. 20, no. 2, pp. 145–153, 2000.
- [12] R. M. R. Kainkwa, "Wind speed pattern and the available wind power at Basotu, Tanzania," *Renewable Energy*, vol. 21, no. 2, pp. 289–295, 2000.
- [13] M. Siti, M. Norizah, and M. Syafrudin, "The evaluation of wind energy potential in peninsular Malaysia," *International Journal*, vol. 2, no. 4, 2011.
- [14] S. Mathew and G. S. Philip, Eds., *Advances in Wind Energy and Conversion Technology*, vol. 20, Springer, Berlin, Germany, 2011.
- [15] C. G. Justus, W. R. Hargraves, A. Mikhail, and D. Graber, "Methods for estimating wind speed frequency distributions," *Journal of Applied Meteorology*, vol. 17, no. 3, pp. 350–353, 1978.
- [16] D. Wood, "Small wind turbines," in *Advances in Wind Energy Conversion Technology*, pp. 195–211, Springer, Berlin, Germany, 2011.
- [17] M. R. Islam, R. Saidur, and N. A. Rahim, "Assessment of wind energy potentiality at Kudat and Labuan, Malaysia using Weibull distribution function," *Energy*, vol. 36, no. 2, pp. 985–992, 2011.
- [18] A. A. Shata and R. Hanitsch, "Evaluation of wind energy potential and electricity generation on the coast of Mediterranean Sea in Egypt," *Renewable Energy*, vol. 31, no. 8, pp. 1183–1202, 2006.
- [19] P. Ramírez and J. A. Carta, "Influence of the data sampling interval in the estimation of the parameters of the Weibull wind speed probability density distribution: a case study," *Energy Conversion and Management*, vol. 46, no. 15, pp. 2419–2438, 2005.
- [20] K. Ulgen and A. Hepbasli, "Determination of Weibull parameters for wind energy analysis of Izmir, Turkey," *International Journal of Energy Research*, vol. 26, no. 6, pp. 495–506, 2002.
- [21] A. S. S. Dorvlo, "Estimating wind speed distribution," *Energy Conversion and Management*, vol. 43, no. 17, pp. 2311–2318, 2002.
- [22] M. Y. Sulaiman, A. M. Akaak, M. A. Wahab, A. Zakaria, Z. A. Sulaiman, and J. Suradi, "Wind characteristics of Oman," *Energy*, vol. 27, no. 1, pp. 35–46, 2002.
- [23] V. M. Karsli and C. Geçit, "An investigation on wind power potential of Nurdağı-Gaziantep, Turkey," *Renewable Energy*, vol. 28, no. 5, pp. 823–830, 2003.
- [24] R. Tchinda and E. Kaptouom, "Wind energy in Adamaoua and North Cameroon provinces," *Energy Conversion and Management*, vol. 44, no. 6, pp. 845–857, 2003.
- [25] A. N. Celik, "A statistical analysis of wind power density based on the Weibull and Rayleigh models at the southern region of Turkey," *Renewable Energy*, vol. 29, no. 4, pp. 593–604, 2004.
- [26] E. K. Akpinar and S. Akpinar, "An assessment on seasonal analysis of wind energy characteristics and wind turbine characteristics," *Energy Conversion and Management*, vol. 46, no. 11, pp. 1848–1867, 2005.
- [27] O. A. Jaramillo and M. A. Borja, "Bimodal versus Weibull wind speed distributions: an analysis of wind energy potential in La Venta, Mexico," *Wind Engineering*, vol. 28, no. 2, pp. 225–234, 2004.
- [28] D. Weisser, "A wind energy analysis of Grenada: an estimation using the 'Weibull' density function," *Renewable Energy*, vol. 28, no. 11, pp. 1803–1812, 2003.
- [29] M. Jamil, S. Parsa, and M. Majidi, "Wind power statistics and an evaluation of wind energy density," *Renewable Energy*, vol. 6, no. 5, pp. 623–628, 1995.
- [30] S. O. Oyedepo, M. S. Adaramola, and S. S. Paul, "Analysis of wind speed data and wind energy potential in three selected locations in South-East Nigeria," *International Journal of Energy and Environmental Engineering*, vol. 3, no. 1, p. 7, 2012.
- [31] S. Mathew and K. P. Pandey, "Analysis of wind regimes for energy estimation," *Renewable Energy*, vol. 25, no. 3, pp. 381–399, 2002.
- [32] A. Keyhani, M. Ghasemi-Varnamkhasti, M. Khanali, and R. Abbaszadeh, "An assessment of wind energy potential as a power generation source in the capital of Iran, Tehran," *Energy*, vol. 35, no. 1, pp. 188–201, 2010.

Research Article

Economic Evaluation of Three Available Solutions for Promotion of Wind Power Integration

Hong-Kun Chen,¹ Yan-Juan Yu,¹ Lei Chen,¹ Xin Jiang,¹ and Ren-Yan Yu²

¹School of Electrical Engineering, Wuhan University, Wuhan 430072, China

²North Electro-Optics Group Co., Ltd., Xi'an 710065, China

Correspondence should be addressed to Hong-Kun Chen; chkinsz@163.com

Received 9 February 2017; Accepted 23 March 2017; Published 5 April 2017

Academic Editor: Tariq Iqbal

Copyright © 2017 Hong-Kun Chen et al. This is an open access article distributed under the Creative Commons Attribution License, which permits unrestricted use, distribution, and reproduction in any medium, provided the original work is properly cited.

The limited operational flexibility of combined heat and power (CHP) units is the main cause of wind power curtailment in the thermal-electrical power system of Northern China. Pumped hydrostorage (PHS), heat storage (HS), and electric boiler (EB) are investigated as three alternative options for the promotion of wind power integration. On the basis of two linear models that determine the capacities of these three facilities required for integrating the curtailed wind power, economic evaluation in terms of investment costs and environmental benefits is presented. Analysis results show that HS requires the least investment and has a good performance of coal saving when accommodating the same amount of curtailed wind power. And EB has the greatest potential for wind power integration with the huge growth of installed capacity of wind power in the future.

1. Introduction

With the rapid growth of wind power, it has been a mainstream green energy source in many countries, as well as in China [1]. But a large amount of wind power has to be wasted in the heating season due to the limited flexibility of the combined heat and power (CHP) units, especially in Northern China where the CHP units account for a large share of the generators [2]. CHP units cannot supply adequate downward regulating space for wind power since the production of electricity is strongly dependent on heat demand in the cogeneration system [3]. In view of this situation, wasted wind power is supposed to be reduced by either accumulating directly with electrical storage devices or decoupling heat and power demand with heat compensation devices.

Potential options for electrical storage include electrochemical energy storage, electromagnetic energy storage, and mechanical energy storage [4, 5]. However, most of the electrical storages need vast investment and have not been in the commercial application except pumped hydrostorage (PHS) [6]. PHS is well known as the most promising energy storage technology, accounting for 99% of the available electrical storage capacity all over the world. And it has a good

performance of frequency control and peak load shifting [7]. Comprehensive benefits of introducing PHS for the promotion of wind power accommodation have been analyzed in [8–11], which achieve an agreement that PHS could get cost-effective peak-shaving as well as the reduction in carbon dioxide emissions. Heat storage (HS) and electric boiler (EB) are favorable alternatives for reducing curtailed wind power in terms of releasing heat and power linkage [12]. Several studies focused on HS and EB have also been made to identify their facilitation of wind power integration. Reference [13] analyzed the possibilities of CHPs and HS balancing large scale of wind power and the optimal capacity of HS. In [14], research of optimal combination of PHS and EB in West Inner Mongolia was carried out, which claimed that PHS was less cost-effective than EB with the same reduction of surplus wind power. In [15], both environmental benefits and economic benefits were included in the objective function which was used to calculate the optimum capacity of EB when all of the curtailed wind power has to be accommodated. Reference [16] put forward several evaluation indexes to weigh the effects of HS and EB added to the cogeneration system on wind power accommodation. In [17–22], the performance of HS and EB on decoupling thermal-electrical production

was further analyzed. All of the studies mentioned above have discussed the different approaches for better wind power integration, but few of them have compared the economic benefits of PHS as being the quintessential example of electrical storages with thermal devices.

This paper focuses on the economic evaluation of PHS, HS, and EB for the promotion of wind power integration. The economic analysis is conducted on the basis of calculating the capacities of these three facilities. Further, two linear models are established following the principle of “ordering power by heat (OPH)” or “ordering heat by power (OHP),” respectively, to obtain the expected capacities. This paper is organized as follows. Section 2 is devoted to introducing the operation characteristics of CHP units and constructing OPH and OHP models while Section 3 presents the economic analysis of the three alternatives on the foundation of Section 2. Case studies and discussion are given in Section 4. Finally, conclusions are drawn in Section 5.

2. Proposed OPH and OHP Models

2.1. Operation Characteristic of CHP Unit. Two main types of CHP units, the back-pressure units and extraction-condensing units, are used worldwide in the power system. The heat output of a back-pressure unit is proportional to the power output while the heat and power outputs of an extraction-condensing unit are not certain to a proportional relationship. We just focused on the extraction-condensing units in this study since this type of CHP units is widely installed in Northern China. For simplicity, all the CHPs mentioned below are in terms of extraction-condensing units.

The feasible operation region of a CHP is characterized as an irregular quadrilateral or a polygon which is illustrated in Figure 1. The operation zone of a CHP is assumed to be convex so that the electric power P_i^t , thermal power Q_i^t , and operating cost C_i^t of a CHP can be represented as the linear convex combination of the extreme points. Several studies [23–25] related to the convexity of the CHP unit have been done, and the demonstrated results enable verifying the linear expression of the operating region as follows:

$$\begin{aligned} Q_i^t &= \sum_{k=1}^{M_i} q_{i,k} x_{i,k}^t \\ P_i^t &= \sum_{k=1}^{M_i} p_{i,k} x_{i,k}^t \\ C_i^t &= \sum_{k=1}^{M_i} c_{i,k} x_{i,k}^t \end{aligned} \quad (1)$$

$$\sum_{k=1}^{M_i} x_{i,k}^t = 1, \quad 0 \leq x_{i,k}^t \leq 1,$$

where $p_{i,k}$, $q_{i,k}$, and $c_{i,k}$ are the values of power, heat, and cost of the k th extreme point; M_i is the number of extreme points for the i th CHP; $x_{i,k}^t$ is the combination coefficient. It is worth mentioning that numerous subsets of extreme points are eligible for representing a given operating status (P_i^t , Q_i^t).

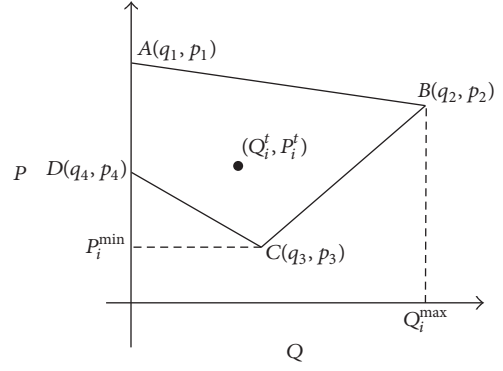


FIGURE 1: The feasible operating region of CHP.

2.2. Ordering Power by Heat (OPH) Model. The electric power produced by CHP units is determined by the thermal power which is the major barrier for the flexibility of CHP. This characteristic is the very foundation of the OPH model which is formulated with the objective function of minimizing the wasted wind power on the premise of meeting the daily heat demand.

Objective Function

$$\min \sum_{t \in T} (P_w - P_{wx}^t); \quad (2)$$

Electric Power Balance Constraint

$$\sum_{i=1}^I \sum_{k=1}^{M_i} p_{i,k} x_{i,k}^t + \sum_{j=1}^J P_{jx}^t + P_{wx}^t = P_e^t; \quad (3)$$

Thermal Power Balance Constraint

$$\sum_{i=1}^I \sum_{k=1}^{M_i} q_{i,k} x_{i,k}^t = P_h^t; \quad (4)$$

Generation Output Constraint

$$0 \leq P_{wx}^t \leq P_w^t \quad (5)$$

$$\sum_{k=1}^{M_i} x_{i,k}^t = 1, \quad 0 \leq x_{i,k}^t \leq 1 \quad (6)$$

$$P_j^{\min} \leq P_{jx}^t \leq P_j^{\max}; \quad (7)$$

Ramp Rate Constraint

$$-P_i^{\text{up}} \leq \sum_{k=1}^{M_i} p_{i,k} x_{i,k}^{t-1} - \sum_{k=1}^{M_i} p_{i,k} x_{i,k}^t \leq P_i^{\text{down}} \quad (8)$$

$$-P_j^{\text{up}} \leq P_{jx}^{t-1} - P_{jx}^t \leq P_j^{\text{down}}, \quad (9)$$

where I and J are the numbers of CHP and power-only units, respectively; T is the scheduling period; P_{jx}^t is the power generated by the j th unit at period t ; P_h^t and P_e^t are the power load and heat load; P_w^t and P_{wx}^t are the forecasted and integrated wind power; P^{up} and P^{down} are the rates of ramping up and down, respectively.

We can obtain the total amount of wasted wind power which would be accommodated directly by PHS and make the operating strategy of PHS by solving this linear OPH model.

2.3. Ordering Heat by Power (OHP) Model. Contrary to the OPH model, the OHP model is established following the principle of "ordering heat by power"; that is, the electric power is given priority to be regulated to accommodate the total wind power as far as possible and part of thermal demand which cannot be met by CHPs would be supplied by heat compensators. A state vector, $V(t)$, is proposed to indicate the operating mode of heat compensator at period t : $V(t) = 1$ means the requirement of heat compensation and $V(t) = 0$, vice versa.

The minimum power output and the equivalent power load of the cogeneration system are noted as follows: E_{\min} and P_{load}^t , respectively.

$$E_{\min} = \sum_{i=1}^I P_i^{\min} + \sum_{j=1}^J P_j^{\min} \quad (10)$$

$$P_{\text{load}}^t = P_e^t - P_w^t.$$

It is obvious that when $E_{\min} > P_{\text{load}}^t$ the wind power is bound to be curtailed and thus $V(t) = 1$. When $E_{\min} < P_{\text{load}}^t$, the value of $V(t)$ has to be further defined by the difference between the maximum heat output of CHPs and heat load. The OHP model is formulated as follows:

Objective Function

$$\max \sum_{i=1}^I \sum_{k=1}^{M_i} q_{i,k} x_{i,k}^t; \quad (11)$$

Electric Power Balance Constraint

$$\sum_{i=1}^I \sum_{k=1}^{M_i} P_{i,k} x_{i,k}^t + \sum_{j=1}^J P_{jx}^t = P_{\text{load}}^t; \quad (12)$$

Other constraints contain (4) and (6)–(9). The value of $V(t)$ is determined with the discriminant function:

$$V(t) = \begin{cases} 1, & \text{if } P_h^t > \sum_{i=1}^I Q_{i,t}^{\text{avail}} \\ 0, & \text{if } P_h^t < \sum_{i=1}^I Q_{i,t}^{\text{avail}}, \end{cases} \quad (13)$$

where $Q_{i,t}^{\text{avail}}$ is the maximum available thermal power of the i th CHP unit solved by (11). $P_h^t < \sum_{i=1}^I Q_{i,t}^{\text{avail}}$ means that the

heat power produced by CHP units is sufficient for heat supply while $P_h^t > \sum_{i=1}^I Q_{i,t}^{\text{avail}}$ means that the heat compensator is required for auxiliary heating.

3. Economic Analysis

The economic analysis is carried out based on the optimal results of OPH and OHP models with typical daily load and wind power curves. The net benefit is used as the index to measure the performance of different solutions in facilitating wind power integration.

3.1. Pumped Hydrostorage (PHS). PHS is expected to consume surplus wind power during off-peak periods by pumping water from the lower reservoir to the upper one. And during peak load periods, the potential energy is transformed into electrical energy again, reducing the power produced by CHP and power-only units. Aiming at integrating the whole generated wind power, the minimum installed capacity of PHS, O_{PHS} , should be larger than the surplus wind power in consideration of energy efficiency.

$$O_{\text{PHS}} = \frac{\sum_{t \in T_w} (P_w^t - P_{wx}^t) \Delta t}{\eta_{\text{PHS}}}, \quad (14)$$

where T_w is the set of the periods when the wind power was wasted. In view of the gross cost of PHS, only the construction cost and maintenance cost are taken into consideration, as well as HS and EB. Thus the annual average cost of PHS can be expressed as follows:

$$\begin{aligned} C_{\text{PHS}}^c &= O_{\text{PHS}} u_{\text{PHS}}^c \frac{r(1+r)^{y_{\text{PHS}}}}{(1+r)^{y_{\text{PHS}}} - 1} \\ C_{\text{PHS}}^m &= O_{\text{PHS}} u_{\text{PHS}}^c \alpha_{\text{PHS}} \\ C_{\text{PHS}}^\Sigma &= C_{\text{PHS}}^c + C_{\text{PHS}}^m, \end{aligned} \quad (15)$$

where η_{PHS} is the energy efficiency; C_{PHS}^c is the converted annual construction cost; C_{PHS}^m and C_{PHS}^Σ are the maintenance cost and gross cost, respectively; u_{PHS}^c is the unit construction cost; r is the bank lending rates; y_{PHS} is the lifetime of PHS; α_{PHS} is the fixed annual maintenance cost ratio.

The economic benefits created by PHS during the daily scheduling period include two parts: the coal saved by replacing power generation of CHP and power-only units during peak load periods and the carbon emission cost reduced by coal saving. The evaluation model is given by

$$B_{\text{PHS}} = (u^{\text{coal}} + u^{\text{car}} \varepsilon) \left(\sum_{t \in T_w} (P_w^t - P_{wx}^t) \Delta t \right) P_{\text{av}}^{\text{coal}}. \quad (16)$$

The daily net benefits of PHS should be expressed as follows:

$$R_{\text{PHS}} = B_{\text{PHS}} - \frac{C_{\text{PHS}}^\Sigma}{D}, \quad (17)$$

where u^{coal} is the cost of per ton of coal equivalent (Tce); u^{car} is the cost of carbon emission; ε is CO_2 emission of per ton coal;

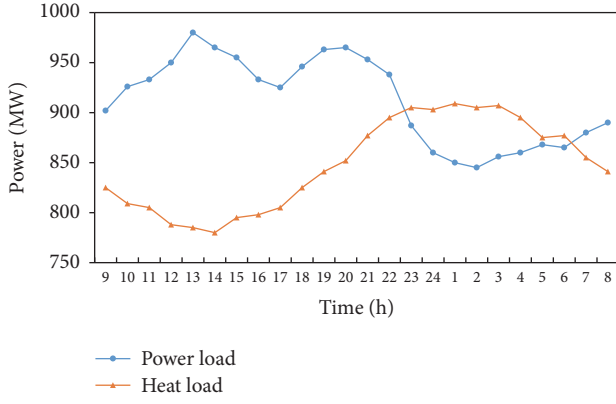


FIGURE 3: Curves of power load and heat load.

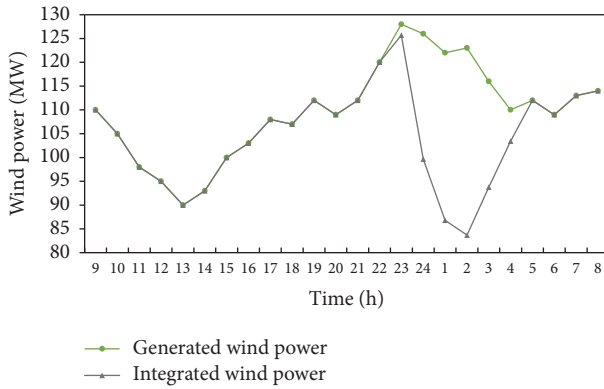


FIGURE 4: Comparison of generated and integrated wind power.

Except for the calculation of R_* , reflecting directly the net benefits, performance of these three different facilities for wind power integration is further discussed with numerable examples in Section 4.

4. Case Studies

4.1. Case 1. In this study, the cogeneration system structure is downscaled based on the actual proportions of installed power energy sources in Northern China. Three CHP units are noted as *CHP1*, *CHP2*, and *CHP3*; two power-only units are noted as *CON1* and *CON2*. The power source structure is listed in Table 1. Detailed information of the units is shown in Table 2. The scheduling period, T , is 24 hours and Δt is 1 hour. D is 180 days. Figure 3 shows the curves of typical daily thermal power load and electric power load. Parameters related to economic analysis are given in Table 3.

By solving the OPH and OHP models, the authors get the same result of T_w which is from 23:00 pm to the next day 4:00 am. Heat compensation is required during these periods if the thermal demand and power demand are simultaneously satisfied without wasting wind power. The curtailed wind power and necessary heat compensation of each period are listed in Table 4. Comparison of generated wind power with integrated wind power is shown in Figure 4. Figure 5 presents the curves of Q_i^{need} and P_i^{need} . The installed capacity of PHS

TABLE 1: Power source structure.

Power Source	Installed Capacity/MW	Proportion
CHP	800	67.8%
Power-only	250	21.2%
Wind	130	11.0%

TABLE 2: Parameters of CHP and power-only units.

CHP Units			
Corner Points	CHP1	CHP2	CHP3
$(q_1, p_1)/\text{MW}$	(0, 323)	(0, 310)	(0, 210)
$(q_2, p_2)/\text{MW}$	(357, 241)	(320, 246)	(240, 155)
$(q_3, p_3)/\text{MW}$	(154, 150)	(100, 150)	(124, 100)
$(q_4, p_4)/\text{MW}$	(0, 150)	(0, 170)	(0, 100)
Power-only Units			
Output Limits	CON1	CON2	
Maximum/MW	150	100	
Minimum/MW	75	50	

TABLE 3: Parameters related to economic analysis.

η_{PHS}	80%
$\eta_{\text{HS}}^{\text{loss}}$	4%
η_{EB}	98%
α_{PHS}	1%
α_{HS}	0.5%
α_{EB}	0.5%
u_{PHS}^c	53.1k\$/MWh
u_{HS}^c	5.3k\$/MWh
u_{EB}^c	217k\$/MWh
$p_{\text{av}}^{\text{coal}}$	330 kg/MWh
$q_{\text{av}}^{\text{coal}}$	154 kg/MWh
r	6%
y_{PHS}	50a
y_{HS}	20a
y_{EB}	20a
u^{coal}	120\$/ton
u^{car}	4\$/ton
ε	2.6

should be $132.02/0.8 = 165.03$ MWh as the aggregated curtailed wind power is 132.02 WMh. The capacity of HS is $278.44/(1 - 0.04) = 290.04$ MWh. The capacity of EB is at least 26.84 MW by solving (21)-(22). Investment costs and economic benefits displayed with histograms in Figure 6 are easy to be calculated since the capacities of these facilities have been known. It can be seen that installing HS needs the least investment cost but gets the maximum net benefit by 4660.85\$ in the case of integrating the same amount of surplus wind power. The EB solution is only second to HS with the net benefit of 4472.21\$ and it creates the most economic benefit by saving coal consumed by electric and thermal power generation concurrently.

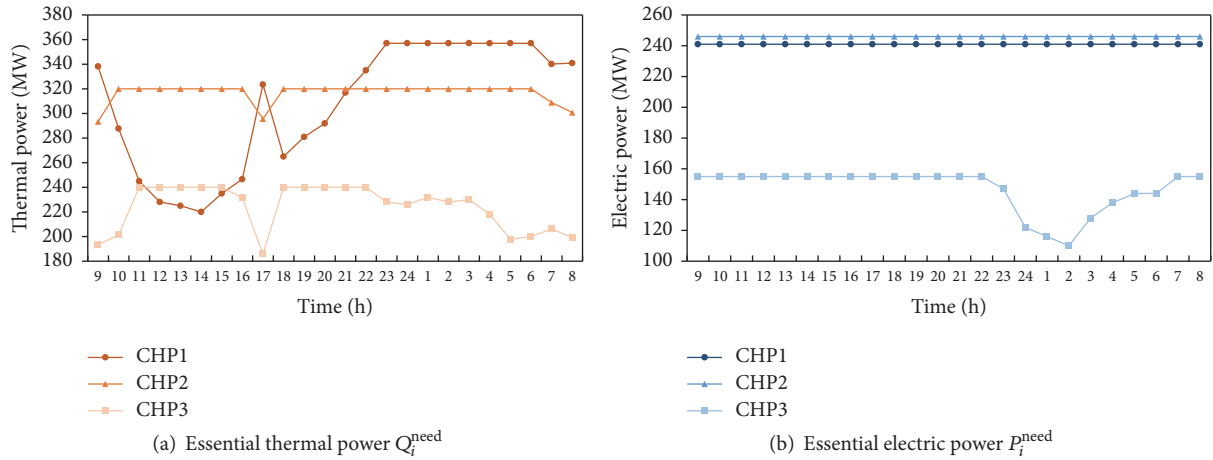


FIGURE 5: Curves of essential thermal and electric power.

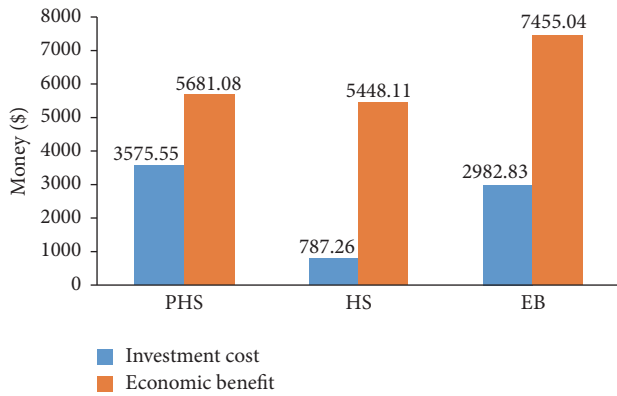


FIGURE 6: Investment costs and economic benefits of PHS, HS and EB.

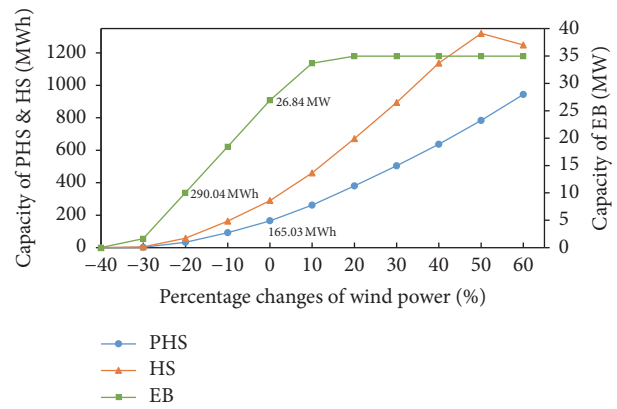


FIGURE 8: Capacity changes of PHS, HS, and EB.

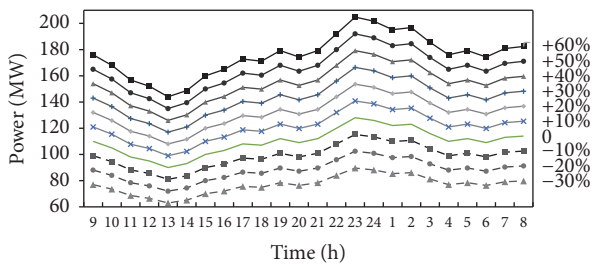


FIGURE 7: Percentage changes of wind power.

TABLE 4: Curtailed wind power and compensated heat power.

Periods	Curtailed Wind/MW	Compensated Heat/MWh
23:00	2.31	4.87
24:00	26.36	55.60
1:00	35.21	74.25
2:00	39.31	82.91
3:00	22.26	46.95
4:00	6.57	13.85
Total	132.02	278.44

4.2. Case 2. The net benefits of different solutions are closely associated with the amount of generated wind power and curtailed wind power. Taking the results in Case 1 as the reference, Figures 7 and 8 show the changes of capacities along with the changes of wind power by moving the curve of generated wind power up and down with the step size of 10%.

As shown in Figure 8, the required capacity of PHS is consistent with the variation of wind power. But the capacity of HS tends to decrease when the wind power is increased by

more than 50%, which is because the available extra thermal power produced by CHPs for heat accumulation starts to decrease with such high wind power generation during the peak load periods. Moreover, the capacity of EB remains unchanged when the wind power increases by more than 20%, verifying the excellent flexibility of EB in adjusting power output with the amount of surplus wind power.

As can be seen from Figure 9, the net benefits of installing PHS, HS or EB for accommodating surplus wind power show a significant growth trend. Thus it is definitely profitable to reduce surplus wind power by integrating PHS, HS, or EB into

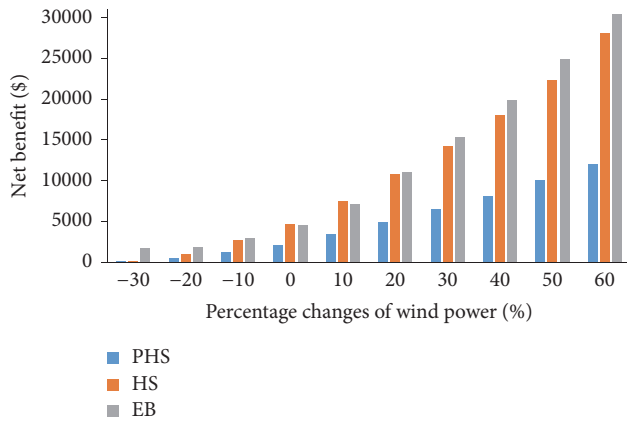


FIGURE 9: Net benefit changes of PHS, HS, and EB.

the cogeneration system. In addition, solutions of utilizing HS and EB for heat compensation have distinct advantages of economic benefits in comparison with PHS. And the net benefit created by installing EB comes to be the best when the generated wind power reaches a high level.

5. Conclusion

This paper presents an evaluation of the economic value of pumped hydrostorage (PHS), heat storage (HS), and electric boiler (EB) in facilitating wind power integration in the cogeneration power system. This evaluation is accomplished by analyzing the investment costs and economic benefits introduced by installing PHS, HS, or EB. Two models denoted as “ordering power by heat (OPH)” model and “ordering heat by power (OHP)” model for obtaining the essential electric power and thermal power required by satisfying the load demand without wind power curtailment are proposed in this study. The minimum capacities of PHS, HS, and EB needed for integrating the same amount of wind power and the subsequent economic analysis are performed on the foundation of the results of these two models.

The cases demonstrated the feasibility of accommodating wasted wind power by these auxiliaries. The capacity of PHS which plays the role of electrical storage is determined by the aggregated surplus wind power and it costs much more than HS and EB. It is economical to utilize the HS to alleviate the conflict between wind power and thermal demand. But the capacity of HS is limited by the heating ability of CHPs since the accumulated thermal power is supplied by CHPs. Instead, the EB shows better performance for promotion of wind power integration with superior economic advantage when the proportion of wind power is very high in the system. Therefore, the HS is preferred if the curtailed wind power is not too much while the EB should be given priority if the wind power develops to an even higher level in the future.

Although the data is simplified in the cases, the conclusion would not be affected by the accuracy of the calculation. More details involved in the practical projects will be considered in the future research.

Conflicts of Interest

The authors declare that there are no conflicts of interest regarding the publication of this paper.

References

- [1] I. Paraschivoiu, O. Trifu, and F. Saeed, “H-Darrieus wind turbine with blade pitch control,” *International Journal of Rotating Machinery*, vol. 2009, Article ID 505343, 7 pages, 2009.
- [2] R. X. Yuan, J. Ye, J. Z. Lei, and T. M. Li, “Integrated combined heat and power system dispatch considering electrical and thermal energy storage,” *Energies*, vol. 9, no. 6, pp. 1–17, 2016.
- [3] Z. G. Li, W. C. Wu, M. Shahidehpour et al., “Combined heat and power dispatch considering pipeline energy storage of district heating network,” *IEEE Transactions on Sustainable Energy*, vol. 7, no. 1, pp. 12–22, 2016.
- [4] B. Dunn, H. Kamath, and J. M. Tarascon, “Electrical energy storage for the grid: a battery of choices,” *Science*, vol. 334, pp. 928–935, 2011.
- [5] J.-N. Liu, Z.-Y. Ren, S.-W. Wu, and Y.-L. Tang, “Theoretical vibration analysis on 600 Wh energy storage flywheel rotor—active magnetic bearing system,” *International Journal of Rotating Machinery*, vol. 2013, Article ID 512674, 11 pages, 2013.
- [6] K. Jiang, H. M. Li, W. Li, and S. J. Cheng, “On several battery technologies for power grids,” *Automation of Electric Power System*, vol. 37, no. 1, pp. 47–53, 2013.
- [7] H. R. Zhao, Q. W. Wu, S. J. Hu, H. H. Xu, and C. N. Rasmussen, “Review of energy storage system for wind power integration support,” *Applied Energy*, vol. 137, pp. 545–553, 2015.
- [8] N. Zhang, C. Kang, D. Kirschen et al., “Planning pumped storage capacity for wind power integration,” *IEEE Transactions on Sustainable Energy*, vol. 4, no. 2, pp. 393–401, 2013.
- [9] A. Tuohy and M. O’Malley, “Pumped storage in systems with very high wind penetration,” *Energy Policy*, vol. 39, no. 4, pp. 1965–1974, 2011.
- [10] J. I. Perez-Diaz and J. Jimenez, “Contribution of a pumped-storage hydropower plant to reduce the scheduling costs of an isolated power system with high wind power penetration,” *Energy*, vol. 109, pp. 92–104, 2016.
- [11] B. Xiao, J. Cong, X. F. Gao, and Y. Gu, “A method to evaluate comprehensive benefits of hybrid wind power-pumped storage system,” *Power System Technology*, vol. 38, no. 3, pp. 338–342, 2014.
- [12] X. Y. Chen, C. Q. Kang, M. O. Malley et al., “Increasing the flexibility of combined heat and power for wind power integration in China: modeling and implications,” *IEEE Transactions on Power Systems*, vol. 30, no. 4, pp. 1848–1857, 2015.
- [13] S. Rinne and S. Syri, “The possibilities of combined heat and power production balancing large amounts of wind power in Finland,” *Energy*, vol. 82, pp. 1034–1046, 2015.
- [14] N. Zhang, X. Lu, M. B. McElroy et al., “Reducing curtailment of wind electricity in China by employing electric boilers for heat and pumped hydro for energy storage,” *Applied Energy*, vol. 184, pp. 987–994, 2016.
- [15] D. Liu, G. W. Zhang, B. H. Huang, and W. W. Liu, “Optimum electric boiler capacity configuration in a regional power grid for a wind power accommodation scenario,” *Energies*, vol. 9, no. 3, pp. 1–13, 2016.
- [16] S. Rong, Z. M. Li, and W. X. Li, “Investigation of the promotion of wind power consumption using the thermal-electric decoupling techniques,” *Energies*, vol. 8, no. 8, pp. 8613–8629, 2015.

- [17] A. Christidis, C. Koch, L. Pottel, and G. Tsatsaronis, "The contribution of heat storage to the profitable operation of combined heat and power plants in liberalized electricity markets," *Energy*, vol. 41, pp. 75–82, 2012.
- [18] H. Dries, P. Leen, H. Lieve, and D. William, "The impact of thermal storage on the operational behaviour of residential CHP facilities and the overall CO₂ emissions," *Renewable and Sustainable Energy Reviews*, vol. 11, no. 6, pp. 1227–1243, 2007.
- [19] Y. L. Yang, K. Wu, X. Yan, J. C. Gao, and H. Long, "The large-scale wind power integration using the integrated heating load and heating storage control," in *Proceedings of the IEEE Eindhoven PowerTech Conference*, Eindhoven, The Netherlands, June 2015.
- [20] T. Nuytten, B. Claessens, K. Paredis, J. V. Bael, and D. Six, "Flexibility of a combined heat and power system with thermal energy storage for district heating," *Applied Energy*, vol. 104, pp. 583–591, 2013.
- [21] Y. Cui, Z. Chen, G. G. Yan, and Y. H. Tang, "Coordinated wind power accommodating dispatch model based on electric boiler and CHP with thermal energy storage," *Proceeding of the CSEE*, vol. 36, no. 15, pp. 4072–4080, 2016.
- [22] H. K. Chen, Y. J. Yu, and X. Jiang, "Optimal scheduling of combined heat and power units with heat storage for the improvement of wind power integration," in *Proceedings of the IEEE PES Asia-Pacific Power and Energy Engineering Conference*, Xi'an, China, October 2016.
- [23] A. Rong and R. Lahdelma, "Efficient algorithms for combined heat and power production planning under the deregulated electricity market," *European Journal of Operational Research*, vol. 176, no. 2, pp. 1219–1245, 2007.
- [24] F. Salgado and P. Pedrero, "Short-term operation planning on cogeneration systems: a survey," *Electric Power Systems Research*, vol. 78, no. 5, pp. 835–848, 2008.
- [25] S. Makkonen and R. Lahdelma, "Non-convex power plant modelling in energy optimisation," *European Journal of Operational Research*, vol. 171, pp. 1113–1126, 2006.
- [26] L. Chen, F. Xu, X. Wang, Y. Min, M. Ding, and P. Huang, "Implementation and effect of thermal storage in improving wind power accommodation," *Proceedings of the CSEE*, vol. 35, no. 17, pp. 4283–4290, 2015.